DTU Library

Atomic-scale Modelling of Magnesium Battery Electrodes

Vincent, Smobin

Publication date:
2022

Document Version
Publisher's PDF, also known as Version of record

[Link back to DTU Orbit](#)

Citation (APA):
Vincent, S. (2022). *Atomic-scale Modelling of Magnesium Battery Electrodes*. Technical University of Denmark.

Smobin Vincent

Atomic-scale Modelling of Magnesium Battery Electrodes

PhD Thesis

August 2022

DTU

Department of Energy Conversion and Storage
Technical University of Denmark

b

Supervisor: Professor Juan Maria García Lastra
Co-supervisors: Professor Tejs Vegge & Assistant Professor Jin Hyun Chang

Abstract

Magnesium batteries are the most promising alternative to lithium ion batteries towards green energy transition due to their relatively high volumetric capacity, availability of Mg and low safety concerns. However, the formation of passivation layer, sluggish ion kinetics and poor ductility of Mg remains a major challenge limiting the development and application in energy storage devices. The thesis presents four investigations designed to understand and develop suitable electrode materials for Mg batteries, addressing the core issues inhibiting their development.

First, a density functional theory (DFT) screening is performed to identify the dopants that enhance the ductility of the Mg anode. The dopants were selected after careful consideration of their ability to improve ductility, stability when alloyed with Mg, and low propensity for surface migration to prevent impact on electrochemical performance. The study identifies 12 dopants that can be alloyed with Mg for battery applications and also suggests a commercial alloy, WE43, as an anode for Mg batteries.

Second, a rigorous phase space search is carried out using DFT based cluster expansion to investigate the phases that form in Sn-based anode during charging and discharging of battery. Anodes based on Sn and its Mg intermetallics have been proposed as a potential solution to mitigate the passivation layer formation. In line with previous experiments, our findings imply that Sn and Mg_2Sn will be the only phases formed during battery operation, and we considered three routes for the transformation from Mg_2Sn to Sn.

Third, a detailed study is performed to understand the charge transport mechanism in the Mg-S battery cathode, with a particular emphasis on the discharge end products MgS and MgS_2, which limit reversible Mg deposition. The study assesed several possible defects in these materials and identified the dominant defects that contribute to charge transport.

Additionally, the charge transport under non-equilibrium conditions during practical battery operation is also studied using ab-initio molecular dynamics.

Fourth and the final project investigated the structural properties of disordered pyroborate $MgMnB_2O_5$ cathode. The study predicted the disorder in the material at different level of magnesiation. Despite having disorder, it is also observed that the material exhibits a specific pattern of cation occupation on fully magnesiation. Structural insights of this material at different level of magnesiation serve as starting point for further study on ion kinetics.

The findings in this thesis provide atomic-level insights into the properties of potential anode and cathode materials for magnesium batteries. The presented results will be able to compliment the researches ongoing world-wide to develop practical magnesium batteries.

Resumé

Magnesiumbatterier er det mest lovende alternativ til lithium-ionbatterier i den grønne energiomstilling på grund af deres relativt høje volumetriske kapacitet, tilgængeligheden af Mg og få sikkerhedsproblemer. Imidlertid er dannelsen af et passiveringslag, langsom ionkinetik og dårlig duktilitet fortsat store udfordringer, der begrænser udviklingen og anvendelsen i energilagringsenheder. Denne afhandling præsenterer fire undersøgelser designet til at forstå og udvikle passende elektrodematerialer til Mg batterier, der tager fat på de kerneproblemer, der hæmmer udviklingen af disse.

Først udføres en density functional theory (DFT) screening for at identificere de dopanter, der øger duktiliteten af Mg-anoden. Dopanterne blev udvalgt efter nøje overvejelse af deres evne til øge duktilitet, stabilitet ved legering med Mg og lav tilbøjelighed til overflademigrrering for at hindre indvirkning på den elektrokemiske ydeevne. Studiet identificerer 12 dopanter, der kan legeres med Mg til batterianvendelse og foreslår også en kommerciel legering, WE43, som anode til Mg batterier.

Herefter udføres en stringent faserumssøgning ved hjælp af DFT-baseret cluster expansion for at undersøge de faser, der dannes i en Sn-baseret anode under opladning og afladning af et batteri. Anoder baseret på Sn og dens Mg intermetalliske forbindelser er blevet fremført som en potentiel løsning til at afbøde dannelsen af passiveringslag. I overensstemmelse med tidligere forsøg indikerer vores resultater, at Sn og Mg_2Sn vil være de eneste faser, der dannes under batteridrift og vi foreslår tre ruter for transformationen fra Sn til Mg_2Sn.

I den tredje del af afhandlingen udføres en detaljeret undersøgelse for at forstå ladningstransportmekanismen i Mg-S batterikatoden, med særlig vægt på afladningsslutprodukterne, MgS og MgS_2, som begrænser reversibel Mg-aflejring. Undersøgelsen vurderer flere mulige defekter i disse materialer og identificerer de dominerende defekter, der bidrager

til ladningstransport. Derudover undersøges ladningstransporten ved ikke-ligevægtsforhold under praktisk batteridrift ved hjælp af ab-initio molecular dynamics.

I det fjerde og sidste projekt undersøges de strukturelle egenskaber af uordnet pyroborat $MgMnB_2O_5$. Studiet forudsiger materialets uorden ved forskellige koncentrationer af magnesium. På trods af materialets uorden, observeres det, at materialet udviser et specifikt mønster i kationbesættelse ved den fulde magnesiumkoncentration. Strukturel indsigt i dette materiale ved forskellige magnesiumkoncentrationer er et udgangspunkt for videre studier af ionkinetik.

Resultaterne fra denne afhandling giver given om materialeegenskaber for både anode og katode på atomistisk niveau. Resultaterne præsenteret heri vil bidrage til den internationale forskning i udviklingen a magnesiumbatterier.

Preface

This thesis is submitted in candidacy for a Doctor of Philosophy (PhD) degree from the Technical University of Denmark (DTU). The work has been carried out between August 2019 and August 2022 at the Section for Atomic Scale Materials Modelling (ASM) at the Department of Energy Conversion and Storage. The studies have been supervised by Juan Maria García Lastra, Tejs Vegge, and Jin Hyun Chang. The PhD project was funded by the "European Magnesium Interactive Battery Community (e-Magic)" FET-Proactive project (Contract N. 824066).

Smobin Vincent

Kongens Lyngby, August 2022

Acknowledgements

List of publications

Publications included in this thesis

Paper I
Computational Design of Ductile Magnesium Alloy Anodes for Magnesium Batteries
<u>Smobin Vincent</u>, Jin Hyun Chang, and Juan Maria García Lastra
Batteries & Supercaps, 4, 522 (2021)

Paper II
Thermodynamic Investigation of Phase Transformation in Sn Anode for Magnesium Batteries
<u>Smobin Vincent</u>, David Kleiven, Juan Maria García Lastra and Jin Hyun Chang,
APL Materials, 10, 071104 (2022)

Paper III
Ab-initio Study of Charge Transport in Mg-S battery Cathode
<u>Smobin Vincent</u>, Jin Hyun Chang, Pieremanuele Canepa and Juan Maria García Lastra
To be submitted

Contents

Summary   81

Bibliography   83

CHAPTER 1

Introduction

Green energy transition from fossil fuels is the key to mitigate the worst impacts of climate change and to reduce carbon emissions. The leading contenders as fossil fuel alternatives are hydroelectric, nuclear, and other renewable energy sources such as solar and wind. Hydroelectric power is a safe, renewable and reliable source of energy, but building dams across the river to has huge environmental consequences related to deforestation, species extinction, and so on. Despite its potential to generate vast amounts of electricity, nuclear power raises concerns about safety and radioactive waste. Renewable energy sources such as solar and wind energy can be a potential game changer as they provide clean energy without having much impact on environment. The main concern with energy from these renewable energy sources are their intermittent supply. The problem pertaining from the intermittent nature of renewable sources can be overcome by using an efficient energy storage technology.

Energy storage technologies are continuously developing and refined, with a variety of competitive options. The selection of an appropriate energy storage technology is based upon the power and energy density, the time period for which energy must be available on the grid, the price and space needed for the infrastructure, and the location of the grid. So far, several ways to store energy have been evaluated and explored. These include pumped storage hydropower (PSH), thermal energy storage, compressed air energy storage, flywheels, batteries, and supercapacitors.[1, 2, 3] Among these, PSH is the most prevalent kind of energy storage, followed by batteries (Figure 1.1). However, PSH has drawbacks such as low efficiency, a large capital investment, and location-specific issues. In comparison, batteries have better efficiency and flexible installation. In recent years, the global market share of batteries as an energy storage technology has increased dramatically. Specifically in the past four years the global market share of batteries increased from 1 %

to $7.4\,\%$.(Figure 1.1).[4]
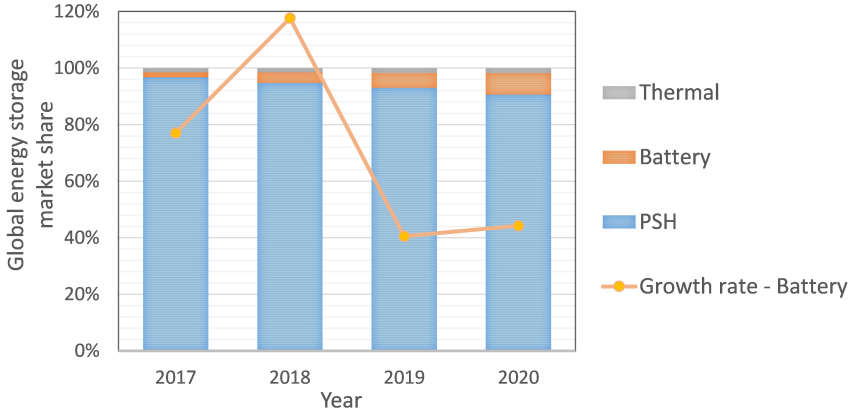
Figure 1.1. Market share of various energy storage technologies in the global energy storage market. The market share of compressed air energy storage, flywheels, and supercapacitors are less than $0.2\,\%$, hence they are not shown in the graph. Based on the data from CNES white paper from the years 2018, 2019, 2020, and 2021 [4]

1.1 Batteries for energy storage

Batteries not only provide energy storage for grids, but also power electric vehicles, portable electronics, medical equipment, machine tools, and toys. Batteries are a strategic and national commodity in today's highly competitive global market. The development of safe, high-energy-density batteries is essential for achieving a carbon-neutral planet.

1.1.1 Basic principle

Batteries are electrochemical storage systems that consist of two electrodes, a positive (cathode) and a negative one (anode), that are joined by an ion conducting but electrically insulating electrolyte. During discharge, ions are released at the anode and move through the electrolyte

to the cathode, generating electrical current in the external circuit (Figure 1.2). If this process is reversed by supplying an external voltage, the battery will be recharged and is called a rechargeable or secondary battery. The voltage is defined as the difference between the chemical potential of an anode and a cathode per elementary charge. This implies that to obtain a high voltage battery, it is desirable to have an anode with a low redox potential and a cathode with a high redox potential.
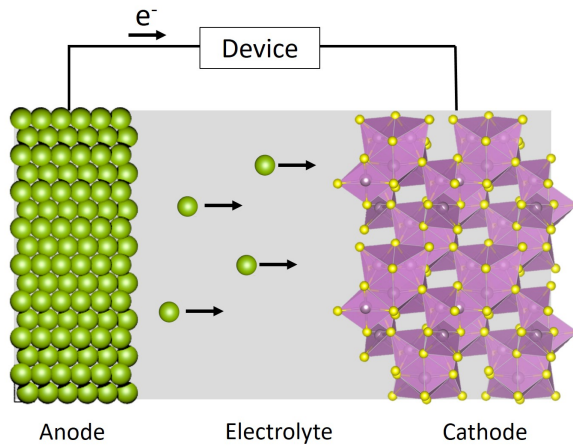
Figure 1.2. Schematic diagram showing the discharge of battery

1.1.2   Short history

Ever since Alessandro Volta made the first real battery using a stack of copper and zinc discs connected with a cloth soaked in salty water, battery storage technologies have evolved continuously, resulting in a plethora of battery chemistries.[5, 6] The first rechargeable batteries were invented in 1859. These were made of lead-acid and are still used today to start vehicles powered by gasoline and diesel engines. However, lead-acid batteries are large and heavy. In 1899, nickel-cadmium batteries were invented, which were more compact but less efficient (70 % efficiency vs 85 % of lead-acid batteries).[7, 8] The twentieth century saw significant improvements in battery research and technology with the invention of lithium-based batteries.

1.2   Li-ion batteries

Stanley Whittingham demonstrated the first functional Li battery using a lithium anode and a TiS_2 cathode.[9] Later, studies by Goodenough showed that cathodes made of layered oxide would react in the same way, but with a higher voltage that would allow for a much higher energy density.[10] However, the lithium anode in these batteries suffered from the formation of dendrites. Dendrites are the thin strands that grow from the anode on repeated charging and may cause a short circuit when they come into contact with the cathode. Eventually, the ingenious discovery of Akira Yoshino to use carbonaceous material as an anode, replacing the Li-metal, led to the development of safer Li-ion batteries (LIBs).[11]

   Even though the capacities provided by Li-intercalated graphite are lower than those offered by Li-metal, (i.e., $837\,\mathrm{mA\,h\,mL^{-1}}$, $372\,\mathrm{mA\,h\,g^{-1}}$ for LiC_6 vs $2061\,\mathrm{mA\,h\,mL^{-1}}$, $3862\,\mathrm{mA\,h\,g^{-1}}$ for Li metal), the specific energy density of LIBs is still higher than that of other rechargeable batteries such as Ni-Cd, Ni-metal hydride, and Pb-acid batteries (about 2.5 times).[12] The exciting breakthroughs in the development of LIBs have resulted in a state-of-the-art battery with a graphite anode and a transition metal oxide cathode that yields an energy density of $240\,\mathrm{W\,h\,kg^{-1}}$ or $640\,\mathrm{W\,h\,L^{-1}}$ over a 1000 charge-recharge cycles.[6] Li-ion batteries have revolutionized technology and continue to be an inevitable part of society.

1.2.1   Need for new battery chemistry

The main challenge that current rechargeable battery technologies face is the increasing gap between the demand for energy storage and the supply from state-of-the-art battery technologies. LIBs alone cannot cater the demand for electrochecmical storage. In terms energy density, LIBs already reached their practical ceiling, as their developments at material level are nearing the fundamental limits.[13] In addition, the availability of essential raw materials for LIBs, such as Li, and Co is a major concern related to the sustainability of LIBs. The long-term availability of Li is still a matter of debate. There is enough lithium reserve, but

the extraction of the lithium is the practical difficulty facing. Moreover, the availability of cobalt is a major concern as it is the main component of state-of-the-art cathodes for LIBs such as $LiNiCoAlO_2$ (NCA) and $LiNiCoMnO_2$ (NCM). According to studies, the demand for cobalt will exceed the available global cobalt reserve in the next ten years (Figure 1.3). Cobalt also accounts for the 20 % to 30 % of the overall battery cost. Even though cobalt-free cathodes such as $LiFePO_4$ (LFP) and $LiMn_2O_4$ (LMO) have been marketed for specialized applications, neither has achieved considerable market penetration in the bigger markets of portable electronics and EVs. In this context, research is tending towards development of better batteries with higher energy density and composed of sustainable materials.
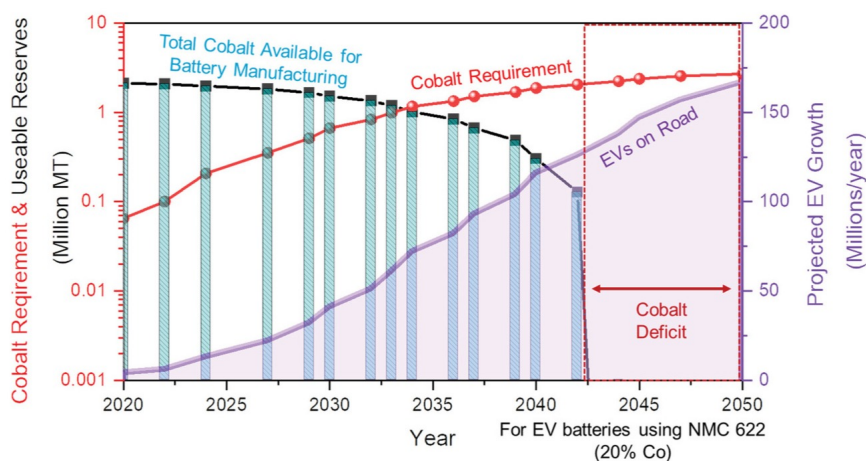
Figure 1.3. Model predicting the depletion of cobalt reserves available for battery manufacturing.[14] Reproduced with permission. Copyright 2015, John Wiley and Sons.

1.3 Magnesium batteries

Rechargeable magnesium batteries (RMBs) have received increased attention as a promising alternative to LIBs due to the ideal features of metallic Mg as the anode. Mg is abundant in the earth crust and has a

high theoretical volumetric capacity of $3832\,\mathrm{mA\,h\,mL^{-1}}$, which is significantly more than Li-metal ($2061\,\mathrm{mA\,h\,mL^{-1}}$). Moreover, despite the fact that metallic Mg is inferior to metallic Li in terms of specific capacity ($2205\,\mathrm{mA\,h\,g^{-1}}$ for Mg vs $3862\,\mathrm{mA\,h\,g^{-1}}$ for Li) and reduction potential ($-2.3\,\mathrm{V}$ for Mg vs $-3.0\,\mathrm{V}$ for Li), the reversible plating and stripping of Mg metal do not promote the formation of the dendrite, unlike its lithium metal counterpart.[15] The absence of dendrite formation, makes it a safer alternative to LIBs. Although the first working prototype for RMBs was reported by Aurbach et al. in 2000,[16] RMBs still have to overcome several challenges before being used for commercial purposes.

1.3.1   Challenges in RMBs

Passivation layer formation

The incompatibility of the metallic Mg anode with standard electrolytes has been recognized as a major challenge since the early stages of developing RMBs. The conventional electrolytes based on typical organic solvents (carbonates, esters, nitriles, lactones, etc.) and simple salt anions (ClO_4, BF_4, PF_6, AsF_6, etc.) exhibit relatively low compatibility with Mg metal anodes.[17, 18] The reaction between the Mg metal anode and the conventional electrolyte forms a passivation layer consisting of ionic Mg compounds at the anode surface, which blocks the transport of Mg ions. The passivation layer blocks the reversible deposition of Mg ions to the anode, leading to poor coloumbic efficiency.[6, 19]

The seminal work of Gregory et al.[20] proposed an etheral solution with salts based on organoaluminate or organoborate can alleviate the problems stemming from the passivation layer formation. Later, Aurbach et al.[16] made a breakthrough by making the first prototype RMB with a metal Mg anode, a chevrel phase Mo_6S_8 cathode, and an electrolyte based on ether (THF) and organo-magnesium-chloride complex ($Mg(AlCl_2BuEt)$. Several groups, following the pioneering work of [16] succeeded in developing ether (mainly tetrahydrofuran (THF) and glyme) based electrolytes that allow reversible deposition/dissolution of magnesium. These include the the magnesium aluminium chloride complex (MACC) electrolyte ($MgCl_2 - AlCl_3$ salt in dimethyl ether (DME)),[21] the all-phenyl complex (APC) electrolyte (($PhMgCl)_2 - AlCl_3$

salt in THF), [22] and the $Mg[B(HFIP)_4]_2$ salt based electrolyte.[23]

Although developing alternative electrolytes offers a promising avenue for the research of RMBs, these electrolytes limit the choice of potential cathodes for RMBs.[17] In this context, magnesium anodes based on materials such as Sn, In, Pb, and Bi that make intermetallic compounds with Mg have been proposed as a solution to the passivation layer problem.[24, 25, 26, 27] Their ability to reversibly deposit magnesium and their appealing theoretical volumetric capacity make them a promising alternative anode for RMBs. However, they confront challenges including electrode pulverization due to volume expansion, capacity loss at high C-rates, and sluggish Mg-ion kinetics.[12, 17] For the development of realistic RMBs, it will be advantageous to have a deeper understanding of the mechanisms causing these obstacles and to devise strategies to overcome them.

Poor ductility of Mg

Mg is difficult to machine into thin foils for practical battery applications due to its poor ductility. The brittleness of Mg originates from its hexagonal crystal structure, which is described in detail in Chapter 3. The current methods for producing thin sheets of Mg via rolling are laborious and expensive.[28] Alloying Mg with small amounts of dopants is another economical solution to obtain ductile Mg.[29] The use of doped Mg as an anode for RMBs is relatively less explored but is a promising avenue to tackle the problem of ductility without compromising the energy density of the battery.

Sluggish Mg^{2+} *ion kinetics*

Alongside the development of the anode and the electrolyte, the design of a high-voltage/high-capacity cathode for magnesium batteries is crucial. However, the development of cathode materials is primarily limited by the slow kinetics of the divalent Mg^{2+} ion. The primary reason for the sluggish ion kinetics is the strong ionic interaction and the polarization induced by the divalent Mg cation.[30] The sluggish Mg^{2+} ion kinetics results in limited reversible capacity and lower power output. Although, the use of materials with good divalent ion mobility, such as cheveral phase Mo_6T_8 (T=S or Se), shows excellent intercalation kinetics and reversibility, the energy densities delivered by these materials

in practical conditions are far from the theoretically expected values.[16] Most of the compounds, which have been demonstrated to be effective Li cathodes, exhibit little or no electrochemical activity with Mg, due to the slow diffusion of Mg^{2+} ion.[30] Several material types, including oxides (V_2O_5,[31] MnO_2[32]), and polyanions ($FeSiO_4$[33]) shows promising electrochemcial performance with Mg. However, the major constraint with these material is the Mg^2+ mobility. Conversion cathode such as sulfur has also been studied as cathode for RMBs. But they face challenges such as poor reversibility of sulfur cathode and polysulfide dissolution.[34] The quest for high capacity cathode for RMBs still continues, and numerous researches are investigating various chemical combinations to find suitable cathode for RMBs. A large chemical space of potential cathode materials for RMBs still remains largely unexplored. Therefore, rigorous experimental and theoretical investigation is required to explore the potential cathode for RMBs.

1.4   Atomic-scale modelling for batteries

Understanding the material properties at the atomic scale has paramount importance in developing new battery technologies. Computational techniques such as density functional theory (DFT) is a powerful tool in understanding the atomic-level mechanisms in electrochemical systems. Such computational tools can be used to understand and predict the material properties in regions where experiments cannot be easily accessed.

DFT has been used with materials for Li-ion batteries since the 1990s.[35, 36] These early studies mainly concentrated on computing the voltages of different cathode and anode materials. The application of DFT in the battery field has expanded over these years, and it has been used to analyze a wide range of material properties, including voltage, material stability, crystal structure, ionic diffusion, and electronic properties.[37] DFT is also used in high-throughput screening, to identify new materials for battery applications. For instance, Bölle et al. demonstrated a workflow for screening ion-insertion cathodes for magne-

sium batteries.[38] The advancement of computational power and simulation techniques has resulted in the emergence of "accelerated material discovery," in which simulation techniques are combined with experiments and artificial intelligence to discover new material chemistries. Understanding and predicting the properties of materials at the atomic scale is a critical step in the search for new materials for battery applications. Therefore, atomic-scale modelling techniques have paramount importance in the development of new emerging technologies such as RMBs..

In this thesis, we aimed to understand and develop possible electrode materials for RMBs using atomic-scale modeling. Throughout this thesis, four separate research projects were carried out to explore the properties of suitable electrode materials for RMBs, addressing the challenges associated with RMBs. The first two projects investigate the properties of the anode, while the third and fourth projects focus on the modelling of the cathode. The first project aims to identify the dopants that can improve the ductility of the Mg anode. The second project explores the chemical space of Mg-Sn anode, which is reported to be a possible alternative to Mg metal anode to alleviate the problem of passivation layer. The third project focused on understanding the transport properties at the cathode side of Mg-S battery. And finally, the fourth project explores the properties of pyroborate $MgMnB_2O_5$ as a cathode for RMBs.

1.5   Outline of thesis

The remainder of thesis is structured as follows:

- **Chapter 2** - *Theory and Methods*
  A brief overview of DFT, nudged elastic band (NEB) method, and cluster expansion (CE) is presented.

- **Chapter 3** - *Ductile alloy anodes*
  A DFT screening study is presented to identify the dopants that improve the ductility of Mg anode for RMB applications. Three main properties of dopants evaluated: ductility improvement, thermodynamic stability, and migration to anode surface.

- **Chapter 4** - *Phase stability of Sn anode*
  A phase search using DFT based cluster expansion (CE) is presented for Mg-Sn system. The energetics of the phases are evaluated using convex. Also presented the voltage profile obtain from CE based MC simulation.

- **Chapter 5** - *Charge transport in Mg-S cathode*
  A charge-transport study is presented for MgS, and MgS_2 which are the discharge end products on Mg-S cathode. Contribution of several defects are evaluated. An ab-initio molecular dynamics study also presented to evaluate charge transport in non-equilibrium conditions.

- **Chapter 6** - *Disorder in pyroborate cathode*
  A study into the structural properties of pyroborate $MgMnB_2O_5$ is presented. Evaluated the disorder at different level of magnesiation using DFT based CE.

- **Chapter 7** - *Summary*
  Main findings from chapter 3-6 are summarized.

CHAPTER 2
Theory and methods

This chapter presents a brief overview of main theory and methods used in the thesis.

2.1 Density functional theory (DFT)

Density functional theory is a matured computation technique for understanding and predicting material properties at atomic scale. The core of DFT is to solve the Schrödinger equation, which represents the wave nature of atomic particles.

2.1.1 The Schrödinger equation

The wave nature of atomic particles was proven experimentally at the beginning of the nineteenth century. Back then, it was assumed that the behavior of atomic particles could be explained by a mathematical wave equation.

The first person to develop such an equation was Austrian physicist Erwin Schrödinger. The Schrödinger equation is the quantum mechanics counterpart of the law of conservation of energy in classical mechanics. The time-independent Schrödinger equation for a particle, defined by a stationary wavefunction $\Psi(\mathbf{r})$ can be expressed as.

$$\mathcal{H}\hat{\Psi}(\mathbf{r}) = E\Psi(\mathbf{r}) \tag{2.1}$$

where $\hat{\mathcal{H}}$ the Hamiltonian operator containing the kinetic energy and the potential energy of the system.

The initial step in solving the Schrödinger equation is determining the Hamiltonian. The Hamiltonian of the many-body system with N_n nuclei and N_e electrons is:

$$\hat{\mathcal{H}} = -\sum_{I=1}^{N_n} \frac{\hbar^2}{2m_n}\nabla_I^2 - \sum_{i=1}^{N_e} \frac{\hbar^2}{2m_e}\nabla_i^2 + \frac{1}{2}\sum_{I,J(I\neq J)}^{N_n,N_n} \frac{Z_I Z_J e^2}{|\mathbf{R}_I - \mathbf{R}_J|}$$

$$+ \frac{1}{2}\sum_{i,j(i\neq j)}^{N_e,N_e} \frac{e^2}{|\mathbf{r}_i - \mathbf{r}_j|} + \frac{1}{2}\sum_{I,i}^{N_e,N_e} \frac{Z_I e^2}{|\mathbf{R}_I - \mathbf{r}_i|} \quad (2.2)$$

which, in concise form expressed as,

$$\hat{\mathcal{H}} = \hat{T}_n(\mathbf{R}) + \hat{T}_e(\mathbf{r}) + \hat{V}_{nn}(\mathbf{R}) + \hat{V}_{ee}(\mathbf{r}) + \hat{V}_{ne}(\mathbf{R},\mathbf{r}) \quad (2.3)$$

where the subscript n and e denotes nucleus and electron, respectively. $\mathbf{R}$ and $\mathbf{r}$ represents the nuclear and electronic coordinates, respectively and Z is the atomic number of the respective nucleus. $\hat{T}$ is the kinetic energy and $\hat{V}$ is the potential energy operator. However, solving this equation is not trivial, thus complexity reductions are required.

2.1.2   The Born-Oppenheimer approximation

The Born-Oppenheimer approximation provides the first simplification towards solving the many body Schrödinger equation by separating electrons and nuclei into two separate mathematical problems. The Born-Oppenheimer approximation defines nuclei as classical point-like particles since the mass of nuclei is typically greater than that of electrons (more than 1000 times). As the positions of nuclei are fixed, their kinetic energy is zero and the potential energy of the nucleus-nucleus interaction remains constant. This approximation simplifies the Hamiltonian.

$$\hat{\mathcal{H}} = \hat{T}_e(\mathbf{r}) + \hat{V}_{ne}(\mathbf{R};\mathbf{r}) + \hat{V}_{ee}(\mathbf{r}) \quad (2.4)$$

Although the Born-Oppenheimer approximation makes the wave function independent of nuclear coordinates, solving the many-electronic wave-function problem still demands a massive computational effort. DFT takes a novel approach to solve this problem by replacing electronic wave-function $\psi(\mathbf{r}_1, \mathbf{r}_2,....,\mathbf{r}_n)$ by charge density (n($\mathbf{r}$)). The two hypotheses

put out by Hohenberg and Kohn serve as the foundational elements of DFT.

2.1.3 The Hohenberg-Kohn theorems

The two theorems proposed by Hohenberg and Kohn [39] are:

1. Proof of existence: There exist a unique external potential, and hence the energy, for any electron density $n(\mathbf{r})$. According to this theorem, the energy functional is written as:

$$E[n(\mathbf{r})] = \int n(\mathbf{r})V_{ext}d\mathbf{r} + F_{HK} \qquad (2.5)$$

with Hohenberg-Kohn functional as:

$$F_{Hk} = T_e[n(\mathbf{r})] + V_{ee}[n(\mathbf{r})] \qquad (2.6)$$

2. (Variational principle) There is a single ground state electron density which can obtained by minimizing the energy functional, and all other electron densities result in an energy value greater than the ground state energy.

$$E_o \leq E[n(\mathbf{r})] = \int n(\mathbf{r})V_{ext}d\mathbf{r} + T_e[n(\mathbf{r})] + V_{ee}[n(\mathbf{r})] \qquad (2.7)$$

2.1.4 The Kohn-Sham equations

For many body wave functions, evaluating the Kinetic energy operator is difficult. The idea proposed by Kohn and Sham to solve the problem in many-electron system, is to define a system of non-interacting electrons in an effective potential($v_{eff}(\mathbf{r})$) which gives the same ground state density as the system with interacting electrons.[40] This reduce the many-body problem to a one electron Schrödinger equation and the wavefunction can be represented as a Slater determinant of single-particle orbitals, ϕ_i. The kinetic energy can then be expressed as

$$T_s[n(\mathbf{r})] = -\frac{\hbar^2}{2m}\sum_i N \int d^3r \phi_i^*(\mathbf{r})\nabla_2\phi_i(\mathbf{r}) \qquad (2.8)$$

All other interactions, that are not considered in non-interacting systems are then added by incorporating additional terms. The contributions to the energy according to Kohn and Sham is described as:

$$E[n(\mathbf{r})] = T_s[n(\mathbf{r})] + V_{ext}[n(\mathbf{r})] + E_H[n(\mathbf{r})] + E_{XC}[n(\mathbf{r})] \qquad (2.9)$$

Where $V_{ext}[n(\mathbf{r})]$ is the external potential from nuclei-electron interaction, $E_H[n(\mathbf{r})]$ is the Hartree energy from the coulomb electron-electron interaction, $E_{XC}[n(\mathbf{r})]$ is exchange-correlation functional, which consider the difference between non-interacting and exact kinetic energies, the non-coulomb electron-electron interactions and all contributions which affect the movement of electrons. The effective potential ($v_{eff}(\mathbf{r})$) used for the non-interacting system can be represented as

$$v_{eff}(\mathbf{r}) = v_{ext}(\mathbf{r}) + v_H(\mathbf{r}) + v_{xc}(\mathbf{r}) \qquad (2.10)$$

The Kohn-Sham equation is often solved iteratively, as explained below:

1. Set a initial trial charge density $n(\mathbf{r})$.

2. Calculate the effective potential V_{eff}.

3. Obtain the single particle wavefunction $\psi(\mathbf{r})$ by solving Kohn-Sham equation using $n(\mathbf{r})$

4. Calculate the new electron density using the wavefunction, $n_{new}(\mathbf{r})$ = $|\psi(\mathbf{r})|^2$

5. Compare $n(\mathbf{r})$ and $n_{new}(\mathbf{r})$. If they are converged, compute the ground state energy and other properties, else the trial charge density is updated and the process repeats from the second step until convergence is reached.

2.1.5   Exchange-Correlation (xc) Functionals

The exact xc functional is unknown. Thus in DFT calculations, the xc functional is approximated to get accurate results. Choosing a reasonable

xc functional is a major consideration before performing the DFT calculation. Local Density approximation (LDA) is the most basic xc functional. The xc energy contributions for LDA is derived from homogenous electron gas model and parametrized using Monte Carlo calculations. The exchange-correlation energy for LDA can be expressed as:

$$E_{xc}^{LDA}[n] = \int n(\mathbf{r}) \epsilon_{xc}^{LDA}[n(\mathbf{r})] d\mathbf{r} \qquad (2.11)$$

where ϵ_{xc}^{LDA} is the xc functional for homogenous electron gas. LDA works well for systems like metals that have a homogenous electron density, while fail for complex systems.

A more accurate approximation for the xc functional is provided by the 'generalized gradient approximation' (GGA). GGA is the improved form of LDA, which also takes into account the gradient of charge density at every point in space. This can be written as:

$$E_{xc}^{GGA} = \int n(\mathbf{r}) E^{xc}(n(\mathbf{r}), \nabla n(\mathbf{r})) d\mathbf{r} \qquad (2.12)$$

GGA comes in a variety of flavors with varying parametrization. The most widely used GGA is the Perude-Burke-Ernzerhof (PBE)[41] functional as it provides a good balance between accuracy and computational cost. Although LDA and GGA fit well with experiments for a wide range of properties, they tend to fail in accurately describing the electronic structure properties of localized states. One reason for this is self interaction error (SIE) in DFT which arises from the fact that DFT considers electrons as electron-densities, and there is no precise way to distinguish which electron-density corresponds to an electron. As a result, the Coloumb energy contribution of an electron includes the self-interaction with its electron-density.

The effect of SIE can be alleviated by using hybrid xc functionals that incorporate a fraction of the exchange from Hartree-Fock (HF) theory, as the HF can provide the exact exchange energy. The xc energy in hybrid functionals is written as

$$E_{xc}^{hyb} = \alpha E_x^{HF} + (1-\alpha) E_x^{DFT} + E_c^{DFT} \qquad (2.13)$$

where α is fraction of exact exchange, E_x^{HF} is the exact exchange from HF theory, E_x^{DFT} and E_c^{DFT} are DFT contribution of the exact, and

correlation energies, respectively. A popular choice of hybrid functional is the Heyd-Scuseria-Ernzherof (HSE)[42] functional, in which the exact exchange is only considered in the short range to simplify the calculations. Although HSE functionals provide accurate results, the computational time required for HSE calculations is still significantly higher than for GGA.

Another widely used method to solve the issues stemming from the SIE but at a modest computational cost is the DFT+U approach. In DFT+U a Hubbard-U correction is applied on top of the LDA/GGA functional. The value of U is derived by fitting it to experimentally measured properties such as band gap.

2.2   Nudged elastic band method

The nudged elastic band (NEB) method [43] is used to find a minimum energy path(MEP) connecting two local minima. The NEB is the modified version of plain elastic band(PEB) method [44, 45]. Typically in these methods, an initial guess of the path from the initial state(R_0) to the final state(R_N) is obtained by linear interpolation. The intermediate points resulting from interpolation are referred to as images and are represented by the notation [R1, R2,..., R$N - 1$]. These images are connected by a spring to avoid them to fall into the endpoints. The objective function is minimized by relaxing the intermediate images until they converge to the MEP. The objective function is expressed as

$$S^{PEB} = \sum_{i=1}^{N-1} F(R_i) + \sum_{i=1}^{N} \frac{k}{2}(R_i - R_{i-1})^2 \qquad (2.14)$$

where $F(R_i)$ force of the image i, and k is the spring constant. The first term denotes the potential force of the configuration and the second term represents the spring force. However, the PEB method is sensitive to the value of the spring constant. A higher spring constant makes the chain stiff and can cuts the corners on the path, which leads to an overestimation of the saddle point energy. This problem arises from the perpendicular component of the spring force. On the other hand, for a lower value of the spring constant, the images are not equally spaced,

which leads to the sliding of images towards the minima. This results from the parallel component of the true force. This can be solved by nudging, which refers to the projection of parallel component of spring force and the perpendicular component of the potential force. Then the force on the image becomes:

$$F_i^{NEB} = F(R_i)^{\perp} + F_i^{s,\|} \tag{2.15}$$

in which the perpendicular component is

$$F(R_i)^{\perp} = F(R_i) - (F(R_i).\boldsymbol{\tau}))\boldsymbol{\tau} \tag{2.16}$$

and the parallel component is

$$F_i^{s,\|} = F_i^s.\boldsymbol{\tau} \tag{2.17}$$

where $\boldsymbol{\tau}$ is the unit tangent in the direction of the path, and F_i^s is the spring force.

2.3   Cluster Expansion

2.3.1   Basic formalism

Cluster expansion treats the scalar physical quantity of a material as a configurational problem. In other words, a scalar quantity of the material can be determined based on the how the atoms are decorated (i.e., the configuration of the atoms) in a fixed lattice. Therefore, the property $q(\boldsymbol{\sigma})$ of a material with N-atomic sites can be expressed as the function of its configurational vector $\boldsymbol{\sigma} = \{s_1, s_2, s_3, s_4, ..., s_N\}$, where s_i is the site variable correspond to the type of atom that occupy the site i. s_i can take one of the value from 0,1,..., $M-1$ for a multicomponent system with M types of atoms. For each s_i, an orthogonal single-site basis function is defined such that

$$\frac{\sum_{s_i=0}^{M-1} \Theta_b(s_i)\Theta_{b'}(s_i)}{M} = \delta_{bb'} \tag{2.18}$$

where $\Theta_b(s_i)$ is bth basis function for ith site and $\delta_{bb'}$ is the Kronecker delta.

The configuration $q(\boldsymbol{\sigma})$ can be represented as the sum of clusters. The clusters can be singlets, pairs, triples, quadruplets, etc. The symmetry equivalent clusters are considered as the same cluster, α. Each cluster is defined by a set of cluster functions, $\Phi_{\mathbf{b}}(\mathbf{s})$.

$$\Phi_{\mathbf{b}}(\mathbf{s}) = \prod_i \Theta_{b_i}(s_i) \tag{2.19}$$

where $\mathbf{b}$ is the vector defining the order of the single-site basis and $\mathbf{s}$ vector containing all site variables. The average of the cluster functions associated with each cluster gives the correlation function, ϕ_α. Then, the quantity, $q(\boldsymbol{\sigma})$ per lattice site can be expressed as

$$q(\boldsymbol{\sigma}) = J_0 + \sum_\alpha m_\alpha J_\alpha \phi_\alpha \tag{2.20}$$

where m_α is the multiplicity of the cluster, J_α is the effective cluster interaction (ECI) associated with cluster α, and J_0 is the ECI for the empty cluster.

2.3.2   Cluster expansion construction

A CE model is constructed by obtaining optimal ECIs by fitting selected number of reference data to the corresponding atomic configurations. The reference data is mostly the energies (can be any scalar quantity) obtained from DFT calculations. The ECIs can then used to predict the energy using the equation (2.20). The predictive power of the CE model is evaluated based on cross validation (CV). The scheme used in this thesis for the CV is leave-one-out (LOO), and the LOOCV score is expressed as

$$\text{LOOCV} = \sqrt{\frac{1}{N} \sum_{i=1}^{N} (\hat{q}_i - q_i)^2} \tag{2.21}$$

where N is the number of atomic configurations, $\hat{q}_i$ is the predicted physical quantity of structure i by CE model constructed using N-1 structures without the structure i and q_i is the calculated value of the physical quantity corresponds to structure i.

The steps in constructing a CE model is described below.

1. Generate training structures.

2. Perform DFT calculations.

3. Fit the CE model and check whether the CE is converged. The convergence of CE is determined by a low CV score.

4. If the CE is converged it can be used to predict the properties of the system, else repeat the process from step 1.

2.3.3   Monte Carlo simulation

MC methods refer to a broad range of computational algorithms that use repeated random sampling to obtain deterministic properties. In this thesis, we used metropolis MC in combination with a Hamiltonian from CE. This allows us to efficiently sample a large configurational space and obtain the thermodynamic properties. The algorithm for Metropolis MC is described below.

1. Start from the initial configuration (q_i).

2. Randomly move (trial move) one (or more) particles in the system to obtain the new configuration (q_{i+1}).

3. Calculate the change in energy due the trial move, $\Delta E = E(q_{i+1})$-$E(q_i)$.

4. If $\Delta E \leq 0$, then always accept the new configuration; that means set q_{i+1} as q_i. And go to step 8.

5. If $\Delta E > 0$, then calculate 'transition probability', $W = \exp(-\beta \Delta E)$. $\beta = \frac{1}{K_B T}$, where K_B is the Boltzmann constant and T is the temperature.

6. Generate a random number, r between 0 and 1.

7. If $r \leq W$ accept the new configuration, else continue with the previous configuration

8. Repeat the process form step 2 to 8 for sufficient number of trial move, so that system is sampled enough.

9. Compute average of the properties.

Part I

Anode

CHAPTER 3

Ductile alloy anodes

This chapter presents the work in paper 1 - *Computational Design of Ductile Magnesium Alloy Anodes for Magnesium Batteries.* The paper is included in this thesis. The text is taken directly from the paper with minor changes for the purpose of the thesis.

3.1   Introduction

As described in Section 1.3.1, the brittle nature of magnesium is a serious obstacle to overcome in fabricating sufficiently thin foils to be used as RMB anodes. Consequently, magnesium anode's ductility has to be increased to develop practical RMBs in conjunction with next-generation electrolytes that suppress the formation of the passivation layer. Magnesium exhibits low ductility due to its hexagonal crystal structure. Existing experimental and theoretical studies indicate that doping magnesium with suitable elements will promote the formation of stacking fault, which in turn improves the ductility of magnesium.[28, 29] Stacking faults are crystal imperfections formed due to the addition or removal of an atomic layer. The excess energy per unit area due to the faults is known as stacking fault energy (SFE). There are three main types of basal stacking faults for Mg: one extrinsic stacking fault with ABABCABAB stacking sequence and two intrinsic stacking faults with ABABCBCB (called I_1) and ABABCACA (called I_2) stacking sequences. Sandlöbes et al. reported that reduction in the SFE of I_1 stacking fault (I_1SF) on doping improves the ductility of magnesium.[29]

Experimental reports on the use of doped Mg as RMB anode are relatively scarce. In aqueous electrolytes, Zhao et al.[46] and Wang et al.[47] have tested the AZ31 commercial alloys (Mg-3 wt% Al-1 wt% Zn). Wang

et al. also tested AP65 (Mg-6 wt% Al-5 wt% Pb).[47] According to their reports, both AZ31 and AP65 exhibit larger overpotentials than pure Mg. Regarding non-aqueous electrolytes, Schloffer et al. studied Mg-1.55 wt% Gd, Mg-1.63 wt% Zn and Mg-1.02 wt% Gd-1.01 wt % Zn alloys with APC as electrolye.[48] They observed that after 5 cycles only the samples doped exclusively with Zn were showing a clear overpotential. Very recently, Mandai and Somekawa made a systematic analysis of Mg doped at 0.3 wt% with nine different elements, namely Ag, Al, Bi, Ca, Li, Mn, Sn, Y and Zn, with $Mg[B(HFIP)_4]_2$/diglyme salt-electrolyte combination.[23] They reported that Zn and Bi increase the overpotential with respect to pure Mg, while Ag and Ca decrease it. The other five elements (Al, Li, Mn, Sn and Y) did not seem to have any noticeable effect on the overpotential. The reason for the different influence of the dopants on the overpotentials remains unclear.

In this work, we hypothesize that the dopants that modify the electrochemical properties of Mg, either benignly or detrimentally, are those that either segregate or migrate towards the surface of the system. By contrast, those dopants that stay at the bulk will be electrochemically inert (i.e., they will not affect the overpotentials, the electron conductivity at the surface, corrosion or passivation at the anode). Ideally, one should try to find dopants that enhance Mg ductility while concomitantly improve its electrochemical properties. The latter may be difficult to rationalize since several complex processes such as Mg diffusion at the surface and Mg solvation/disolvation need to be accounted, and they depend on the electrolyte being used. A more conservative approach is to focus solely on seeking dopants that reduce Mg brittleness without interfering with the electrochemical processes. Our strategy ensures to increase the ductility of RMB anode without sacrificing any other property.

Several authors have used density functional theory (DFT) to perform an exhaustive search to find suitable doping elements that improve the ductility of magnesium.[28, 29, 49, 50] The work of Zhang et al. has identified a set of 34 elements that improve the ductility of magnesium.[49] As an initial step of the investigation, we took these 34 elements and confirmed that they lower the SFE of I_1SF on alloying with magnesium based on our DFT calculations. As the dopants' impact on the electrochemical properties of the magnesium anode has not been explored, we

investigated their propensity to migrate to the surface. Based on the propensity criterion, we have identified 12 dopants that could be added to magnesium to form a suitable ductile alloy anode while not compromising its electrochemical properties. Some of the identified systems can be readily purchased for further testing as they are commercially available.

This chapter is structured in four sections. A short discussion on the brittleness of magnesium and how stacking faults helps to improve its ductility is presented in section 2. Section 3 covers the methodology and the computational details. The main results of this work are presented and discussed in section 4. Some final comments are provided in the last section.

3.2   Ductility in Magnesium

The brittleness of Mg originates from its insufficient number of independent slip systems needed to accommodate deformations. According to the Von Mises criterion, a material requires five independent slip systems to allow deformations.[51] The possible slip systems in an hcp crystal, the crystal structure of magnesium at room temperature, are illustrated in Figure 3.1. The corresponding number of independent slip systems are listed in Table 3.1.
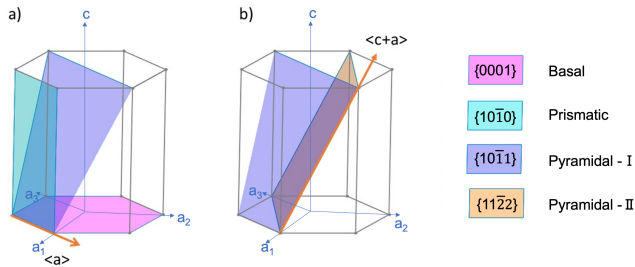
Figure 3.1.   Possible slip systems in hexagonal system.   a) Basal, prismatic and pyramidal–I slip systems in $\langle a \rangle$ direction and b) pyramidal–I and pyramidal–II slip systems in $\langle c + a \rangle$ direction.

Direction	Plane	Number of independent slip systems
$\langle a \rangle$	Basal	2
	Prismatic	2
	Pyramidal–I	4
$\langle c + a \rangle$	Pyramidal–I	5
	Pyramidal–II	5

Table 3.1. Independent slip systems in magnesium crystal system.[52]

Basal and prismatic slips along $\langle a \rangle$ direction offer two independent slip systems each. The four slip systems of pyramidal–I along $\langle a \rangle$ direction is crystallographically equivalent to the combination of basal $\langle a \rangle$ and prismatic $\langle a \rangle$ slips.[52] Therefore, only four independent slip systems are attainable in $\langle a \rangle$ direction. On the other hand, pyramidal–I and pyramidal–II slips along $\langle c + a \rangle$ direction offer five independent slip systems, and activating any of the slips along $\langle c + a \rangle$ direction can satisfy the Von Mises criterion. Wu and Curtin showed that $\langle c + a \rangle$ dislocations are metastable even in pure Mg once they are formed, although the their formation is energetically unfavorable.[53] Therefore, finding dopants that activate and further stabilize the $\langle c + a \rangle$ dislocations is a suitable strategy to enhance the ductility of Mg.

The dopants activate $\langle c + a \rangle$ dislocations through the promotion of stacking faults.[29] Sandlöbes et al. investigated the relationship between ductility and SFEs in Mg and Mg–Y alloys.[29] They observed a reduction in SFE of Mg upon alloying with Y and reported that the improved ductility of Mg–Y alloys was due to the high activity of pyramidal–I and pyramidal–II $\langle c + a \rangle$ dislocations. The plausible explanation for this is that I_1 stacking fault (I_1SF) can act as nucleation source for $\langle c + a \rangle$ dislocations.[28] Thus, dopants that reduce the SFE (relative to that of pure Mg) for the I_1SF will promote $\langle c + a \rangle$ dislocations, and consequently will enhance Mg ductility. Therefore, we limit the scope of the stacking faults to I_1SF in this study.

3.3   Computational methods

Three conditions need to be fulfilled in order to assess whether the addition of dopants is beneficial for RMB applications:

- The dopant should improve magnesium's ductility (the SFE for the I_1SF should be lowered after dopant addition).

- The dopant has to form a thermodynamically stable alloy with magnesium.

- The dopant should be more stable either in bulk or at stacking faults than on the surface to form a dopant-free surface.

Regarding the first condition, the first-principle study of Zhang et al. on I_1SF identified 34 dopants that decrease the SFE of magnesium.[49] These elements are Al, Ba, Bi, Ca, Ce, Cs, Dy, Er, Eu, Ga, Gd, Hf, Ho, In, K, La, Lu, Na, Nd, Pb, Pr, Rb, Sc, Sm, Sn, Sr, Tb, Ti, Tl, Tm, Y, Yb, Zn and Zr. In our study, we restricted ourselves to this set of 34 dopants with a doping concentration of $\sim 2.08\,\%$ for all alloy structures (i.e., one dopant atom per 48 atoms), which lies in the typical doping level of commercial alloys ($\sim 1\,\%$ to $3\,\%$). We carried out our own first-principle I_1SF study since the SFE depends on the doping level, while no SFEs have been reported for a $2.08\,\%$ doping concentration to the best of our knowledge.

The SFE for the I_1SF was calculated using

$$\text{SFE} = \frac{E^{I_1\text{SF}} - E^{\text{bulk}}}{2A}, \tag{3.1}$$

where $E^{I_1\text{SF}}$ and E^{bulk} are the energies of the structures with and without stacking faults, respectively. A is the area of the stacking fault plane, which corresponds to the area of the XY plane in this work. The term "bulk" refers to the bulk of the material in a pristine form without stacking faults. The I_1SF and bulk structures used in the calculations are shown in Figure 3.2. We tested the size of the SF supercell to make sure that the interactions between the SF defects are negligible. The change in SFE for the supercells with SFs seperated by more than 8 atomic

layers is less than $1\,\mathrm{mJ/m^2}$. To perform calculations with low doping concentration ($\sim$2.08\%), we employed $2 \times 2 \times 12$ supercell of hcp containing 96 atoms for both structures, and two magnesium atoms were substituted with the dopants for the alloy structures. Due to periodic boundary conditions, the I_1SF structure has two stacking-fault planes separated by 12 atomic layers to minimize the interaction between them, and a dopant was placed on each of the stacking faults.

We used Vienna Ab initio Simulation Package (VASP) to perform first-principle calculations based on DFT.[54, 55] The Perdew-Burke-Ernzerhof (PBE) parameterized GGA functional was employed to describe the exchange and correlation effects,[41] and the projector augmented wave (PAW) method was used to account for the core-valence interaction.[56] A plane-wave basis set with cut-off energy of $520\,\mathrm{eV}$ was used for all calculations. The Brillouin zone is integrated with the k-point mesh generated using the Monkhorst-Pack scheme with a k-point density of 4.5 per Å^{-1} for all the structures. The convergence of the k-point density was tested for magnesium and all other elements in this
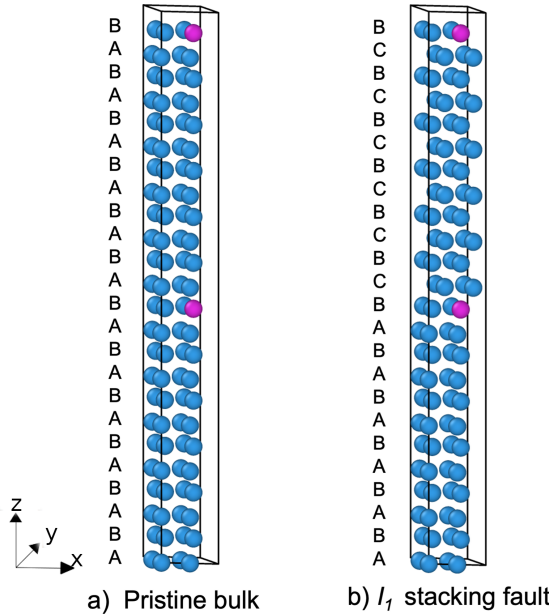
Figure 3.2. Structures of a) pristine bulk and b) I_1SF. Mg atoms are shown in blue and the dopants are shown in pink.

study, and the difference in total energy was found to be less than 2 meV/atom. The convergence criterion for the electronic self-consistent loop was set to 1×10^{-6} eV, and the atomic positions were relaxed until the force on each atom reached below 1×10^{-2} eV Å^{-1}. The structure and atomic positions were relaxed for both bulk and I_1SF structures, and only the atomic positions were relaxed for the slabs.

The second and third conditions (the alloy stability and the dopant's propensity to migrate to the surface, respectively) were evaluated based on conventional expressions for formation energies. The formation energies of an alloy when a dopant is in bulk, at stacking fault or on the surfaces were calculated using

$$E_f^{\text{struct}} = \frac{E^{\text{struct}}(\text{Mg}_{m-n}\text{X}_n) - E^{\text{struct}}(\text{Mg}_m) - nE(\text{X}) + nE(\text{Mg})}{n}, \qquad (3.2)$$

where struct can be either bulk, I_1SF, or surface terminations (e.g., (0001), (1010), and (1011)). $E^{\text{struct}}(\text{Mg}_{m-n}\text{X}_n)$ is the energy of the structure where n out of m Mg atoms are substituted with dopant atoms. $E^{\text{struct}}(\text{Mg}_m)$ is the energy of the same structure with no dopants (i.e., all m atoms are Mg). $E(\text{X})$ is the energy per atom of X in its most stable crystalline structure. $E(\text{Mg})$ is the energy per atom of Mg in hcp. All the simulations for calculating formation energies have the same calculation parameters used for the stacking fault simulations for consistency. In addition, the number of atoms in the supercells were kept to 96 for all the cases (i.e., m=96 in (3.2)), with two dopant atoms placed as far apart from each other as possible.

The stability of the alloy (second condition) was evaluated based on the formation energy with the dopant in the bulk/stacking fault. The E_f^{bulk} or $E_f^{I_1\text{SF}}$ should be negative to form a stable alloy. The dopants will segregate and form a separate phase if they are positive. The energy of the bulk and I_1SF structures were also computed using the structure shown in Figure 3.2. The propensity of the dopant to migrate to the surface (third condition) was analyzed by comparing the formation energies of the alloys when the dopant is in the bulk and at stacking fault versus on surfaces. The relative energy of the dopant in the bulk and at the stacking fault versus on the surface are written as

$$\Delta E^{\text{bulk}} = E_f^{\text{bulk}} - E_f^{\text{surface}} \qquad (3.3)$$

and

$$\Delta E^{I_1 \mathrm{SF}} = E_f^{I_1 \mathrm{SF}} - E_f^{\mathrm{surface}}, \tag{3.4}$$

respectively. The superscript 'surface' refers to one of (0001), $(10\bar{1}0)$ and $(10\bar{1}1)$ surface terminations considered, and the E_f^{surface} is for the most thermodynamically favorable Mg surface for the dopant. At least one of ΔE^{bulk} or $\Delta E^{I_1 \mathrm{SF}}$ should be negative in order to ensure that the dopant does not migrate to the surface.

The preliminary step for assessing the migration of the dopants towards the surface is to determine which Mg surface terminations are thermodynamically most favorable. The surfaces formed in magnesium at equilibrium condition were identified using the Wulff plot analysis. The 12 symmetrically distinct surfaces in magnesium crystal with the lowest Miller indices were considered for the Wulff construction. We followed the methodology in the work of Tran et al.[57] to obtain the Wulff plot using our lattice constants and simulation parameters. Tran et al. reported that the minimum thickness of 10 Å for both slab and vacuum is sufficient to converge surface energies to within 0.02 J/m². We used slab structures with two surfaces separated by a minimum of 8 atomic layers (>10 Å) and vacuum thickness of 10 Å for the surface energy calculations. The surface energy, γ^{surf}, of different surfaces required for obtaining the Wulff shape is calculated using

$$\gamma^{\mathrm{surf}} = \frac{E^{\mathrm{slab}} - n^{\mathrm{slab}} E_{\mathrm{Mg}}}{2 A^{\mathrm{slab}}}, \tag{3.5}$$

where E^{slab} is the energy of the slab model with the surface, n^{slab} is the number of atoms in slab structure and A^{slab} is the area of the slab along the surface plane. The Wulff shape was obtained using the Wulff analysis module implemented in Pymatgen.[57, 58] After identifying the surfaces formed in magnesium at equilibrium conditions, the formation energies of the surfaces were calculated using (3.2).

3.4   Results and Discussion

3.4.1   Ductility analysis

The alloying elements that reduce SFE of magnesium upon alloying are identified as suitable dopants that enhance the ductility of Mg. The SFEs calculated for the 34 binary magnesium alloys with the dopant concentration of $\sim 2.08\,\%$ are given in Section 3.4.1. The SFE obtained for the pure magnesium is $21.547\,\mathrm{mJ/m^2}$, which is in agreement with the previous studies.[29, 49, 59] All the doping elements other than Zn exhibit a reduction in the SFE on alloying with magnesium. The anomalous behavior of Zn is in contrast to the results of Zhang et al. where all the 34 dopants showed a decrease in the SFE.[49] For a $2.08\,\%$ doping concentration, our results show that SFE for Zn-doped Mg is $1.6\,\mathrm{mJ/m^2}$ larger than that of pure Mg. On the other hand, SFEs of Zn alloys with $1.1\,\%$ and $2.5\,\%$ Zn concentrations are more stable than pure Mg by $0.2\,\mathrm{mJ/m^2}$ and $2.3\,\mathrm{mJ/m^2}$, respectively, according to Zhang et al.[49]. One cannot draw a conclusion on the ability of Zn to promote stacking faults based on such small changes in SFE, especially when we account for the inherent DFT inaccuracies and the spurious dopant–dopant interactions of our model. Therefore, Zn was not disregard for subsequent analyses, especially because Zn is present in numerous commercial Mg alloys.

3.4.2   Wulff plot analysis

The surface energies calculated for 12 surfaces with the lowest Miller indices Mg are given in Table 3.3. The equilibrium shape of Mg crystal is obtained using the Wulff plot construction using these surfaces energies as inputs. The computed Wulff shape is shown in Figure 3.3a. It can be seen from the Wulff shape that (0001), $(10\bar{1}0)$ and $(10\bar{1}1)$ surfaces are the only surfaces present in Mg at equilibrium conditions. The area fraction of each surfaces derived from the Wulff shape is given in Table 3.3. Even though (0001) surface is the most energetically favorable surface, most area of the equilibrium magnesium surface consists of the $(10\bar{1}1)$ surface.

System	SFE (mJ/m^2)	E_f^{bulk} (eV)	$E_f^{I_1\text{SF}}$ (eV)	$E_f^{(0001)}$ (eV)	$E_f^{(10\bar{1}1)}$ (eV)	$E_f^{(10\bar{1}0)}$ (eV)
Al	14.083	0.048	0.031	0.096	0.094	0.112
Ba	4.316	1.311	1.273	-0.343	-0.612	-0.580
Bi	-5.679	-0.245	-0.305	-0.779	-0.879	-0.909
Ca	14.084	0.126	0.109	-0.221	-0.330	-0.273
Ce	13.402	0.167	0.150	0.036	0.114	0.125
Cs	-2.044	2.833	2.781	-0.410	-0.573	-0.639
Dy	18.854	-0.010	-0.016	0.280	0.336	0.473
Er	19.081	0.001	-0.004	0.334	0.400	0.533
Eu	6.815	0.411	0.379	-0.209	-0.387	-0.310
Ga	15.219	-0.169	-0.183	-0.158	-0.227	-0.219
Gd	18.400	-0.016	-0.023	0.200	0.254	0.393
Hf	11.358	0.605	0.582	1.435	1.813	1.795
Ho	19.081	-0.007	-0.013	0.307	0.369	0.504
In	11.358	-0.367	-0.399	-0.464	-0.510	-0.501
K	5.452	1.593	1.558	-0.229	-0.380	-0.430
La	14.311	0.310	0.294	0.056	-0.028	0.112
Lu	18.627	0.024	0.018	0.390	0.485	0.612
Na	12.948	0.437	0.419	-0.072	-0.177	-0.218
Nd	15.447	0.080	0.067	0.109	0.096	0.238
Pb	3.407	-0.209	-0.249	-0.545	-0.624	-0.638
Pr	14.538	0.092	0.077	0.050	0.019	0.161
Rb	1.590	1.492	1.448	-1.047	-1.205	-1.256
Sc	18.172	-0.111	-0.118	0.329	0.503	0.523
Sm	17.037	0.031	0.021	0.170	0.186	0.327
Sn	3.862	-0.260	-0.299	-0.467	-0.531	-0.538
Sr	7.042	0.718	0.686	-0.217	-0.431	-0.373
Tb	18.627	-0.006	-0.013	0.256	0.305	0.443
Ti	13.175	0.649	0.630	1.213	1.479	1.429
Tl	11.131	-0.049	-0.072	-0.305	-0.367	-0.382
Tm	19.081	0.012	0.006	0.360	0.428	0.559
Y	18.854	-0.092	-0.098	0.173	0.253	0.377
Yb	11.358	0.282	0.260	-0.079	-0.220	-0.150
Zn	23.170	-0.033	-0.030	-0.015	-0.067	-0.080
Zr	11.131	0.192	0.169	0.999	1.376	1.354
Mg	21.547	-	-	-	-	-

Table 3.2. Calculated SFE and formation energies of the binary Mg alloys with the dopant in bulk, at stacking fault and on surfaces.

Surface	Surface energy (J/m^2)	Area fraction
(0001)	0.59	0.22
$(10\bar{1}0)$	0.63	0.34
$(10\bar{1}1)$	0.68	0.44
$(10\bar{1}2)$	0.75	0.00
$(11\bar{2}0)$	0.76	0.00
$(11\bar{2}1)$	0.80	0.00
$(20\bar{2}1)$	0.82	0.00
$(21\bar{3}0)$	0.75	0.00
$(21\bar{3}1)$	0.77	0.00
$(2\bar{1}\bar{1}2)$	0.80	0.00
$(21\bar{3}2)$	0.80	0.00
$(22\bar{4}1)$	0.80	0.00

Table 3.3. Surface energies and area fraction of 12 surfaces with the lowest Miller indices.

a) Wulff plot   b) (0001) Surface   c) $(10\bar{1}0)$ Surface   d) $(10\bar{1}1)$ Surface
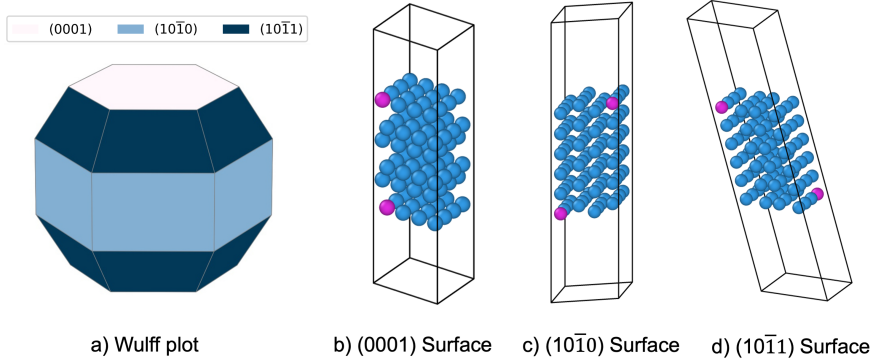
Figure 3.3. a) Wulff plot of the equilibrium surfaces of Mg. Slab structures used in the surface calculations. b) (0001) surface, c) $(10\bar{1}0)$ surface and d) $(10\bar{1}1)$ surface. Mg atoms are shown in blue and the dopants are shown in pink.

Thus, we only considered the (0001), $(10\bar{1}0)$ and $(10\bar{1}1)$ surfaces for our study of the propensity of a dopant to migrate to the surface. Again, for the sake of consistency, the formation energies with the dopants at the surfaces were calculated using 96-atoms slab structures with one dopant on each of the two surfaces. The (0001), $(10\bar{1}0)$ and $(10\bar{1}1)$ surface slabs

are visualized in Figure 3.3.

3.4.3   Stability analysis

The formation energy of the alloy with the dopant atom in the bulk, E_f^{bulk}, or at the stacking fault, $E_f^{I_1\mathrm{SF}}$, should be negative in order to form a stable alloy. As shown in Section 3.4.1, only 14 out of the 34 considered dopants fulfill that condition: Bi, Dy, Er, Ga, Gd, Ho, In, Pb, Sc, Sn, Tb, Tl, Y and Zn. It is worth noting that $E_f^{I_1\mathrm{SF}}$ is smaller than E_f^{bulk} for all dopants other than Zn, which indicates that these dopant are more favorable to be at stacking fault than in the bulk. Er is special case where it is stable only at the stacking fault – all the other stable dopants are stable both in bulk and at the stacking fault. In addition to the 14 dopants that fulfill our stability condition, some dopants such as Al, Lu, Nd, Pr, Sm and Tm display slightly positive values (i.e., less than $0.1\,\mathrm{eV}$ for E_f^{bulk} and $E_f^{I_1\mathrm{SF}}$. Due to the intrinsic errors in DFT, we took a cautious approach and decided not to exclude these 6 dopants at this stage from the pool of potential dopants that are beneficial for Mg-alloy anodes.

A screening based on the stability criterion allows us to disregard 14 out of the 34 dopant candidates. The disregarded dopants were alkali and alkali-earth metals, whose large atomic size compared to that of Mg makes them rather unstable, three rare-earth elements (Eu, La and Yb), and the elements in group 4 of the periodic table (Ti, Zr and Hf). Regarding elements from group 4, there are experimental reports in the literature confirming their low solubility in Mg.[60, 61, 62] One could argue the 14 excluded dopants could be metastable at the low doping level considered in this work due to kinetic considerations (e.g., high migration barriers), and they may not segregate to form a separate phase. However, under the operating conditions of the battery where Mg atoms are continuously plated/stripped from the anode, atomic migration is strongly favored, and thus the segregation of metastable dopants would eventually occur.

It is worth to mention explicitly the case of Ca, which was included in the study by Mandai and Somekawa. The Mg-0.3 wt% Ca showed a reduction of the overpotential relative to pure Mg.[23] Our calculation show

that Ca and Mg should segregate, which agrees well with experiments.[63] Mandai and Somekawa speculated that the low amounts of Ca dopant in their samples dissolve during the first cycles, producing defects that may function as active sites.

3.4.4   Relative energy analysis

As a final step of the analysis and screening, we evaluated the propensity of the 20 stable dopants to reside in bulk or at stacking fault than migrate to the (0001), (10$\bar{1}$0) or (10$\bar{1}$1) Mg surfaces. While using the surface at which the dopant is most stable as a reference, we evaluate the relative energies of the dopants in the bulk and at the stacking fault versus on the surface, which are respectively represented as ΔE^{bulk} and $\Delta E^{I_1\text{SF}}$. The results are shown in Figure 3.4.

Among the stable magnesium alloys, Al and most of the rare earth elements (Dy, Er, Gd, Ho, Lu, Nd, Sc, Sm, Tb, Tm and Y) have negative ΔE^{bulk} and $\Delta E^{I_1\text{SF}}$. The negative relative energies imply that these dopants are not prone to migrating to the surface, and thus they are electrochemically inert. In contrast, Bi, Pb, Sn, In and Tl strongly prefer to migrate to the Mg surface, which will interfere in the stripping
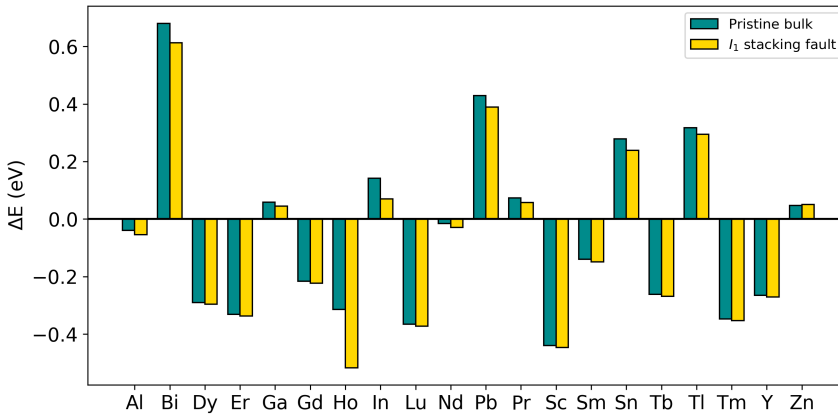
Figure 3.4. Relative energies of stable Mg alloys.

(deposition) of Mg during the discharge (charge) of the battery and potentially react with the electrolyte. Experiments have shown increased overpotentials for Bi and Pb dopants with respect to pure Mg.[23, 47]

It should be pointed out that the propensity of the dopants to migrate to the surface depends on the considered surface termination. For example, Zn and Ga have slightly positive ΔE^{bulk} and $\Delta E^{I_1\mathrm{SF}}$ values because they energetically prefer to be on the $(10\bar{1}0)$ or $(10\bar{1}1)$ surfaces. However, they are more stable to be in the bulk or at the $I_1\mathrm{SF}$ compared to the (0001) surface. Our results show a good agreement with the experimental results even for the borderline cases where the magnitudes of ΔE^{bulk} and $\Delta E^{I_1\mathrm{SF}}$ are small. The study of Schloffer et al. on the electrochemical behavior of Mg-1.63 wt% Zn in APC electrolyte reported that the alloy exhibits a high propensity to be passivated,[48] indicating that Zn participates in surface processes. Along the same lines, Mandai and Somekawa,[23] Zhao et al.[46] and Wang et al.[47] reported an increased overpotential in the AZ31 alloy, containing Zn, with respect to pure Mg. Schloffer et al. also showed that the addition of 1.55 wt% Gd does not have any adverse effect on the anode performance.[48] These experimental observations are in a good agreement with our findings where Gd does not migrate to Mg surfaces while Zn does.

Based on the identified dopants, the commercial alloy WE43 with a composition of Mg-4 wt% Y-2.25 wt% Nd-0.15 wt% Zr will be a suitable candidate as magnesium alloy anode. The two main dopants in WE43, Y and Nd, are both stable in the bulk, promote stacking faults and do not migrate to the surface. Zr is added to magnesium alloys as a grain refiner although it has limited solubility in magnesium; the undissolved Zr act as a nucleation site during solidification and form fine-equiaxed grains.[64] In contrast, the alloys in the AZ family (the most widely used type of commercial Mg alloys) contain Al and Zn, are expected to be unsuitable for Mg battery anodes as Zn tends to migrate to the surface.

3.5   Conclusion

We performed a theoretical study of 34 dopants reported in the literature as beneficial to improve magnesium ductility to explore their potential

use as anodes in magnesium batteries. We started by checking that the studied alloys at the doping level considered in this work ($\sim 2.08\,\%$) promote stacking faults defects, whose presence enhances magnesium ductility. Subsequently, we examined whether the dopants tend to segregate and form separate phases or prefer to remain in the alloy. We found that only 20 out of the 34 dopants, mostly rare-earth elements, are stable in the alloy. Finally, we investigated these 20 stable dopants and their propensity to migrate to the alloy's surface. We considered that those dopants that migrate to the surface could interfere with the electrochemical process (they could, for instance, produce passivation or degrade the electrolyte), and thus we disregarded them as useful dopants. Within this sequential analysis, we identified 12 potential favorable dopants: Al, Dy, Er, Gd, Ho, Lu, Nd, Sc, Sm, Tb, Tm and Y. Remarkably, the commercial alloy WE43 contains Y and Nd, both included in our shortlist of beneficial dopants, so we encourage experimental tests with this alloy.

3.6   Outlook

The commercial alloy (WE43) suggested in this work has been tested by our experimental partners in the EMAGIC consortium. They were not successful in rolling the alloy into thin foils. The main reason for this failed attempt was the use of wrought alloy rather than cast alloy. The criteria that we used in this study to evaluate the enhancement of ductility by the addition of doping that promotes stacking fault are only applicable for cast alloys that have a homogenous distribution of dopants and an unaltered microstructure. For wrought alloys, on the other hand, the microstructure has already been changed by mechanical processing during the making of the alloy.

CHAPTER 4

Sn Anode

This chapter presents the work in paper 2 - *Thermodynamic investigation of phase transformation in Sn anode for magnesium batteries.* The paper is included in this thesis. The text is taken directly from the paper with minor changes for the purpose of the thesis.

4.1   Introduction

The alloying anode materials for Mg batteries such as Sn,[25] In,[26] Pb,[27] Bi,[65] and their intermetallics have recently been proposed as a new class of anode materials for Mg-ion batteries to address the issues of incompatibility with the conventional electrolytes. These alloying anodes are shown to be compatible with a wide range of conventional electrolytes and are less susceptible to the passivation layer formation.[24, 25, 66] Among the alloying anodes, Sn appears to be a promising anode because of its high gravimetric capacity, ductility and low intercalation voltage.[25] A theoretical study by Wang et al.[67] indicated that Sn has a relatively low migration barrier for Mg^{2+} ions, making it a competitive anode for RMBs.

Sn exists in two allotropic forms: α- and β-Sn. The ground-state structure of Sn is a face-centered cubic (fcc) with a diamond crystal structure known as a α-Sn phase, which is a zero-gap semiconductor.[68] At a transition temperature of 13 °C, α-Sn transforms into β-Sn phase, a body-centered tetragonal (bct) metal[69]. Most experimental studies of Sn are based on the β-Sn as it is the stable phase at room temperature. The β-Sn structure becomes Mg_2Sn with fcc structure upon magnesiation.[25]

Significant volume change during charge and discharge is a known issue of Sn.[17, 70] The structural distortion due to the volume change

leads to poor coulombic efficiency and rapid capacity degradation. [71]
The underlying reasons for how the structural changes hamper electro-
chemical performance remain unclear. Singh et al.[25] indicated that
amorphization, accompanied by the structural transformation, hinders a
complete extraction of Mg^{2+} from Mg_2Sn, which leads to poor coloumbic
efficiency and fast capacity fade. The first step of improving the perfor-
mance of Sn anode is to gain an in-depth understanding of the phase
transformation process during charge and discharge, which can be used
for designing future anode materials.

The aim of this study is to investigate the phase transformation from
pure Sn (bct) to Mg_2Sn (fcc) on magnesiation. While the β-Sn and
Mg_2Sn are the only two known crystalline phases during the cycling of
Sn anode, no detailed information is available for the transformation from
bct to fcc structures. This study investigates the relative thermodynamic
stability of the bct to fcc phase at intermediate magnesiation levels. The
cluster expansion (CE) method coupled with first-principle densiy func-
tional theory (DFT) calculations have been proven to predict the struc-
tures formed during the battery charging and discharging.[72, 73, 74] Pre-
vious CE study on Mg-Sn alloys only considers hcp and fcc structures,[75]
while overlooking the bct structure, which is known to be the most sta-
ble phase for pure Sn.[69] The present work is the first theoretical study
that includes the missing bct structure in the phase analysis. The hcp
phase has not been considered in this study as it is not present during
the charge-discharge process of the RMBs. Two CE models are devel-
oped to determine the most thermodynamically stable phase at different
Mg concentration levels by comparing the formation energies of bct and
fcc structures. In addition, we simulated the voltage profile using Monte
Carlo simulations to gain more insights into how the thermodynamic
stability of the materials is related to their performance.

4.2   Method

First-principle calculations based on DFT were employed to calculate
the total energies of all structures. DFT calculation results are used
to train CE models, and all of the calculations were performed using

the Vienna Ab initio Simulation Package (VASP).[54, 55] The Perdew-Burke-Ernzerhof (PBE) parameterized generalized gradient approximation (GGA) functional was employed to describe the exchange and correlation effects, and the projector augmented wave (PAW) method was used to account for the core-valence interactions.[41, 56] A plane-wave basis set with cut-off energy of $520\,\mathrm{eV}$ is used for the calculations. The Brillioun zone is integrated with the k-point mesh generated using the Monkhorst-Pack scheme with a k-point density of 4 per $\mathrm{\AA}^{-1}$.[76] The convergence threshold for electronic degrees of freedom was $1 \times 10^{-6}\,\mathrm{eV}$, and the interatomic forces were set to $1 \times 10^{-2}\,\mathrm{eV\,\AA}^{-1}$ for the structural relaxation.

We developed two separate CE models for α-Sn and β-Sn systems, where both of them are trained using corresponding DFT calculations. For simplicity, we refer to α-Sn and β-Sn systems as fcc and bct structures, respectively, based on their parent lattice structures. The energies from the first-principle calculations were then used to build the CE model to explore the configurational space more effectively. The CLuster Expansion in Atomic Simulation Environment (CLEASE) package was used to generate training structures for DFT calculations and to construct the CE model by fitting the effective cluster interactions (ECIs).[73] The training structures were generated systematically using different generation schemes provided in the CLEASE package. The first set of structures was generated using a random generation method. The subsequent structures are generated to ensure that energetically stable structures are included in the training set while the configurational space is sufficiently explored. Two generation schemes are employed for this work; a probe structure [77, 78] scheme was used to generate structures that differ the most from the existing training set in the database and the ground-state structure generation scheme based on simulated annealing was used to include low-energy structures.[79]

A template lattice structure describing the substitutional disorder is needed to construct a CE model. A structure with a space group 216 (shown in Figure 4.1a) is used to represent fcc structures (α-Sn and Mg_2Sn) as it is the common subgroup with the highest symmetry for the space groups of Mg_2Sn (space group 225) and Sn (space group 227). The structure becomes α-Sn when 4b and 4c Wyckoff positions are occupied

by Sn and vacancy, respectively. The Mg_2Sn structure can be realized using the template when 4b and 4c positions are occupied by Mg. The charging procedure can be mimicked by letting the 4b sites be occupied by either Mg or Sn while the 4c sites are occupied by either Mg or vacancy. A total of 200 structures are generated for the fcc structures while applying the above site constraints. The 200 structures consists of structures with a conventional cell ($1 \times 1 \times 1$ cell consisting of 12 atoms), $2 \times 1 \times 1$ cell (24 atoms) and $2 \times 2 \times 1$ cell (48 atoms).

A template structure with space group 141 was used to construct the CE model for bct structures (shown in Figure 4.1b) as the β-Sn has a bct crystal structure with the space group 141. There is no imposed constraint for the occupation of the lattice sites, which means any of the lattice sites can be occupied by either Mg or Sn. It is known from experiments that the solubility of magnesium in bct Sn is very low.[80, 81] Therefore, we limited the magnesiation concentration in the bct structure to be up to 12.5% Mg to allow for a thorough sampling at low Mg concentration. We generated 170 bct structures with the Mg concentration below 12.5% to train the CE model. The CE models for bct and fcc structures were constructed using the maximum cut-off radii of 9, 9, and 7 Å for the 2-body, 3-body, and 4-body clusters, respectively. Two regularization schemes, ℓ_1 and ℓ_2 types, are compared for its predictive power, which is evaluated using leave-one-out cross-validation (LOOCV) score.

One technical issue for constructing an accurate CE model is the large lattice distortion after the structure relaxation, which originates from the presence of vacancies or large mismatch in atomic radii of elements that occupy the lattice. The lattice distortions introduce "noise" in the CE model, which assumes an ideal lattice structure. One strategy to alleviate the issue of lowered accuracy is to eliminate the heavily distorted structures. [75, 82, 83] The lattice distortion can be quantitatively measured using normalized mean square displacement (NMSD), which is described as[82]

$$\text{NMSD} = \frac{\text{MSD}}{\text{V}^{\frac{2}{3}}}, \tag{4.1}$$

where V is the volume of the structure and MSD is the mean square
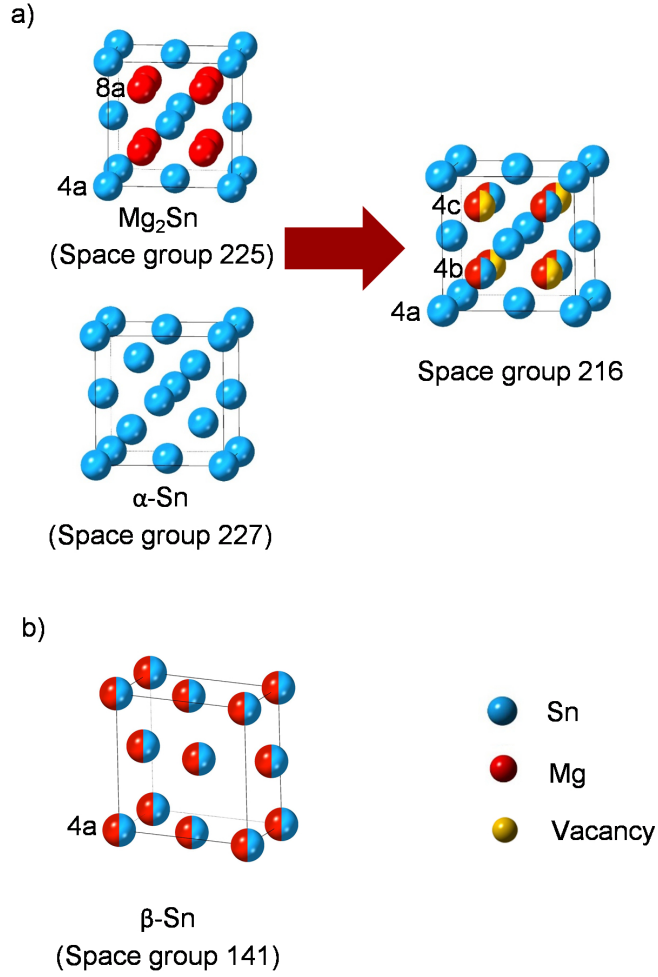
Figure 4.1. a) Structures of Sn and Mg$_2$Sn, which can be represented using a common template with space group 216. b) Template with space group 141 for bct structures.

displacement calculated using

$$\text{MSD} = \frac{\sum_{\text{atom}} \sum_{X=x,y,z} (X[f] - X[i])^2}{N_{\text{atom}}}.$$ (4.2)

$X[f]$ and $X[i]$ are Cartesian coordinates of final relaxed structure and initial unrelaxed structure, respectively, and N_{atom} is the total number

of atoms in the structure. The structures with a high value of NMSD (i.e., heavily distorted structures) are removed from the training set to construct a CE model without much distortion noise.

Monte Carlo (MC) simulations were performed using the constructed CE model to investigate the relative stability of fcc and bct structures and to obtain the voltage profile.[74, 84] We used canonical MC at various fixed concentrations for the phase stability analysis. The lowest energy structure for each concentration was obtained using a simulated annealing technique. The starting temperature of the MC simulations was set to 1×10^{10} K, which was gradually lowered to 2 K. A $5 \times 5 \times 15$ supercell consisting of 1200 atoms was used for the fcc structures, while a $6 \times 6 \times 9$ supercell consisting of 1296 atoms was used for bct structures.

The relative stability of the phases investigated using convex-hull analysis. The formation energy for the construction of convex hull is calculated using the following equation:

$$E_f = E_{\mathrm{Mg_xSn}} - X_{Mg}E_{\mathrm{Mg}} - X_{Sn}E_{\alpha\text{-Sn}}, \tag{4.3}$$

where $E_{\mathrm{Mg_xSn}}$ $(0 < \mathrm{x} < 2)$ is the total energy of the structure and X_{Mg} and X_{Sn} are the concentration of Mg and Sn in the structure, respectively. E_{Mg} and $E_{\alpha\text{-Sn}}$ are the energy per atom of pure Mg (hcp) and α-Sn, respectively.

The open-circuit voltage (OCV) profile was obtained using semi-grand canonical Monte Carlo (sgcMC) simulations. The sgcMC has the advantage of controlling the concentration of the system by imposing fixed chemical potential. Each trial move in sgcMC simulation consists of selecting a random site and substituting the site with a different element, which makes the concentrations of species in the cell to fluctuate from one point to another. The chosen value of chemical potential controls the average concentration of species. The sgcMC simulations presented in this work require two chemical potential values since there are two binary sub-lattices in the simulation cell that consists of Mg-Sn and Mg-vacancy. Throughout this work, the two sub-lattices were kept in internal equilibrium by constraining the chemical potential of Mg to be the same on both of the two sub-lattices. This constraint allows us to control the Mg concentration by varying one chemical potential. This chemical potential can directly use to calculate the OCV of the half-cell consisting of Mg and Sn electrodes (Sn electrode is the material under study, which is

magnesiated up to Mg_2Sn). The OCV is calculated using the following formula:

$$\text{OCV} = -\frac{\mu_{\text{Mg}}^{\text{Mg}_x\text{Sn}} - \mu_{\text{Mg}}}{e}. \qquad (4.4)$$

$\mu_{\text{Mg}}^{\text{Mg}_x\text{Sn}}(0 < \text{x} < 2)$ is the chemical potential in eV per Mg atom in Mg_xSn (this is the chemical potential obtained from sgcMC), μ_{Mg} is the energy per atom of the pure Mg in hcp crystal structure calculated as $-1.5095\,\text{eV}$ and e is the electric charge which is 2 for Mg^{2+} ion. The same settings were used for the simulated annealing for the sgcMC simulations, except for the use of a $10 \times 10 \times 10$ supercell consisting of $12\,000$ atoms for simulating fcc structures. The large supercell was used to allow the system to explore very low magnesium concentrations as a dip in voltage is observed in the experimental voltage profile at low magnesium concentrations.[25]

4.3   Results and discussion

4.3.1   Cluster expansion

As the first step of constructing the CE model, the relaxed structures from the DFT simulations are examined to determine their NMSDs to quantitatively investigate their degree of distortion. The lattice distortion of relaxed structures in the considered magnesium range and their distributions are shown in Figure 4.2. The Mg concentration ranging from 0 to ~67 % and from 0 to 12.5 % are considered for fcc and bct structures, respectively. It is noted that lattice distortion is low in the vicinity of known stable concentrations (α-Sn and Mg_2Sn for fcc structures and β-Sn for bct structures). The heavily distorted structures tend to be present in the concentration ranges that deviate significantly from the known stable structures (i.e., α-Sn, β-Sn and Mg_2Sn). The inclusion of these heavily distorted structures in the training set has been shown to have an adverse effect on the predictive power of the CE model.[75, 82] In particular, Nguyen et al.[82] demonstrated that the accuracy of the CE model improves when it is trained with structures with the NMSD

value of less than $0.1\,\%$.[82] Of the 200 fcc and 170 bct structures, 106 fcc and 71 bct structures had the NMSD values below $0.1\,\%$.
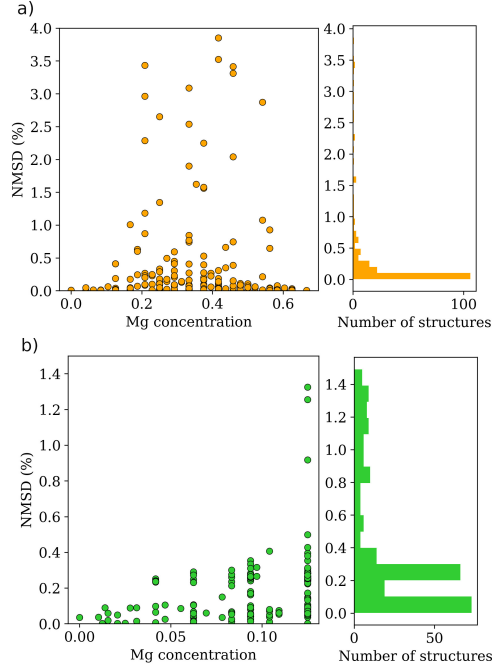
Figure 4.2. Distortion of the structures based on the normalized mean square displacement (NMSD) values for a) fcc system b) bct system.

The effect of filtering out the distorted structures is verified by comparing the performances of the CE models constructed with and without the distorted structures. The performance is measured using the LOOCV score, and the NMSD value of $0.1\,\%$ is used as a threshold to filter out the distorted structures. The LOOCV score of CE models with and without distorted structures is given in Table 4.1. Two commonly used regularization schemes, ℓ_1- and ℓ_2-regularized fits, are used for obtaining the LOOCV scores. The LOOCV score of the fcc system improved substantially upon the removal of the highly distorted structures; the LOOCV score improved from $24.95\,\mathrm{meV/atom}$ to $6.59\,\mathrm{meV/atom}$ for the ℓ_1-regularized fit and from $25.89\,\mathrm{meV/atom}$ to $5.89\,\mathrm{meV/atom}$ for the ℓ_2-regularized fit. The improved LOOCV scores agree well with the findings of Nguyen et al..[82] The difference in the LOOCV for ℓ_1- and

ℓ_2-regularized fits is negligible, and they deliver similar MC simulation results and convex hull diagram. The key difference is in the number of ECI terms used in the CE model. The ℓ_1-regularized fit yields a lower number of ECIs, leading to a reduced computational time for the subsequent MC simulations. Consequently, the CE model constructed using the ℓ_1-regularized fit was used for the subsequent MC simulations for the fcc system.

	All structures			Undistorted structures		
	No. structures	LOOCV (meV/atom)		No. structures	LOOCV (meV/atom)	
		ℓ_1	ℓ_2		ℓ_1	ℓ_2
fcc	200	24.95	25.89	106	6.59	5.89
bct	170	13.66	4.39	71	13.31	3.7

Table 4.1. LOOCV score for the CE models of the fcc and the bct structures before and after removing distorted structures. LOOCV scores with ℓ_1- and ℓ_2-regularized fits are given for all models.

No significant improvement in the LOOCV is found for the bct system upon the removal of the distorted structures. Despite the lack of significant change in the LOOCV score, it is observed that the structures with high NMSD values relax into different space groups. The structures with high NMSD values are discarded from the training set since the relaxed structures no longer correspond to the original lattice model. In other words, we only used the structures in the training set that remain to have the same space group as we specified. It is evident from the Table 4.1 that the LOOCV score with ℓ_1 regularization is significantly higher than those with ℓ_2 regularization. Hence, the ECIs based on ℓ_2-regularized fit is used for the MC simulation of the bct system.

4.3.2   Convex-hull analysis

The stable structures at different levels of magnesiation are identified through convex-hull analysis. The convex-hull plot obtained from DFT calculations without distorted structures for bct and fcc structures are shown in Figure 4.3a, and the one from the canonical MC based on CE

models trained with this DFT dataset is shown in Figure 4.3b. It can be seen from both convex-hull plots that α-Sn (fcc) is more stable than the β-Sn (bct), which agrees with experimental and theoretical studies that α-Sn is the stable phase at low temperatures (temperature below 13 °C).[69, 85] Furthermore, the fcc structures are energetically more favorable for the entire magnesiation levels considered. The canonical MC simulation for bct structures predicts a new phase when Mg concentration is around 11 % (Figure 4.3b). However, the relative energy of this phase with respect to the fcc is high, which indicates that this phase will not form at low temperatures. Jain et al.[86] reported an Mg_9Sn_5 phase to be thermodynamically stable. This phase is not observed in our convex hull since we only considered the structures in space groups 225 and 141. We calculated the formation energy of this structure and observed that this structure falls on the hull line. However, this structure is reported as a high temperature and pressure phase and will not form under normal operating conditions of batteries.[87]

The vibrational contributions should be added to the formation energies to compare the bct and fcc systems at temperatures higher than 0 K. As the phonon calculations using DFT are computationally expensive, we include the vibrational contribution from the study of Legrain and Manzhos[85] on α-Sn and β-Sn based on DFT and the harmonic approximation. They calculated the difference in vibrational contribution to energy between β-Sn and α-Sn at transition temperature is 0.024 eV/atom. The difference in energy is subtracted from the energies of all the bct structures to include the vibrational contributions effectively. This approximation is valid since our training set consists only of low Mg concentration structures and stays in the original parent lattice after discarding the highly distorted structures.

The convex-hull plots after including the vibrational contributions to DFT and canonical MC results are shown in Figure 4.3c and d, respectively. The energies of α-Sn and β-Sn become almost the same upon the inclusion of the vibrational contribution corresponding to the transition temperature. The updated convex-hull plots show that Sn and Mg_2Sn are the two stable phases upon alloying Sn with Mg. Furthermore, it can be seen from the convex-hull plots that no other stable intermediate states are present during the charging of Sn electrode to Mg_2Sn. The energies of fcc and bct structures overlap slightly only when Mg concen-
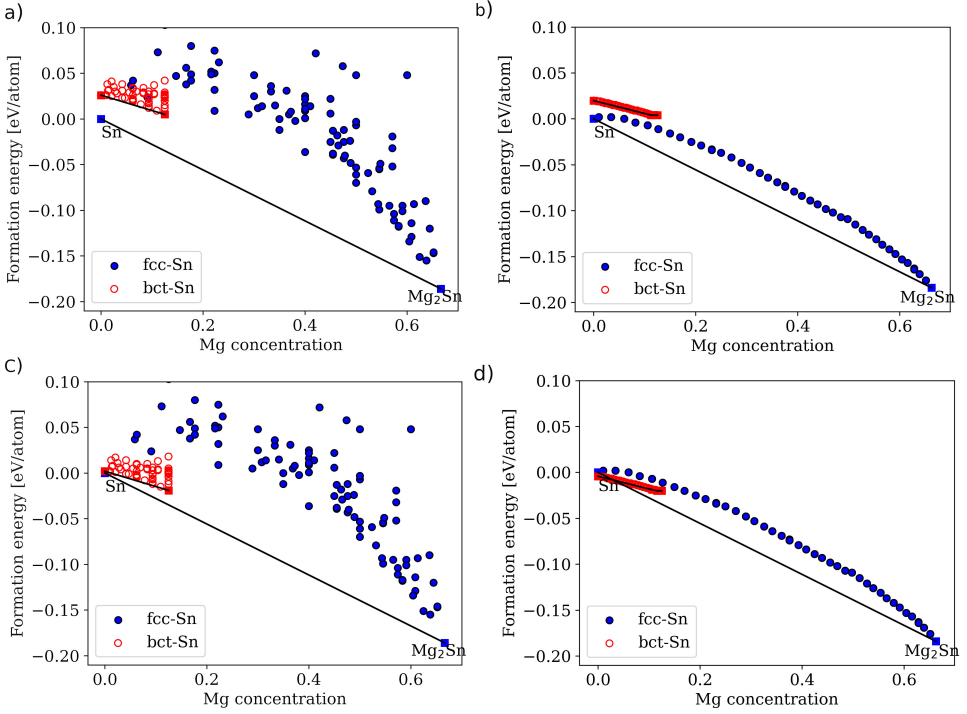
Figure 4.3. Convex hull from a) DFT calculations, b) canonical MC simulations, c) DFT calculations with $0.024\,\mathrm{eV/atom}$ subtracted from the energy per atom of bct structures to include the vibrational contribution and d) canonical MC based on CE model trained with vibrational contributions added DFT dataset.

tration is very low, and the fcc structures become more stable as the Mg concentration is increased, indicating that bct structures are only stable when Mg concentration is negligible. The results indicate that the nucleation of Mg_2Sn (fcc) will take place upon adding Mg to β-Sn. Legrain et al.[88] have shown that low-concentration doping of Mg is unfavorable in both α-Sn and β-Sn, i.e., Mg prefers to segregate when doped in low concentration in these phases. Although doping of Mg is unfavorable in both phases, β-Sn exhibits lower defect formation energy relative to that of α-Sn, indicating that doping in β-Sn phase is more stable. A similar trend can be observed in the present study as the system at low Mg concentrations is above the hull line (Figure 4.3 b and d), and the

formation energies of low-concentration Mg in β-Sn are lower than those of α-Sn. We only considered the vibration contribution corresponding to the transition temperature 13 °C, but a similar approach can be used to study the phase transformation at higher temperatures. It is worth noting that the energy difference between the α-Sn and β-Sn without any vibrational contribution ($\Delta E_{\alpha-\beta}$) is 0.026 eV/atom in our study. This matches with the $\Delta E_{\alpha-\beta}$ value of 0.02-0.06 eV/atom reported in the previous DFT studies. [85, 86] Legrain and Manzhos[85] pointed out that slight changes in the $\Delta E_{\alpha-\beta}$ can lead to a large difference in the transition temperature, and they obtained a $\Delta E_{\alpha-\beta}$ value of 0.04 eV/atom using GGA functional. The $\Delta E_{\alpha-\beta}$ value of 0.026 eV/atom calculated in the present study is slightly lower than the value reported in their study. A larger $\Delta E_{\alpha-\beta}$ value will result in pushing the formation energies of β-Sn in Figure 4.3 upwards, making it less stable compared to the α-Sn.

4.3.3   Open-circuit voltage profile

The thermodynamic stability of the phases studied using the convex-hull plots is directly related to the voltage profile of batteries. The voltage profile obtained from the sgcMC simulation is shown in Figure 4.4. The voltage plateau at 0.15 V obtained from the sgcMC matches the experimental value reported by Singh et al.[25]. In their results, a slight dip in the voltage was observed at the beginning of magnesiation, which could originate from the kinetics of the bct to fcc transition. Since we only considered the thermodynamics of the phase transformation, the dip is not observed in the simulated voltage profile. The flat voltage profile predicted by the MC simulations indicates that the anode material is phase-separated during charging and discharging.

The magnesium solubility in Sn is low,[80, 81] which could be a possible cause of the formation of two phases rather than a solid solution. The flat voltage profile is consistent with the convex-hull analysis, where no phases other than Sn and Mg_2Sn are observed. The single-phase β-Sn becomes phase-separated between β-Sn and Mg_2Sn during charge. At the end of the charging, the system becomes a single-phase Mg_2Sn. Some studies suggest that an amorphous phase can form during the transformation from Mg_2Sn to β-Sn upon discharge.[25, 89] Some of the highly
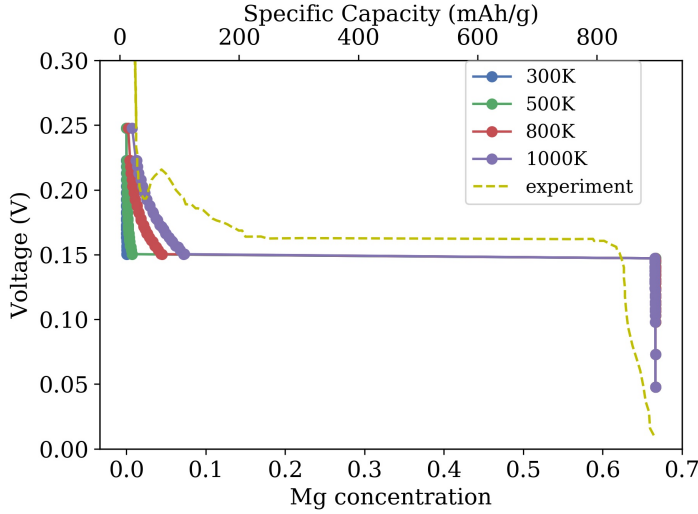
Figure 4.4. Voltage profile obtained from semi grand canonical MC simulation for fcc structures. The dotted line is the experimental voltage profile from ref.25.

distorted structures discarded for CE training had low formation energies that lie close to the convex hull, indicating that the system could transform into an intermediate phase (possibly an amorphous phase as indicated in previous experimental studies) during the charging/discharging of the battery. A sufficiently slow discharge process can transform Mg_2Sn to β-Sn without losing its crystalinity. This transformation can happen via two possible routes. The first route is Mg_2Sn transforms to α-Sn upon demagnesiation as they share a common parent lattice with space group 216 (Figure 4.1 a), followed by a transformation from α-Sn to β-Sn (i.e., $Mg_2Sn \rightarrow \alpha$-Sn $\rightarrow \beta$-Sn). However, it is not clear whether α-Sn to β-Sn transformation is massive or martensitic. Mitchell and Donnelly[90] reported that the α to β transformation is highly likely to be massive in nature due to the absence of a specific orientation relationship. Ojima et al.[91], on the other hand, suggested that the transformation is mainly massive but also martensitic. The discrepancy indicates that a detailed study on the transformation from α-Sn to β-Sn is required. The second route is a direct transformation from Mg_2Sn structure to

β-Sn upon demagnesiation without an intermediate α-Sn (i.e., Mg$_2$Sn $\rightarrow$ β-Sn). As shown in Figure 4.3 c and d, the low-concentration Mg structures in the β-Sn phase has lower formation energies than those in the α-Sn phase, indicating the feasibility of taking the second route of bypassing the α-Sn phase entirely. We performed a DFT calculation to test the thermodynamic feasibility of the direct transformation from Mg$_2$Sn to β-Sn. A full structure relaxation calculation was carried out on a structure where all the Mg atoms in Mg$_2$Sn are removed from the cell, followed by a slight rattling of all the atoms. The structure relaxed to a tetragonal crystal structure which is very similar to pristine β-Sn. The current work focuses on the thermodynamic stability of the phases present during the cycling of the Sn anode in RMBs. Further work on the kinetics of these phases to understand the transformation pathway is underway.

4.4   Conclusion

We investigated the phase transformation of Sn anode for RMBs using two DFT-based CE models to analyze the energetics of bct and fcc structures. This is the first time the energetics of fcc and bct phases are evaluated in the same framework to study the phase transformation in Mg-Sn alloy. We performed canonical MC to obtain the convex-hull plots and sgcMC to obtain the open-circuit voltage profile. The phase stability analysis using the convex-hull plots demonstrates that bct structures are only stable at very low magnesium concentrations. The bct-Sn starts to transform into Mg$_2$Sn upon magnesiation. The voltage profile obtained from sgcMC simulations shows the voltage plateau that is consistent with the value reported in previous experiments. The flat voltage profile obtained from sgcMC is consistent with the phase stability analysis where the material remains phase-separated between β-Sn and Mg$_2$Sn during the charging and discharging of the battery. The highly distorted structures discarded in the CE model had low formation energies, suggesting that the material could transform into an amorphous phase during cycling. Our novel approach considers the three possible routes for the transformation from Mg$_2$Sn to β-Sn in this study. The

first route is the transformation via an intermediate α-Sn phase (Mg$_2$Sn $\rightarrow$ α-Sn $\rightarrow$ β-Sn). The second route is the direct transformation from Mg$_2$Sn to β-Sn (Mg$_2$Sn $\rightarrow$ β-Sn). The third route is via an intermediate amorphous phase (Mg$_2$Sn $\rightarrow$ amorphous phase $\rightarrow$ β-Sn). Further study is needed to understand the kinetic barrier and the phase transformation pathways.

4.5   Outlook

In this study, the highly relaxed structures were discarded as they were affecting the predictability of the CE model. The phase space was therefore restricted to fcc and bct structures. Some of the highly relaxed structures that deviate from the original parent lattices show low formation energy. Therefore, it is desirable to develop a model that incorporates lattice change and can efficiently explore the phase space.

Part II

Cathode

CHAPTER 5

MgS transport properties

This chapter presents the work in paper 3 - *Ab-initio Study of Charge Transport in Mg-S battery Cathode*. The paper in its current form included in this thesis. The text is taken directly from the paper with minor changes for the purpose of the thesis.

5.1   Introduction

Rechargeable metal-sulfur batteries such as Li-S, Al-S, Mg-S, and Ca-S are receiving significant interest as potential next generation batteries due to their low cost, environmental sustainability and abundance of sulfur.[92, 93, 94, 95] In addition, metal-sulfur batteries offer high theoretical energy densities owing to their use of metal as an anode and high-capacity sulfur as the cathode. Li-S ($2654\,\mathrm{W\,h\,kg^{-1}}$ and $2856\,\mathrm{W\,h\,L^{-1}}$) and Mg-S ($1684\,\mathrm{W\,h\,kg^{-1}}$ and $3286\,\mathrm{W\,h\,L^{-1}}$) have the highest energy densities among the most studied metal-sulfur batteries.[92, 96]. Mg-S battery has the advantage over the Li counterpart; in addition to the abundance and lower cost, [92, 97, 98] the dendrite-free nature of Mg makes it a safer alternative,[16, 99] attracting much attention as a next-generation battery. Mg-S batteries have the potential to become a cost-effective, sustainable and safe alternative to Li-ion and Li-S batteries.

Despite the promises of Mg-S batteries, it is not free of technical challenges that must be overcome before being used in practical applications. One of the major challenges is the poor cyclability of the sulfur cathode, where the magnesiation process upon discharge is not highly

reversible. More specifically, Mg^{2+} ions migrate from the Mg anode to sulfur cathode during discharge, forming various high-order polysulfides (e.g., MgS_8, MgS_6, and MgS_4), which get further reduced to form the final discharge products, MgS and MgS_2.[100] The formation of these high-order polysulfide intermediates occur at a fast rate due to their high solubility in the electrolytes.[101] However, the further reactions to lower-order (poly)sulfides become slower as they start to precipitate on the sulfur cathode.[102] Furthermore, these low-order (poly)sulfides have exhibit low Mg^{2+}-ion diffusivity, leading to a large overpotential at the trailing end of the charging process, as well as limited reversibility to high-order polysulfides and sulfur during charge.[103] Thus, understanding the charge transport properties in MgS and MgS_2 is very important in designing an efficient Mg-S battery with long cycle life.

Presently, the charge transport mechanism in MgS and MgS_2 is not fully understood. Although few experimental and computational studies exist for MgS, the study of charge transport in MgS_2 is left unexplored. Most experimental studies on the charge transport in MgS have been performed at temperatures above $900\,K$.[104, 105] The conductivity at room temperature is more important for battery applications. Presumably, the lack of conductivity measurement of MgS around room temperature stems from the difficulties in determining its low conductivity due to its insulating nature. Several computational works also investigated the charge transport in MgS. Puntambekar et al. computed the activation energies for the diffusion of Mg^{2+} ($2.6\,eV$) and S^{2-} ($3.4\,eV$) ions in MgS using an empirical interionic potential model.[106] Using density functional theory (DFT), Chen et al. calculated the diffusion barrier of $1.2\,eV$ for Mg^{2+} ions in MgS.[107] These studies mainly focused on the ionic transport, and only little effort was devoted to studying electronic transport. The present study aims to elucidate the charge transport mechanism in MgS and MgS_2 using first-principles DFT calculations at the hybrid functional level of theory. More precisely, we study the ionic and electronic conductivity arising from the migration of charged point defects and polaronic defects (electron and hole polarons), respectively. The formation energies and equilibrium concentration of several point defects and polarons are calculated to identify the dominant defects. Further, the diffusion barrier for the prevalent defects are evaluated using nudged elastic band (NEB) method. The calculated energy barrier is

then used to estimate the maximum thickness of MgS and MgS$_2$ layers to achieve practical discharge rates. The transport mechanism under the non-equilibrium conditions during the battery operations, i.e., the injection or extraction of polarons and Mg^{2+} from the cathode, is also investigated using ab-initio molecular dynamics (AIMD).

5.2   Methodology

5.2.1   Computational details

All of the first-principle DFT calculations were performed using Vienna Ab initio Simulation Package (VASP).[54, 55] The commonly used PBE functional[41] is known to severely underestimate the bandgaps of semiconductors and insulators, as well as not predicting the charge localization reliably (i.e., the charges are often delocalized).[108] Therefore, we used the screened hybrid functional of HSE06[42, 109] for the calculation of formation energies and diffusion barrier for the defects. The α value was set to 0.40 (i.e., incorporating 40 % exact exchange) to reproduce the bandgap values of GW-level calculations, which is known to be more accurate.[110] All of the calculations used a plane wave basis for the electronic wave functions with a cut-off energy of 520 eV, and the projector augmented wave (PAW) method was used to account for the core-valence interactions.[56] All calculations are spin polarized, and the atomic positions are relaxed until the forces acting on each atoms are less than 1×10^{-1} eV Å^{-1}. The convergence threshold for electronic self-consistent loop was is set to 1×10^{-6} eV Å^{-1}.

The calculations for the bandgap, dielectric constant and chemical potential are performed with primitive unit cells. For these systems, the Brillouin zone was sampled with a dense Γ-centered k-point mesh with a minimum k-point density of 4 per Å^{-1}. The defect and mobility calculations were carried out using a $2 \times 2 \times 2$ supercell of the conventional cell with single Γ-centered k-point.

5.2.2   Defect formation energy

The likelihood of the defect formation was evaluated using the formation energy, E_f, of a defect, X. The E_f of X in charge state, q, was calculated according to

$$E_f(X^q) = E(X^q) - E_0 - \sum n_i \mu_i + q\epsilon_f + E_{\text{FNV}}. \qquad (5.1)$$

E_0 and $E(X^q)$ and represent the total energy of the pristine cell and the computational cell containing a point defect in charge state q, respectively. n_i is the number of atoms of species, i, removed while creating the defect, X. The value of n_i becomes negative when a species is removed from the cell during the defect creation. μ_i denotes the chemical potential of species i, which is determined by the phases that are in thermodynamic equilibrium with the material under study at $0\,\text{K}$. ϵ_f is the equilibrium Fermi energy of electrons, and E_{FNV} is the Freysoldt-Neugebauer-Vanderwall (FNV) correction for charged systems.[111] The FNV correction requires a dielectric constant of the material under investigation, which is calculated using density functional perturbation theory.

The Python Charge Defects Toolkit (PYCDT) package[112] was used to generate the input structures and VASP settings files for the point defect calculations. The input structures for the polaronic defect calculations, on the other hand, were prepared manually by distorting the local surrounding of the region where polaron localization is as it is often . To localize polarons in DFT calculations, typically, it is necessary to prepare the structures by manually distorting the local surroundings of the region where polaron localization is anticipated.

The concentration of defects, $c(X^q)$, was calculated using

$$c(X^q) = N \exp\left(\frac{-E_f}{k_B T}\right), \qquad (5.2)$$

where N is the number of equivalent sites of the defects, k_B is the Boltzmann constant and T is the temperature in kelvin. The mobility of defect, μ, was calculated using

$$\mu = \frac{\nu q a^2}{k_B T} \exp\left(\frac{-E_b}{k_B T}\right), \qquad (5.3)$$

where ν is the attempt frequency of the hopping, a is the hopping distance and E_b is the diffusion barrier. The attempt frequency, ν, was taken as $1 \times 10^{13}\,\mathrm{s}^{-1}$ for both S and Mg.[113] a is the distance between the initial and final points of the defects taken from DFT. The diffusion barrier is calculated using nudged elastic band (NEB)[114] method implemented in the atomic simulation environment (ASE) package.[115]. Then using $c(\mathrm{X}^q)$ and μ the equilibrium conductivity of the defects are calculated using

$$\sigma = qc(\mathrm{X}^q)\mu \tag{5.4}$$

The maximum diffusion length of a defect is calculated using

$$L = \sqrt{Dt} \tag{5.5}$$

where D is the diffusion coefficient, $D = \mu K_B T$, and t is the time for charge or discharge of battery

5.2.3   Molecular dynamics

The dynamics of the low energy barrier defects were analyzed using AIMD simulations. The dynamics of the defects in non-equilibrium conditions is evaluated using AIMD simulation. The molecular dynamcis (MD) calculations were performed in a canonical ensemble (NVT) at $350\,\mathrm{K}$, which is maintained by Langevin thermostat as implemented in ASE. The MD simulations used the same VASP settings as static DFT calculations for defect formation, except for the use of the PBE functional to keep the computational cost of the MD calculations reasonable. The simulation is run with a time step of $1\,\mathrm{fs}$ and equilibriated for a time period of $0.5\,\mathrm{ps}$ for all cases, unless it is explicitly mentioned otherwise.

5.3   Results and discussion

5.3.1   Crystal structure and bandgaps

The crystal structures of MgS and MgS_2 are illustrated in Figure 5.1. The MgS exist as rocksalt crystal structure (spacegroup Fm-3m) in which
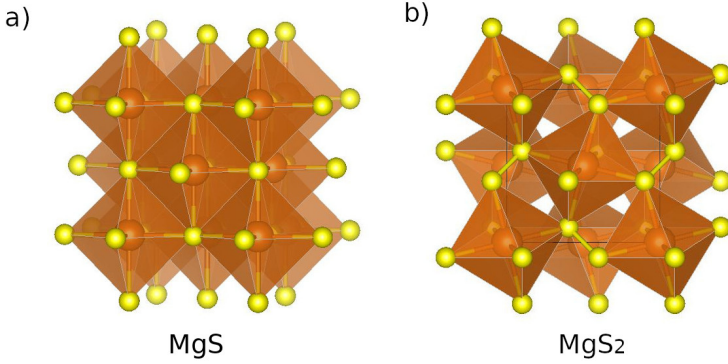
Figure 5.1. The crystal structure of a) MgS and b) MgS_2. Brown and yellow correspond to Mg and S ions, respectively.

the Mg^{2+} cations are octahedrally coordinated by S^{2-} anions. The most stable structure for MgS_2 is reported to be cubic pyrite structure (space-group Pa-3).[116] This is a modified rocksalt structure in which the S^{2-} anions of the rocksalt structure (MgS) is replaced by a S_2^{2-} dianions (S dimer). The calculated lattice constant value for MgS using HSE06 is 3.66 Å, which matches well with the experimental value of 3.67 Å.[117]

MgS and MgS_2 bandgaps were computed using DFT at three distinct levels of theory, namely G_0W_0, GW_0 and HSE06. The computed bandgaps are given in Table 5.1. It has been demonstrated that the GW_0 approach best describes the band gap of semiconductors and insulators.[110] Thus the α value of HSE06 ($\alpha=0.4$) functional was calibrated to reproduce the GW_0 bandgaps, and results in a bandgap of 4.49 eV and 4.34 eV for MgS and MgS_2, respectively. Both MgS and MgS_2 exhibits indirect bandgaps. Previous theoretical studies employing hybrid functional also reported an indirect band gap in the range of 4.0 eV to 4.8 eV for MgS.[118, 119]

5.3.2   Localization of polaron

Polarons are the localized charge of an electron or hole along with the induced polarization of the surrounding lattice in the crystal (i.e., lattice distortion in the vicinity of localized charge). In this work, we attempted

|	Bandgap (eV)	
	MgS	MgS_2
HSE06	4.49	4.34
GW_0	4.52	4.33
G_0W_0	4.29	3.88

Table 5.1. Calculated bandgaps for MgS and MgS_2 with different levels of theory

to localize four types of polarons: single hole polaron (p^1), double hole polaron (p^{2+}), single electron polaron (p^{1-}), and double electron polaron (p^{2-}).

In MgS, we were only able to obtain p^{2+}. The sulfur atom in MgS has an oxidation state of -2. Removal of 2 electrons from the system results in a p^{2+} which changes the oxidation states of two sulfur atoms from -2 to -1. Thus the ions experience weaker electrostatic repulsion, resulting in the formation of a S-dimer. This can be seen in Figure 5.2a that a S dimer is formed. The original S$-$S interataomic distance of $3.65\,\text{Å}$ is shortened to $2.3\,\text{Å}$ in the presence of double-hole polaron. The double-hole polaron is localized only when the system is relaxed from a initial configuration in which one of the S-S bond is shortened. Without this initial distortion, it results in the delocalization of the polaron in the crystal. The delocalization energy (i.e., the difference in total energy between the structures with polaron delocalized and localized) for p^{2+} in MgS is calculated to be $0.21\,\text{eV}$. Previous study on MgO (which has a rocksalt structure similar to MgS) demonstrated that a single hole polaron could be localized on the Mg atom. [120] However, we could not localize the single hole polaron as well as the electron polarons in MgS.

For MgS_2, we could localize double-electron polaron and single-electron polaron. The addition of an electron leads to localization of the p^{1-} on the sulfur dimer without any initial structural distortion. The presence of p^{1-} increases the S$-$S bond distance to $2.57\,\text{Å}$ from $2.05\,\text{Å}$. Figure 5.2b shows the localization of p^{1-} on the S dimer. The p^{2-} formed by the addition of two electrons increases the S$-$S distance significantly to $3.15\,\text{Å}$. This is illustrated in Figure 5.2c. The formation of p^{2-} required a manual distortion of the initial structure. We observed that without this initial distortion, the two electrons were localize as two separate p^{1-} in

the crystal structure.

MgS single hole polaron   MgS$_2$ single electron polaron   MgS$_2$ double electron polaron
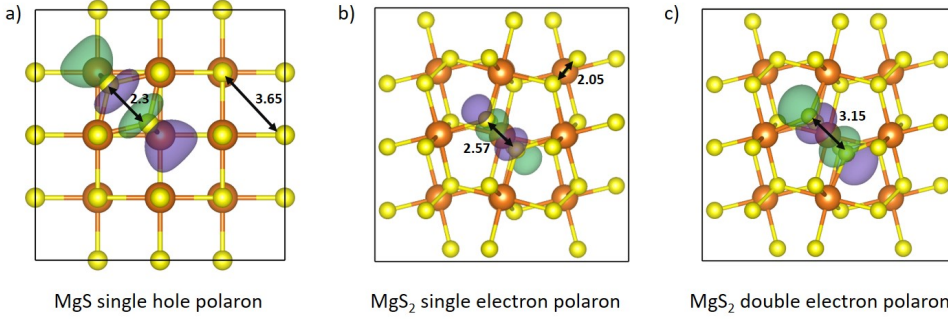
Figure 5.2. Frontier orbital wave function of a) Doubel hole polaron (p^{2+}) localized in MgS b) single electron polaron (p^{1-}) localized in MgS$_2$, and c) double electron polaron (p^{2-}) localized in MgS$_2$. The numbers in the figure shows the S-S distance in Å

5.3.3 Defect formation energy

The formation energy of defects in MgS and MgS$_2$ for different chemical potential is shown in Figure 5.3. The chemical potential varies with chemical environment of the system. i,e., the reservoir from which the chemical potential taken can be defined as Mg rich region (S poor region) or Mg poor region (S rich region). Based on OQMD database,[121] the phases that are in thermodynamic equilibrium with MgS at $0\,\mathrm{K}$ are Mg$_{149}$S, and MgS$_2$. While, the phases that are in thermodynamic equilibrium with MgS$_2$ are MgS and S. Thus, the limiting chemical potential value for calculating defects in MgS are defined by the Mg$_{149}$S$-$MgS region (Mg rich) and MgS$-$MgS$_2$ region (Mg poor). Similarly for MgS$_2$, the limiting chemical potential is defined by the MgS$-$MgS$_2$ (Mg rich) and MgS$_2$$-$S (Mg poor) regions.

A total of 69 charged defects including magnesium vacancies (Vac$_{\mathrm{Mg}}$), magnesium interstitial (Int$_{\mathrm{Mg}}$), sulfur vacancies (Vac$_{\mathrm{S}}$), sulfur interstitial (Int$_{\mathrm{S}}$), hole polarons and electron polarons were considered. The charge of the defects are given as superscript in their notation. The slope of each line corresponds to charge state of that defect. We investigated 3
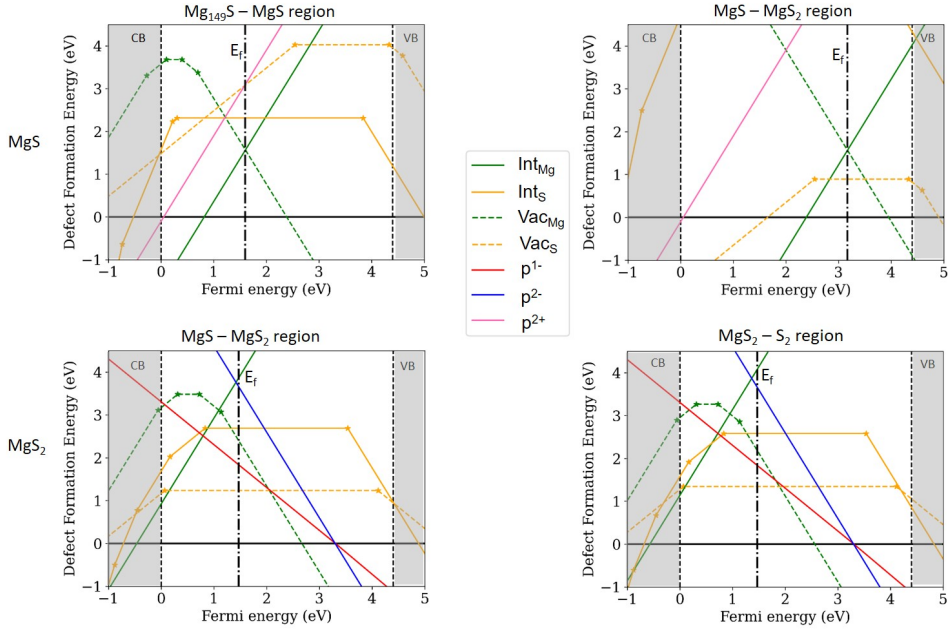
distinct interstitial positions for the Mg and S interstitial in MgS. However, the interstitial defect with low formation energies are only shown in Figure 5.3. The position of the equilibrium fermi level (E_f), which is indicated as vertical dashed line in Figure 5.3 is determined using the charge neutrality condition, $\sum c_i q_i = 0$. The defects with low formation energy at equilibrium fermi level is considered as the dominant defect. The concentrations of the prevalent defects is given in Table 5.2.

Figure 5.3a and Figure 5.3b illustrate the formation energies of the defects in MgS for $Mg_{149}S-MgS$ region and $MgS-MgS_2$ region, respectively. In both regions, Vac_{Mg}^{2-} and Int_{Mg}^{2+} are the most favorable charged defects and they exhibit low defect formation energies, result in a high defect concentration of $9.78\,cm^{-3}$ The equilibrium fermi level is located at the intersection of these two defects, since the opposite charges of these two defects cancel each other out, resulting in the charge neutrality condition. In $MgS-MgS_2$ region, the defect with lowest formation energy is Vac_S^0. However, since the defect is neutral, it does not contribute to charge transport. Puntambekar et al. reported that Vac_{Mg}^{2-} is the predominant defect in MgS, which agrees with our observation.[106]

The defect formation energies of the defects in MgS_2 for $MgS\text{-}MgS_2$ and MgS-MgS regions are shown in Figure 5.3c and Figure 5.3d. Both regions showcase analogous defect formation energy diagram with Vac_S^0 as the lowest formation energy defect. However, as stated previously, they have no effect on charge transport due to the neutral charge. The p^{1-} is the next dominant defect in MgS_2 with a defect concentration of $3.48 \times 10^{-9}\,cm^{-3}$. Vac_{Mg}^{2-} have a slightly greater defect formation energy, which results in a rather lower defect concentration of $6.65 \times 10^{-15}\,cm^{-3}$. The interstitial defects in MgS_2 exhibits very high formation energy.
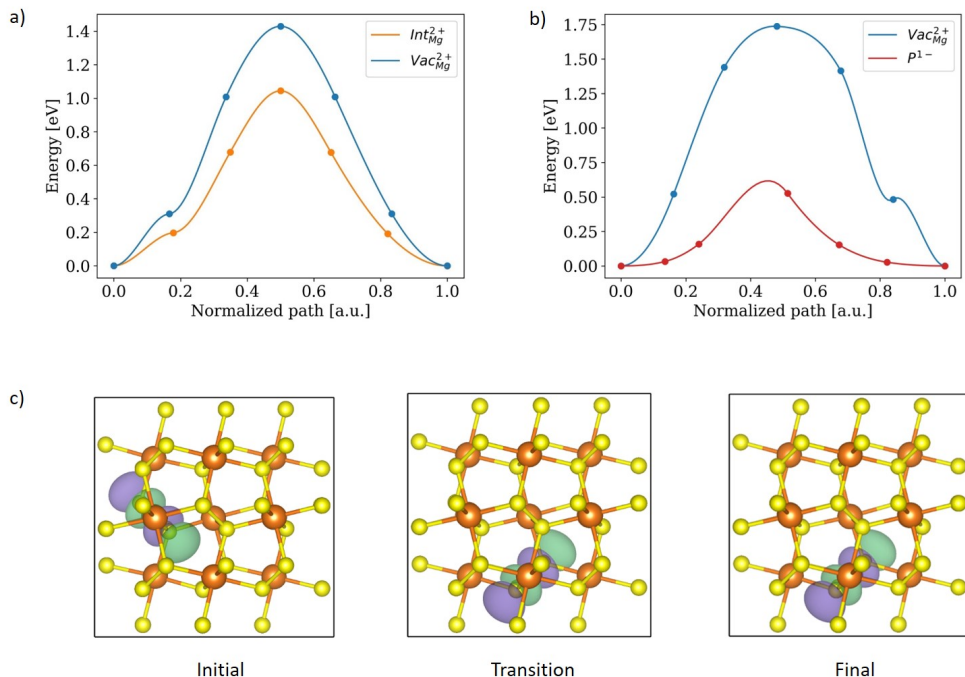
5.3.4   Mobility and conductivity

The energy barrier for the diffusion of most prevalent defects in MgS and MgS_2 were calculated using nudged elastic band method (NEB). Figure 5.4a depicts the minimum energy path (MEP) for the predominant defects in MgS. The calculated mobility and conductivity values are summarized in Table 5.2. Vac_{Mg}^{2-} exhibits very high migration barrier, which is consistent with experiment.[104]. Previous computational

Figure 5.3. The defect formation energy for MgS and MgS$_2$. The equilibrium Fermi energy is shown with the dashed dotted line.

study using PBE functional estimated a migration barrier of $0.9\,\text{eV}$ for the diffusion of $\text{Vac}_{\text{Mg}}^{2-}$.[107] The use of different functional could be the cause of variance in migration barrier compared to our study. The diffusion of $\text{Int}_{\text{Mg}}^{2+}$ is also characterized by a high diffusion barrier of $1\,\text{eV}$. The diffusion barrier of these defects are higher than the maximum tolerable migration barrier for cathodes in RMB, which is $\sim 0.9\,\text{eV}$. [107] Despite having high defect concentrations, the low mobility of the $\text{Int}_{\text{Mg}}^{2+}$ and $\text{Vac}_{\text{Mg}}^{2-}$ results in poor conductivity.

The MEP for the dominant defects in MgS$_2$ is shown in Figure 5.4b. Analogous to MgS, the $\text{Vac}_{\text{Mg}}^{2-}$ migration barrier in MgS$_2$ is also very high. The single electron polaron (p^{1-}) exhibit low diffusion barrier. The activation energy for the diffusion of p^{1-} is $0.53\,\text{eV}$. Figure 5.4c shows the initial, intermediate, and final states of the p^{1-} migration. The relatively low energy barrier of p^{1-} leads to a decent mobility. However, the less concentration of these defect results in negligible conductivity. Owing to their low diffusion barrier, the maximum diffusion length for p^{1-} is

Figure 5.4. The energy barrier for the prevalent defects in a) MgS, and b) MgS$_2$.c) Frontier orbital wave function of initial, transition, and final images of p^{1-} in MgS$_2$

calculated to be 3.1×10^3 nm for a discharge rate of 1C. This implies that the mobility of p^{1-} is sufficient enough to traverse through the cathode. Therefore, a potential strategy to improve the conductivity in MgS$_2$ is to enhance the concentration of p^{1-}.
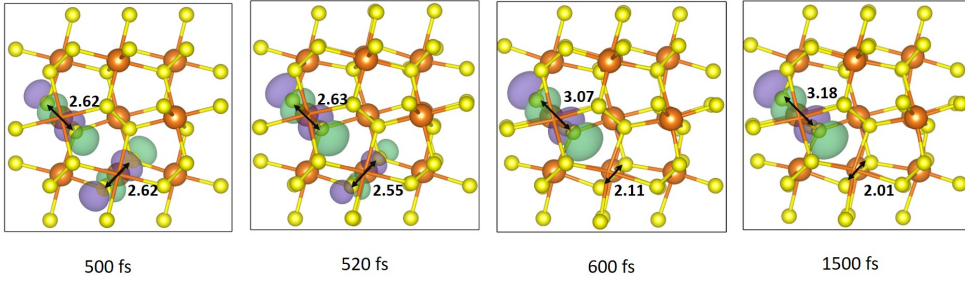
5.3.5 Molecular Dynamics

So far, we have analysed the transport mechanism based on the intrinsic defects formed at equilibrium. However, during the practical battery operation the scenario is different, being the cathode material out of equilibrium. During the charging of battery, electrons move from the external circuit to the cathode. Simultaneously, Mg ions from the electrolyte join the cathode. We employed different AIMD setups to comprehend the

System	Defects	Defect concentration [cm^{-3}]	Energy barrier [eV]	Mobility cm^2/(Vs)	Conductivity [S cm^{-1}]
MgS	Vac$_{Mg}^{2-}$	9.78	1.42	1.3×10^{-24}	2.7×10^{-23}
	Int$_{Mg}^{2+}$	9.78	1.01	8.3×10^{-18}	1.3×10^{-16}
MgS$_2$	Vac$_{Mg}^{2-}$	6.6×10^{-15}	1.7	1.1×10^{-29}	1.5×10^{-43}
	p^{1-}	3.4×10^{-9}	0.53	1.0×10^{-9}	3.6×10^{-18}

Table 5.2. Defect concentration, energy barrier, mobility and conductivity for the most prevalent defects in MgS and MgS$_2$.

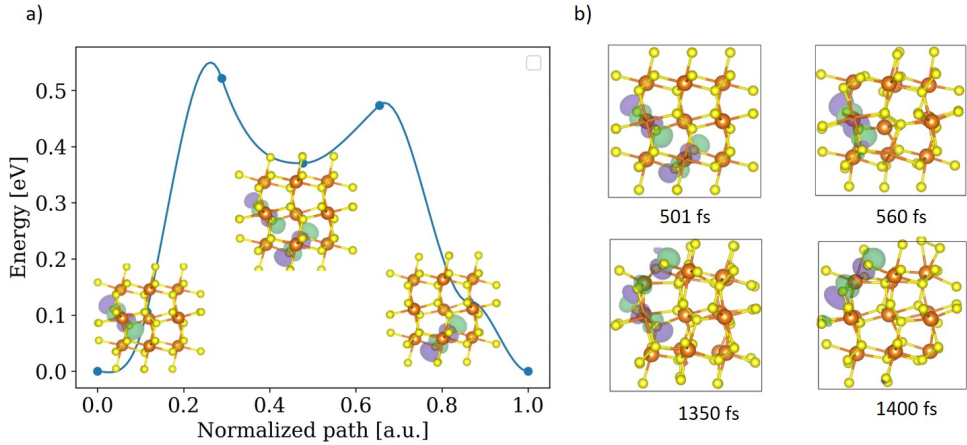system's dynamics in such a scenario.

Figure 5.5. Snapshot from MD of electron polarons in bulk MgS$_2$

The Mg^{2+} ion from the electrolyte need two electrons from external circuit to compensate the charge. Our initial AIMD setup aimed to determine whether electrons entering from the external circuit prefer to exist as p^{1-}s or as a p^{2-}. The system was initialized with two single-electron polarons localized in the bulk crystal structure. The size of the bulk supercell is $2 \times 2 \times 2$ of the conventional unit cell with 96 atoms. The snapshot from the AIMD simulation after equilibration is shown in Figure 5.5. During the equilibration, the S-dimers in which the polarons were localized kept fixed. From the Figure 5.5, it is clear that initially the electrons exist as separated p^{1-}. Then in the subsequent steps they merge to form p^{2-}. Consequently, the S−S distance of one S-S dimer shorten while the S−S distance of the other dimer increases. We did not observed any further diffusion of p^{2-}.

To evaluate the diffusion of p^{2-}, we performed a NEB calculation. We observed that the migration of p^{2-} from one site to the equivalent site happens via an intermediate stage at which the p^{2-} split into two different p^{1-}. It can be clearly seen in Figure 5.6a that p^{2-} is localized in the initial and final images, while its split into two distinct p^{1-} in the intermediate image. The energy barrier for the formation of two p^{1-} from p^{2-} is $0.52\,\text{eV}$. Probably due to this high barrier that the diffusion of p^{2-} did not observed in our MD simulation. Therefore, we performed the MD simulation at $1000\,\text{K}$ with same setup used for the previous MD simulation. The snapshots from the MD simulation is shown in Figure 5.6b. During the initial steps of MD, the two p^{1-} combine to form p^{2-} as analogus to previous MD simulation. After then we observe the diffusion p^{2-} via two p^{1-}, which is consistent with our observation in NEB calculation.
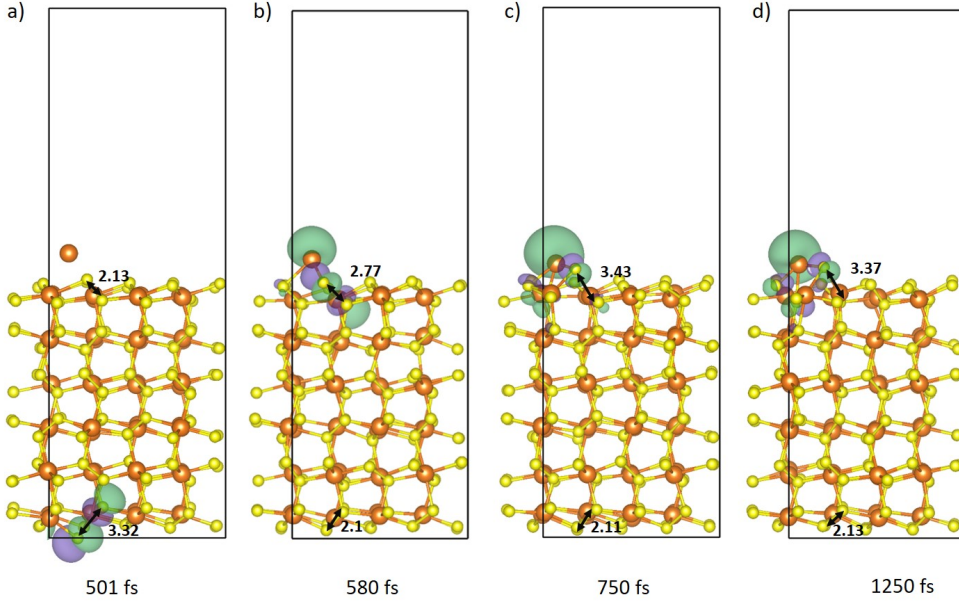
From these MD simulations, we anticipate that the electrons approaching the cathode from the external circuit will readily combine and form p^{2-}. For subsequent simulations, we therefore assumed the electrons entering from the external circuit to be p^{2-}.

Figure 5.6. a) Minimum energy path for p^{2-}. b) Snapshots from MD simulation of bulk at $1000\,\text{K}$

The second setup is to study the magnesiation in MgS_2 surface. We used a slab structure of (001) surface of MgS_2 with a vacuum of $15\,\text{Å}$ and slab thickness of $18\,\text{Å}$. To localize the polaron, the system is initiated
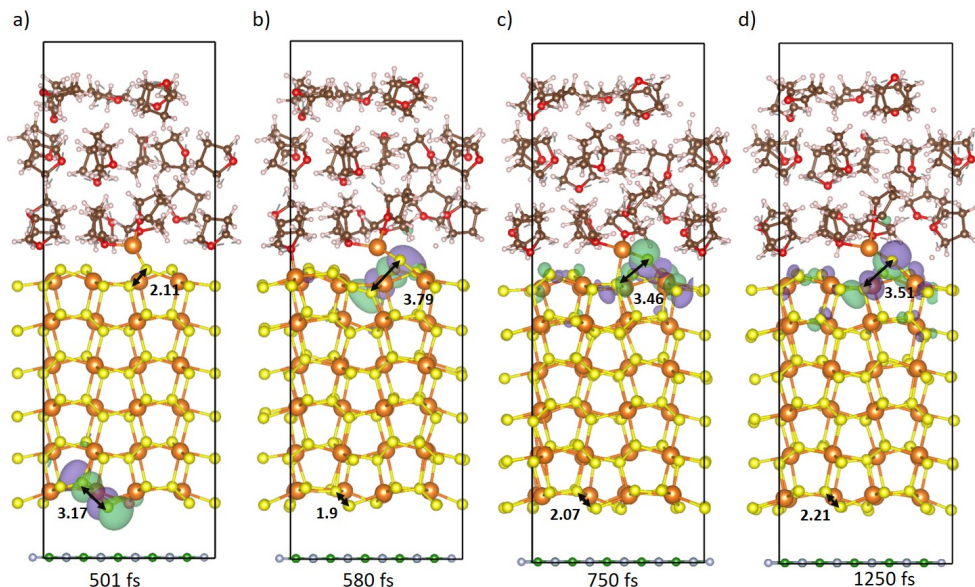
in such a way that one of the $S-S$ bonds at the bottom of the slab is broken. A Mg atom is placed on top of the slab to investigate the effect of magnesiation at the electrode surface. To compensate for the dipole moment from the Mg atom, dipole correction was applied in the direction of the surface.

Figure 5.7. Snapshot from MD at (001) surface of MgS_2

Figure 5.7 depicts snapshots from the MD run. It can be seen that, the p^{2-} is localized at the bottom of the slab in the beginning. The charge is transferred to the surface on subsequent MD steps when the Mg^{2+} begins to interact with the cathode. This is also reflected on the $S-S$ distance of the S dimers in which the charge is localized. The $S-S$ distance of the S dimer at which the polaron localized at the beginning of the simulation has been reduced from $3.6\,\text{Å}$ to $2.1\,\text{Å}$. In contrast, the interaction with Mg^{2+} increases the S-S distance of the S-dimer at the surface to $3.6\,\text{Å}$ from $3.6\,\text{Å}$. This implies the formation of MgS at the surface. During the MD run, no charge transport path was observed. When Mg^{2+} interacts at the surface, the localized charge from the bottom of the slab abruptly of shifts to the surface. Probably, electron tunneling

would have occurred from the bottom of the slab to the surface. Typically, tunneling occurs in materials with a thickness of less than $3\,\text{nm}$.[122] However, it is not feasible to study such a big system with current setup. In a system large enough to prevent tunneling, we could observe the transport path for the electron.

Figure 5.8. Snapshot from MD at 001 surface of MgS_2 with THF electrolyte

The third AIMD setup was designed to investigate the role of electrolytes in the magnesiation of MgS_2. The vacuum of the slab structure was filled with THF molecules, which are the commonly used electrolyte solvent in magnesium batteries. Using the GROMACS package,[123] 18 THF molecules were added to match the empirical density of $0.88\,\text{g}\,\text{cm}^{-3}$. [124] A bottom layer of wide gap semiconductor boron nitride (BN) was employed to prevent charge leakage from the slab's bottom to the electrolyte. Following the initial conjugate gradient relaxation, the electrolyte was relaxed at $350\,\text{K}$ for $0.5\,\text{ps}$ keeping the crystalline part frozen. Then, except for the BN, the crystalline component was unfrozen and relaxed for another $1\,\text{ps}$ to allow for cathode - electrolyte interaction. Figure 5.8 shows the snapshot from MD run. The observation is similar to what we saw in the previous MD simulation without the electrolyte. The

electrolyte seemed to have no direct effect on the magnesiation process, according to our MD simulation.

5.4   Conclusion

Elucidating the charge transport mechanism in MgS and MgS$_2$ is very essential in developing efficient RMBs. We performed a theoretical investigation of charge transport in these materials, evaluating the contribution of several defects to the conductivity in the material. In MgS, we identified $\text{Vac}_{\text{Mg}}^{2-}$ and $\text{Int}_{\text{Mg}}^{2+}$ as the prevalent defects. These defects show a relatively high concentration in the material. However, due to their poor mobility, the contribution of these defects to the conductivity of material is negligible. We identified that p^{1-} and $\text{Vac}_{\text{Mg}}^{2-}$ are the prevalent defects in MgS$_2$. The concentration of these defects appears to be quite high. Although the concentration of p^{1-} is low, their mobility is sufficient to allow them to traverse the MgS$_2$ deposit under practical battery conditions. Consequently, the strategy to enhance the conductivity in MgS$_2$ is to increase the concentration of p^{1-}. We also performed ab-initio molecular dynamics to understand the charge transport in non-equilibrium conditions. Our results indicate that two p^{1-} in MgS$_2$ prefer to combine and form a p^{2-}.

5.5   Outlook

The dominant defects in MgS identified in the present study have low mobility. Hence, we were not able to identify any charge carriers that could potentially improve the conductivity of MgS. A previous theoretical study on MgO, which has a similar crystal structure to MgS, reported that a p^{1+} is the dominant defect in MgO with excellent mobility. In the present work, we were not able to localize a p^{1+} in MgS. If the p^{1+} exist in MgS, they can be potential charge carrier in MgS. Thus, it is desirable to have a detailed investigation into the possibility of p^{1+} formation in MgS.
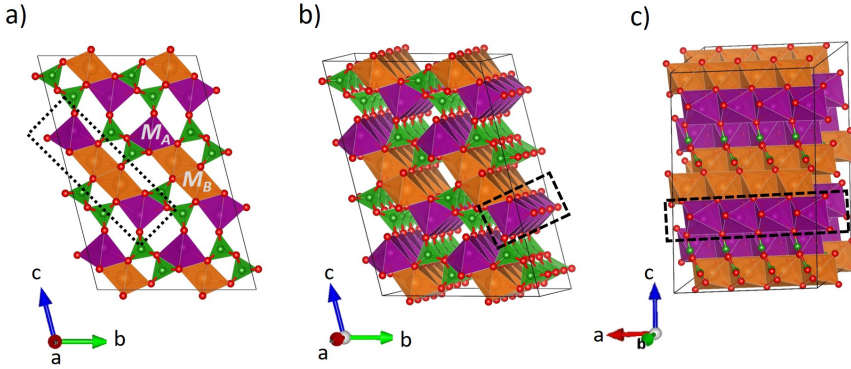
Disorder in pyroborate cathode

6.1   Introduction

In the search for novel cathode materials for rechargeable magnesium batteries (RMBs), polyanionic materials that consist of a metal cation (M) and a polyanionic group (XO, where X=B, S, P, etc.) are promising contenders. The polyanionic type cathodes exhibit high redox potential due to the "inductive effect", which arises from the difference in electronegativity between the strong X-O bond and the weak M-O bond.[125] In addition, the strong covalent bond between X and O provides additional stability to the crystal structure, thereby enhancing the safety of the materials and making them ideal for rechargeable battery applications.[126]

The borate anion is the lightest among the common polyanionic groups; as a result, it can provide higher specific capacity than other polyanions. Several studies have demonstrated the ability of borate-based materials as high-capacity cathodes for lithium-ion batteries. Although borate-based electrolytes have been extensively studied for RMBs, their potential as a cathode in RMBs has not been fully explored. Bo et al. investigated borate compounds such as $MgVBO_4$ and $MgFeB_2O_5$ as cathodes for RMBs and discovered that Mg is mobile in $MgFeB_2O_5$ but not in $MgVBO_4$.[127] A later study on disordered pyroborate $MgMnB_2O_5$ shows reversible Mg^2+ intercalation is possible in this material.[128] However, the the kinetics of Mg ion in this material is not fully explored.

The crystal structure of the pyroborate $MgMnB_2O_5$ is reported to be triclinic.[129] The polyanionic structure of $MgMnB_2O_5$ is made up of B_2O_5 units, which consist of two corner sharing BO_3 triangles. These

B_2O_5 units link the ribbon-like frameworks consisting of four parallel chains of edge-sharing MO_6 (in this case, M can be either Mg or Mn) octahedra (Figure 6.1a). Each parallel chain in the quadruplet ribbon extend in the a-direction (Figure 6.1b & c). These quadruplet ribbons have two crystallographically distinct sites, M_A and M_B, for the M cations. The outer two octahedral sites in the ribbon correspond to M_A, while the central two octahedral chains correspond to M_B. Since both sites are symmetrically distinct, this can lead to disorder in material as Mg and Mn can occupy either M_A and M_A sites. Also the mobility of Mg is strongly dependent on the site at which they are occupied as the local environment is different for both sites.

Figure 6.1. Crystal structure of $MgMnB_2O_5$ structure shown in different directions. The dotted lines shows the quadruplet ribbon and the dashed line shows the infinite chain of a cation in the quadruplet ribbon. For illustration purpose, the M_A site with is shown with occupation of Mn (purple octahedra) and M_B site is shown with occupation of Mg (orange octahedra). Boron atoms are shown in green and oxygen atoms are shown in red.

Therefore, understanding on the disorder in the material is crucial in studying the ion kinetics. It has been demonstrated that the cluster expansion (CE) method coupled with density functional theory (DFT) calculations are effective tools for predicting the disorder in a material.[72, 73] The current study focus on assessing the disorder in the material at various magnesiation levels using Monte Carlo simulations based on CE method.

6.2   Methodology

Spin-polarized DFT calculations were employed to calculate the total energies, which are then used to train the CE models. All DFT calculations were performed using the Vienna Ab initio Simulation Package (VASP) [54, 55] using a plane-wave basis set with cut-off energy of 520 eV. The exchange and correlation effects are approximated using Perdew-Burke-Ernzerhof revised for solids (PBEsol)[130] functional with a correction of U=3.9 eV on Mn-d orbitals, as recommended by the materials project to account for the self-interaction error.[86] The projector augmented wave (PAW) method was used to account for the core-valence interactions [56]. The Brillioun zone is sampled using the Monkhorst-Pack grid with a k-point density of 4 points per Å^{-1}. The atomic positions and cells were relaxed until the forces of each atom converged to within $1 \times 10^{-2}\,\text{eV}\,\text{Å}^{-1}$. The threshold for the convergence of total energy is set to 1×10^{-6} eV.

The CLEASE software package is adopted to generate various atomic configurations for DFT calculations and train the CE model. The structures were constructed in such a way that the M_A and M_B sites can be occupied by either Mg, Mn or a vacancy. The vacancy represent the removal of Mg from the structure. This allows to generate structures with various levels of disorder and different Mg concentration. We generated 367 atomic structures with different magnesium concentrations to train the CE model. The amount of magnesium removed in this study is restricted to 25 %, as a prior experimental investigation reported a demagnesiation of less than 25 % for $MgMnB_2O_5$ when used as the cathode in a magnesium battery.

The energies from the DFT calculations were used to construct the CE model by fitting effective cluster interactions (ECIs). The maximum cut-off radii for the 2-body, 3-body, and 4-body clusters were set to 6, 4 and 4 Å respectively, for the construction of the CE model. The ℓ_2 regularization scheme is employed to account for the overfitting. The predictability of the model is evaluated using the leave-one-out cross-validation (LOOCV) score.

After obtaining good CE model, canonical Monte Carlo (MC) simulations were performed to evaluate the disorder at different magnesium concentrations. Using MC simulated annealing, the disorder at various

magnesium concentrations and temperatures were assessed. The starting temperature for simulated annealing was set to 1×10^{10} K and gradually decreased to 1 K. A supercell of 12×6×4 with 5184 atoms were used for the simulated annealing.

The disorder in this material is due to the flexibility of Mg and Mn to occupy either M_A and M_B sites. As a result, the degree of disorder in this material can be defined by a cation's occupation of any of the M_A and M_B sites. For the sake of consistency, throughout this study the degree of disorder in this material is evaluated based on the occupation of Mn on M_B sites, and is calculated as

$$\text{Degree of disorder} = \frac{\text{Number of Mn on} M_B \text{ sites}}{\text{Total number of } M_B \text{ sites}} \qquad (6.1)$$

6.3   Results and discussion

As a first step in evaluating the disorder in material, we construct a CE model with reasonable accuracy. The generated CE model has a LOOCV score of 2.19 meV/atom. The developed CE model was then couple with Monte Carlo simulations to predict the low energy structures and the disorder in the material at different level of magnesiation. Figure 6.2 depicts the predicted disorder at different temperatures for various levels of magnesiation. The predicted disorder for the fully magnesiated structure at room temperature matches with the experimental reported disorder of 0.35. Figure 6.2 shows that the disorder tends to increase with the amount of demagnesiation. This indicates that the removal of Mg from the material facilitate the redistribution of cations in the structure. However, for such a redistribution to happen, it is required that both Mg and Mn should have mobility in the structure.

The lowest energy structures obtained from the MC annealing for fully magnesiation, 0.13 demagnesiation, and 0.25 demagnesiation is shown in Figure 6.3b, 6.3c, 6.3d, respectively. The ordered structure, which is used as the starting point for MC annealing is shown in Figure 6.3a. The MC annealing study reveals that the ground state structure of MgMnB$_2$O$_5$ exhibits a specific pattern, despite of having a disorder of 0.38. The cation chain in the quadruplet ribbon shows alternate occupa-
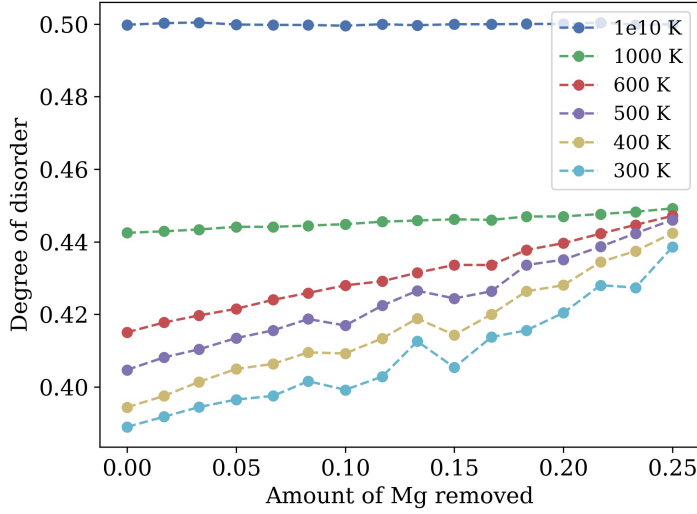
Figure 6.2. Occupation of Mn at M_B sites for different level of magnesiation

tion of Mg and Mn (Figure 6.3b), compared to the single type of cation occupancy in fully ordered structure (Figure 6.3a). This kind of pattern could develop a percolation path for the Mg diffusion in these structures. However, further studies are required to fully understand the specific arrangement of the structure when it is fully magnesiated. We observed that the specific pattern is lost upon demagnesiation. It is interesting to note that it is preferred to remove magnesium from a site between two Mn-occupied sites (Figure 6.3c & d). This has been observed for all levels of magnesiation.

The structural insights in to this disordered material can serve as the starting point for studying the Mg ion kinetics in this material. Due to the cation disorder, it is not feasible to use conventional approaches, such as the nudged elastic band (NEB) method to investigate the ion kinetics in this material. In this context, neural network based machine learning potentials is a realistic approach to study the several possible transformation pathways in these material. Further work in this aspect is underway.
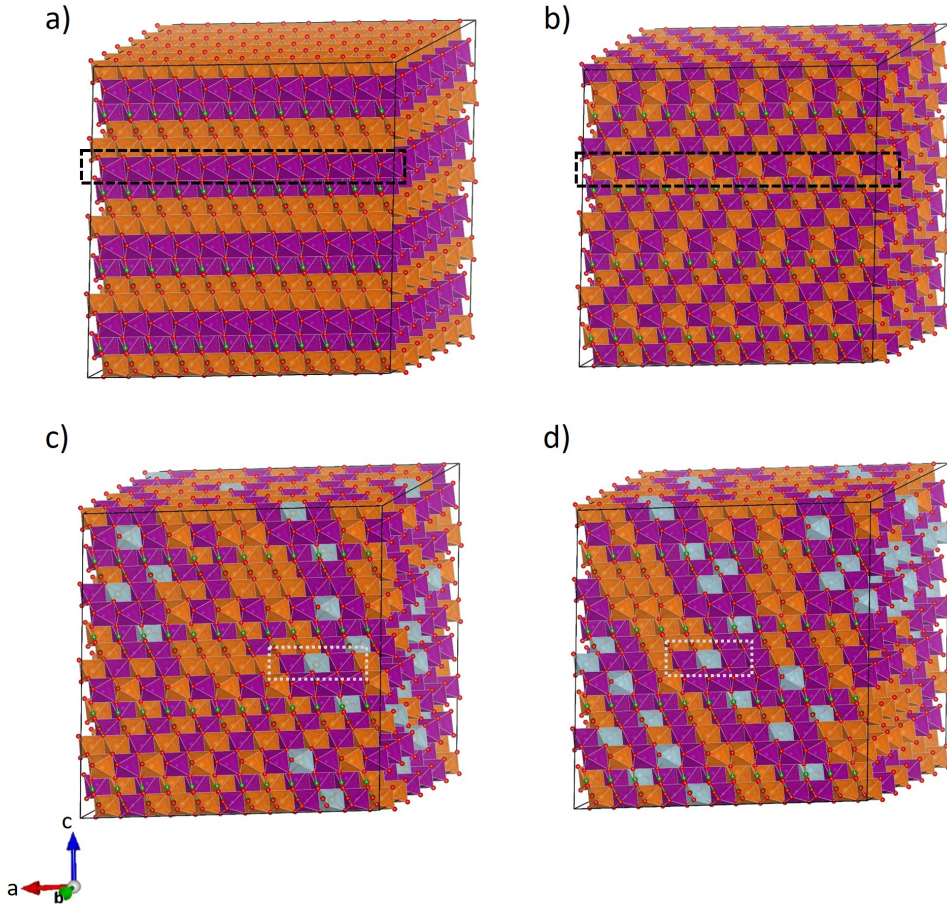
Figure 6.3. a) Starting configuration for MC simulation. Lowest energy structures from MC annealing for b) fully magnesiation c) 0.13 magnesiation and d) 0.25 demagnesiation. Orange octahedra represents Mg sites, purple octahedra Mn sites, and light blue octahedra represents vacancy

6.4   Conclusion

We employed DFT trained CE model to evaluate the disorder in pyroborate $MgMnB_2O_5$ cathode for RMBs. The study shows that the disorder in the material increase with demagnesiation. For the fully disorder structure, our predicted disorder agrees well with the previous experi-

ment studies. The MC annealing simulation reveals that the ground state structure of fully magnesiated structure have a specific pattern for the cation occupation. Further studies are required to understand the kinetics in the material.

6.5   Outlook

In this study, we limited the amount of demagnesiation to 25 %, given that the experimental study on this material in magnesium batteries only shows 25 % demagnesiation.[128] However, with a proper electrolyte, it will be possible to fully demagnesiate the structure. Therefore, a study with fully demagnesiation is desirable.

   Preliminary studies are carried out along this line. However, it is observed that including the fully demagnesiated structure affects the predictability of the CE model. We found that some of the DFT calculations did not yield the lowest energy structures, unless the difference between spin-up and spin-down electrons is fixed (NUPDOWN in vasp). However, for some structures, this initialization resulted in higher energy than previously calculated energy without initialization. The attempt to use the hybrid functional HSE instead of PBE+U functional also did not improve the predictability of the CE model. Therefore, exploring the full phase space upto fully demagnesiated structure is shown to be a difficult task. Hence, in the interest of time, we limit the current study to 25 % demagnesiation.

CHAPTER 7

Summary

The thesis presented the outcomes of four projects that aimed to understand and design suitable electrode materials for rechargeable magnesium batteries (RMBs). The main findings from the four projects are summarized as follows.

The first project performed a DFT screening of 34 dopants that are reported to improve magnesium ductility to investigate whether their alloying with magnesium is beneficial for RMB applications. As a preliminary step, we checked the potential of these dopants to promote stacking fault defects in Mg, considering that stacking fault defects improve the ductility of magnesium. Subsequent analysis based on the alloying stability of dopants narrows down the search to 20 dopants. Finally, we evaluated the propensity of these dopants to migrate to the surface and excluded 8 dopants that tend to migrate to the surface as they may have an impact on electrochemical properties. The systematic screening identified 12 beneficial doping elements for the magnesium anode. These include Al, Dy, Er, Gd, Ho, Lu, Nd, Sc, Sm, Tb, Tm, and Y. The commercial alloy WE43 has two of the dopants identified in this study, Nd and Y, making it a potential anode for a magnesium battery.

In the second project, we explored the phase space of the Mg-Sn system to gain a deeper insight into the stability of the phases formed during the battery operation. Sn exists in two allotropic forms, α-Sn (fcc) and β-Sn (bct), and on complete magnesiation it becomes Mg_2Sn (fcc). In order to analyze the phase stability of fcc and bct structures, two CE models are constructed and compared within the same framework. Phase stability analysis confirmed that α-Sn, β-Sn and Mg_2Sn are the only phases present in this system. The observations from the obtained convex hull plot and voltage profile agree well with the experiment. The study discussed the thermodynamic feasibility of three routes for the

transformation from Mg_2Sn to Sn: $Mg_2Sn \rightarrow \alpha$-Sn $\rightarrow \beta$-Sn, $Mg_2Sn \rightarrow$ β-Sn, and $Mg_2Sn \rightarrow$ amorphous phase $\rightarrow \beta$-Sn.

The third project investigated the charge transport mechanism in MgS and MgS_2, which are the discharge end products on the MgS cathode. The study evaluated the contribution of several defects to the conductivity in these materials. The prevalent defects in MgS are doubly negative Mg vacancy and doubly positive Mg interstitial. Despite having a high defect concentration, the poor mobility of these defects results in very low conductivity. On the other hand, the two dominant defects in MgS_2, doubly negative Mg vacancy and single electron polaron, show a very low defect concentration. The single electron polaron exhibited decent mobility in MgS despite the low concentration. This implies that increasing the concentration of electron polaron in MgS can lead to perceptible conductivity. Furthermore, a molecular dynamics study on evaluating the charge transport in non-equilibrium conditions revealed that two single electron polarons preferred to combine and form a double electron polaron in MgS_2 during practical battery operation.

The fourth and final project provided insight into the structural properties of disordered pyroborate cathodes. In this study, a cluster expansion model was employed to predict the disorder at various temperatures for different levels of magnesiation. The predicted disorder for the fully magnesiated structure at room temperature agrees well with the experiment. Examining the lowest energy structures obtained from CE based Monte Carlo annealing revealed that when fully magnesiated, the cathode material exhibits a specific pattern in the occupation of cations.

Bibliography

[1] Xiayue Fan, Bin Liu, Jie Liu, Jia Ding, Xiaopeng Han, Yida Deng, Xiaojun Lv, Ying Xie, Bing Chen, Wenbin Hu, et al. Battery technologies for grid-level large-scale electrical energy storage. *Transactions of Tianjin University*, 26(2):92–103, 2020.

[2] Hussein Ibrahim, Adrian Ilinca, and Jean Perron. Energy storage systems—characteristics and comparisons. *Renewable and sustainable energy reviews*, 12(5):1221–1250, 2008.

[3] Reed T Doucette and Malcolm D McCulloch. A comparison of high-speed flywheels, batteries, and ultracapacitors on the bases of cost and fuel economy as the energy storage system in a fuel cell based hybrid electric vehicle. *Journal of Power Sources*, 196(3): 1163–1170, 2011.

[4] China Energy Storage. Cnesa white papers. URL `http://en.cnesa.org/white-paper-access-multyear`.

[5] Marco Piccolino. The bicentennial of the voltaic battery (1800–2000): the artificial electric organ. *Trends in neurosciences*, 23(4): 147–151, 2000.

[6] Rana Mohtadi, Masaki Matsui, Timothy S. Arthur, and Son-Jong Hwang. Magnesium borohydride: From hydrogen storage to magnesium battery. *Angewandte Chemie*, 124(39):9918–9921, August 2012.

[7] Ronald Dell and David Anthony James Rand. *Understanding batteries*. Royal society of chemistry, 2001.

[8] Paul Breeze. Chapter 4 - large-scale batteries. In Paul Breeze, editor, *Power System Energy Storage Technologies*, pages 33–45. Academic Press, 2018. ISBN 978-0-12-812902-9.

[9] M Stanley Whittingham. Electrical energy storage and intercalation chemistry. *Science*, 192(4244):1126–1127, 1976.

[10] KJPC Mizushima, PC Jones, PJ Wiseman, and John B Goodenough. Lixcoo2 (0< x<-1): A new cathode material for batteries of high energy density. *Materials Research Bulletin*, 15(6):783–789, 1980.

[11] Akira Yoshino. The birth of the lithium-ion battery. *Angewandte Chemie International Edition*, 51(24):5798–5800, 2012.

[12] Rana Mohtadi and Fuminori Mizuno. Magnesium batteries: Current state of the art, issues and future perspectives. *Beilstein Journal of Nanotechnology*, 5:1291–1311, August 2014.

[13] Pieremanuele Canepa, Gopalakrishnan Sai Gautam, Daniel C Hannah, Rahul Malik, Miao Liu, Kevin G Gallagher, Kristin A Persson, and Gerbrand Ceder. Odyssey of multivalent cathode materials: open questions and future challenges. *Chemical reviews*, 117(5): 4287–4341, 2017.

[14] Nitin Muralidharan, Ethan C Self, Marm Dixit, Zhijia Du, Rachid Essehli, Ruhul Amin, Jagjit Nanda, and Ilias Belharouak. Next-generation cobalt-free cathodes–a prospective solution to the battery industry's cobalt problem. *Advanced Energy Materials*, 12(9): 2103050, 2022.

[15] Federico Bella, Stefano De Luca, Lucia Fagiolari, Daniele Versaci, Julia Amici, Carlotta Francia, and Silvia Bodoardo. An overview on anodes for magnesium batteries: challenges towards a promising storage solution for renewables. *Nanomaterials*, 11(3):810, 2021.

[16] Doron Aurbach, Z Lu, Alex Schechter, Yossef Gofer, H Gizbar, R Turgeman, Y Cohen, Mordechay Moshkovich, and El Levi. Prototype systems for rechargeable magnesium batteries. *Nature*, 407 (6805):724–727, 2000.

[17] Jiazheng Niu, Zhonghua Zhang, and Doron Aurbach. Alloy anode materials for rechargeable mg ion batteries. *Advanced Energy Materials*, 10(23):2000697, 2020.

[18] E Peled and H Straze. The kinetics of the magnesium electrode in thionyl chloride solutions. *Journal of The Electrochemical Society*, 124(7):1030, 1977.

[19] Doron Aurbach, Yossef Gofer, Alex Schechter, O Chusid, H Gizbar, Y Cohen, M Moshkovich, and R Turgeman. A comparison between the electrochemical behavior of reversible magnesium and lithium electrodes. *Journal of power sources*, 97:269–273, 2001.

[20] Thomas D Gregory, Ronald J Hoffman, and Richard C Winterton. Nonaqueous electrochemistry of magnesium: applications to energy storage. *Journal of The Electrochemical Society*, 137(3):775, 1990.

[21] Christopher J. Barile, Elizabeth C. Barile, Kevin R. Zavadil, Ralph G. Nuzzo, and Andrew A. Gewirth. Electrolytic conditioning of a magnesium aluminum chloride complex for reversible magnesium deposition. *The Journal of Physical Chemistry C*, 118(48): 27623–27630, November 2014.

[22] Oren Mizrahi, Nir Amir, Elad Pollak, Orit Chusid, Vered Marks, Hugo Gottlieb, Liraz Larush, Ella Zinigrad, and Doron Aurbach. Electrolyte solutions with a wide electrochemical window for rechargeable magnesium batteries. *Journal of The Electrochemical Society*, 155(2):A103, 2008.

[23] Toshihiko Mandai and Hidetoshi Somekawa. Metallurgical approach to enhance the electrochemical activity of magnesium anodes for magnesium rechargeable batteries. *Chem. Commun.*, 2020. ISSN 1359-7345, 1364-548X.

[24] Timothy S. Arthur, Nikhilendra Singh, and Masaki Matsui. Electrodeposited bi, sb and bi1-xSbx alloys as anodes for mg-ion batteries. *Electrochemistry Communications*, 16(1):103–106, March 2012.

[25] Nikhilendra Singh, Timothy S Arthur, Chen Ling, Masaki Matsui, and Fuminori Mizuno. A high energy-density tin anode for rechargeable magnesium-ion batteries. *Chemical communications*, 49(2):149–151, 2013.

[26] Fabrizio Murgia, Ephrem Terefe Weldekidan, Lorenzo Stievano, Laure Monconduit, and Romain Berthelot. First investigation of indium-based electrode in mg battery. *Electrochemistry Communications*, 60:56–59, 2015.

[27] Kalani Periyapperuma, Tuan T Tran, MI Purcell, and MN Obrovac. The reversible magnesiation of pb. *Electrochimica Acta*, 165:162–165, 2015.

[28] S. Sandlöbes, M. Friák, S. Korte-Kerzel, Z. Pei, J. Neugebauer, and D. Raabe. A rare-earth free magnesium alloy with improved intrinsic ductility. *Scientific Reports*, 7(1), September 2017.

[29] S. Sandlöbes, M. Friák, S. Zaefferer, A. Dick, S. Yi, D. Letzig, Z. Pei, L.-F. Zhu, J. Neugebauer, and D. Raabe. The relation between ductility and stacking fault energies in mg and mg–y alloys. *Acta Materialia*, 60(6-7):3011–3021, April 2012.

[30] E Levi, Y Gofer, and D Aurbach. On the way to rechargeable mg batteries: the challenge of new cathode materials. *Chemistry of Materials*, 22(3):860–868, 2010.

[31] Gregory Gershinsky, Hyun Deog Yoo, Yosef Gofer, and Doron Aurbach. Electrochemical and spectroscopic analysis of mg2+ intercalation into thin film electrodes of layered oxides: V2o5 and moo3. *Langmuir*, 29(34):10964–10972, 2013.

[32] Kwan Woo Nam, Sangryun Kim, Soyeon Lee, Michael Salama, Ivgeni Shterenberg, Yossi Gofer, Joo-Seong Kim, Eunjeong Yang, Chan Sun Park, Ju-Sik Kim, et al. The high performance of crystal water containing manganese birnessite cathodes for magnesium batteries. *Nano Letters*, 15(6):4071–4079, 2015.

[33] Yuki Orikasa, Titus Masese, Yukinori Koyama, Takuya Mori, Masashi Hattori, Kentaro Yamamoto, Tetsuya Okado, Zhen-Dong

Huang, Taketoshi Minato, Cédric Tassel, et al. High energy density rechargeable magnesium battery using earth-abundant and non-toxic elements. *Scientific reports*, 4(1):1–6, 2014.

[34] Dan-Thien Nguyen, Raymond Horia, Alex Yong Sheng Eng, Seung-Wan Song, and Zhi Wei Seh. Material design strategies to improve the performance of rechargeable magnesium–sulfur batteries. *Materials Horizons*, 8(3):830–853, 2021.

[35] JN Reimers and JR Dahn. Application of ab initio methods for calculations of voltage as a function of composition in electrochemical cells. *Physical Review B*, 47(6):2995, 1993.

[36] MK Aydinol, AF Kohan, Gerbrand Ceder, Kang Cho, and JJPRB Joannopoulos. Ab initio study of lithium intercalation in metal oxides and metal dichalcogenides. *Physical Review B*, 56(3):1354, 1997.

[37] Michael M Thackeray, Christopher Wolverton, and Eric D Isaacs. Electrical energy storage for transportation—approaching the limits of, and going beyond, lithium-ion batteries. *Energy & Environmental Science*, 5(7):7854–7863, 2012.

[38] Felix T Bölle, Nicolai R Mathiesen, Alexander J Nielsen, Tejs Vegge, Juan Maria Garcia-Lastra, and Ivano E Castelli. Autonomous discovery of materials for intercalation electrodes. *Batteries & Supercaps*, 3(6):488–498, 2020.

[39] Pierre Hohenberg and Walter Kohn. Inhomogeneous electron gas. *Physical Review*, 136(3B):B864, 1964.

[40] Walter Kohn and Lu Jeu Sham. Self-consistent equations including exchange and correlation effects. *Physical review*, 140(4A):A1133, 1965.

[41] John P. Perdew, Kieron Burke, and Matthias Ernzerhof. Generalized gradient approximation made simple. *Physical Review Letters*, 77(18):3865–3868, October 1996.

[42] Jochen Heyd, Gustavo E Scuseria, and Matthias Ernzerhof. Hybrid functionals based on a screened coulomb potential. *The Journal of chemical physics*, 118(18):8207–8215, 2003.

[43] Hannes Jónsson, Greg Mills, and Karsten W Jacobsen. Classical and quantum dynamics in condensed phase simulations, chapter nudged elastic band method for finding minimum energy paths of transitions. *World Scientific, Singapur*, 3:2, 1998.

[44] Lawrence R Pratt. A statistical method for identifying transition states in high dimensional problems. *The Journal of chemical physics*, 85(9):5045–5048, 1986.

[45] Christoph Dellago, Peter G Bolhuis, Félix S Csajka, and David Chandler. Transition path sampling and the calculation of rate constants. *The Journal of Chemical Physics*, 108(5):1964–1977, 1998.

[46] Hongyang Zhao, Pei Bian, and Dongying Ju. Electrochemical performance of magnesium alloy and its application on the sea water battery. *J. Environ. Sci.*, 21:S88 – S91, 2009. ISSN 1001-0742.

[47] Naiguang Wang, Richu Wang, Chaoqun Peng, Yan Feng, and Bin Chen. Effect of hot rolling and subsequent annealing on electrochemical discharge behavior of AP65 magnesium alloy as anode for seawater activated battery. *Corros. Sci.*, 64:17–27, 2012.

[48] Daniel Schloffer, Salar Bozorgi, Pavel Sherstnev, Christian Lenardt, and Bernhard Gollas. Manufacturing and characterization of magnesium alloy foils for use as anode materials in rechargeable magnesium ion batteries. *Journal of Power Sources*, 367:138–144, November 2017.

[49] Jing Zhang, Yuchen Dou, Guobao Liu, and Zhengxiao Guo. First-principles study of stacking fault energies in mg-based binary alloys. *Computational Materials Science*, 79:564–569, November 2013.

[50] Zongrui Pei, Martin Friák, Stefanie Sandlöbes, Roman Nazarov, Bob Svendsen, Dierk Raabe, and Jörg Neugebauer. Rapid theory-

guided prototyping of ductile mg alloys: from binary to multi-component materials. *New Journal of Physics*, 17(9):093009, September 2015.

[51] R. V. Mises. Mechanik der plastischen formänderung von kristallen. *ZAMM - Zeitschrift für Angewandte Mathematik und Mechanik*, 8 (3):161–185, 1928.

[52] M. H. Yoo. Slip, twinning, and fracture in hexagonal close-packed metals. *Metallurgical Transactions A*, 12(3):409–418, March 1981.

[53] Zhaoxuan Wu and W. A. Curtin. The origins of high hardening and low ductility in magnesium. *Nature*, 526(7571):62–67, September 2015.

[54] G. Kresse and J. Furthmüller. Efficiency of ab-initio total energy calculations for metals and semiconductors using a plane-wave basis set. *Computational Materials Science*, 6(1):15–50, July 1996.

[55] G. Kresse and J. Furthmüller. Efficient iterative schemes forab initiototal-energy calculations using a plane-wave basis set. *Physical Review B*, 54(16):11169–11186, October 1996.

[56] P. E. Blöchl. Projector augmented-wave method. *Physical Review B*, 50(24):17953–17979, December 1994.

[57] Richard Tran, Zihan Xu, Balachandran Radhakrishnan, Donald Winston, Wenhao Sun, Kristin A. Persson, and Shyue Ping Ong. Surface energies of elemental crystals. *Scientific Data*, 3(1), September 2016.

[58] Shyue Ping Ong, William Davidson Richards, Anubhav Jain, Geoffroy Hautier, Michael Kocher, Shreyas Cholia, Dan Gunter, Vincent L. Chevrier, Kristin A. Persson, and Gerbrand Ceder. Python materials genomics (pymatgen): A robust, open-source python library for materials analysis. *Computational Materials Science*, 68: 314–319, February 2013.

[59] Y. Wang, L.-Q. Chen, Z.-K. Liu, and S.N. Mathaudhu. First-principles calculations of twin-boundary and stacking-fault energies in magnesium. *Scripta Materialia*, 62(9):646–649, May 2010.

[60] Ma Qian, D.H. StJohn, and M.T. Frost. Characteristic zirconium-rich coring structures in mg–zr alloys. *Scripta Materialia*, 46(9): 649–654, May 2002.

[61] J. L. Murray. The mg-ti (magnesium-titanium) system. *Bulletin of Alloy Phase Diagrams*, 7(3):245–248, June 1986.

[62] J.H. Schaum and H.C. Burnett. Magnesium-rich side of the magnesium-zirconium constitution diagram. *Journal of Research of the National Bureau of Standards*, 49(3):155, September 1952.

[63] Renu Agarwal, Jung Joong Lee, Hans Leo Lukas, and Ferdinand Sommer. Calorimetric measurements and thermodynamic optimization of the ca-mg system. *Zeitschrift für Metallkunde*, 86(2): 103–108, 1995.

[64] Yunfei Ding, Cuie Wen, Peter Hodgson, and Yuncang Li. Effects of alloying elements on the corrosion behavior and biocompatibility of biodegradable magnesium alloys: A review. *J. Mater. Chem. B*, 2(14):1912–1933, 2014. ISSN 2050-750X, 2050-7518.

[65] Aadil Benmayza, Mayandi Ramanathan, Nikhilendra Singh, Fuminori Mizuno, and Jai Prakash. Electrochemical and thermal studies of bismuth electrodes for magnesium-ion cells. *Journal of The Electrochemical Society*, 162(8):A1630, 2015.

[66] Yanna NuLi, Jun Yang, Jiulin Wang, and Yun Li. Electrochemical intercalation of mg2+ in magnesium manganese silicate and its application as high-energy rechargeable magnesium battery cathode. *The Journal of Physical Chemistry C*, 113(28):12594–12597, 2009.

[67] Zhiguo Wang, Qiulei Su, Jianjian Shi, Huiqiu Deng, GQ Yin, Jian Guan, MP Wu, YL Zhou, HL Lou, and Yong Qing Fu. Comparison of tetragonal and cubic tin as anode for mg ion batteries. *ACS applied materials & interfaces*, 6(9):6786–6789, 2014.

[68] Steven Groves and William Paul. Band structure of gray tin. *Physical Review Letters*, 11(5):194, 1963.

[69]   GA Busch and R Kebn. Semiconducting properties of gray tin. In *Solid State Physics*, volume 11, pages 1–40. Elsevier, 1960.

[70]   Oleksandr I Malyi, Teck L Tan, and Sergei Manzhos. In search of high performance anode materials for mg batteries: Computational studies of mg in ge, si, and sn. *Journal of Power Sources*, 233:341–345, 2013.

[71]   Dan-Thien Nguyen, Xuan Minh Tran, Joonsup Kang, and Seung-Wan Song. Magnesium storage performance and surface film formation behavior of tin anode material. *ChemElectroChem*, 3(11): 1813–1819, 2016.

[72]   Jin Hyun Chang, Christian Baur, Jean-Marcel Ateba Mba, Denis Arčon, Gregor Mali, Dorothea Alwast, R Jürgen Behm, Maximilian Fichtner, Tejs Vegge, and Juan Maria Garcia Lastra. Superoxide formation in li 2 vo 2 f cathode material–a combined computational and experimental investigation of anionic redox activity. *Journal of Materials Chemistry A*, 8(32):16551–16559, 2020.

[73]   Jin Hyun Chang, David Kleiven, Marko Melander, Jaakko Akola, Juan Maria Garcia-Lastra, and Tejs Vegge. Clease: a versatile and user-friendly implementation of cluster expansion method. *Journal of Physics: Condensed Matter*, 31(32):325901, 2019.

[74]   Ying Shirley Meng and M Elena Arroyo-de Dompablo. First principles computational materials design for energy storage materials in lithium ion batteries. *Energy & Environmental Science*, 2(6): 589–609, 2009.

[75]   Kang Wang, Du Cheng, Chu-Liang Fu, and Bi-Cheng Zhou. First-principles investigation of the phase stability and early stages of precipitation in mg-sn alloys. *Physical Review Materials*, 4(1): 013606, 2020.

[76]   Hendrik J Monkhorst and James D Pack. Special points for brillouin-zone integrations. *Physical review B*, 13(12):5188, 1976.

[77] Atsuto Seko, Yukinori Koyama, and Isao Tanaka. Cluster expansion method for multicomponent systems based on optimal selection of structures for density-functional theory calculations. *Physical Review B*, 80(16):165122, 2009.

[78] Atsuto Seko and Isao Tanaka. Cluster expansion of multicomponent ionic systems with controlled accuracy: importance of long-range interactions in heterovalent ionic systems. *Journal of physics: Condensed matter*, 26(11):115403, 2014.

[79] Axel Van De Walle and Gerbrand Ceder. Automating first-principles phase diagram calculations. *Journal of Phase Equilibria*, 23(4):348–359, 2002.

[80] AA Nayeb-Hashemi and JB Clark. The mg- sn (magnesium-tin) system. *Bulletin of Alloy Phase Diagrams*, 5(5):466–476, 1984.

[81] AK Nayak and W Oelsen. Quantitative thermal analysis of magnesium-tin alloys by calorimetric measurement for the determination of solidus and liquidus curves. *TRANS. INDIAN INST. METALS*, 22(3):53–58, 1969.

[82] Andrew H Nguyen, Conrad W Rosenbrock, and Gus LW Hart. The robustness of cluster expansion: Assessing the role of relaxation. In *APS March Meeting Abstracts*, volume 2016, pages K22–005, 2016.

[83] Axel Van De Walle. Multicomponent multisublattice alloys, non-configurational entropy and other additions to the alloy theoretic automated toolkit. *Calphad*, 33(2):266–278, 2009.

[84] A Van der Ven and G Ceder. Ordering in lix (ni0. 5mn0. 5) o2 and its relation to charge capacity and electrochemical behavior in rechargeable lithium batteries. *Electrochemistry communications*, 6(10):1045–1050, 2004.

[85] Fleur Legrain and Sergei Manzhos. Understanding the difference in cohesive energies between alpha and beta tin in dft calculations. *AIP Advances*, 6(4):045116, 2016.

[86] Anubhav Jain, Shyue Ping Ong, Geoffroy Hautier, Wei Chen, William Davidson Richards, Stephen Dacek, Shreyas Cholia, Dan Gunter, David Skinner, Gerbrand Ceder, and Kristin A. Persson. Commentary: The materials project: A materials genome approach to accelerating materials innovation. *APL Materials*, 1 (1):011002, 2013.

[87] Klaus-Jürgen Range, Georg H Grosch, and Martina Andratschke. Studies on ab2-type intermetallic compounds. part v1. the crystal structure of mg9sn5, a supposed high-pressure modification of mg2sn. *Journal of alloys and compounds*, 244(1-2):170–174, 1996.

[88] Fleur Legrain, Oleksandr I Malyi, Clas Persson, and Sergei Manzhos. Comparison of alpha and beta tin for lithium, sodium, and magnesium storage: An ab initio study including phonon contributions. *The Journal of Chemical Physics*, 143(20):204701, 2015.

[89] Dan-Thien Nguyen and Seung-Wan Song. Magnesium stannide as a high-capacity anode for magnesium-ion batteries. *Journal of Power Sources*, 368:11–17, 2017.

[90] DRG Mitchell and SE Donnelly. A transmission electron microscopy study of the $\beta \to \alpha$-phase transformation of tin. *Philosophical Magazine A*, 63(4):747–755, 1991.

[91] K. Ojima, Y. Taneda, and A. Takasaki. Direct observation of $\alpha \to \beta$ transformation in tin by transmission electron microscopy. *physica status solidi (a)*, 139(1):139–144, 1993.

[92] Georg Bieker, Verena Küpers, Martin Kolek, and Martin Winter. Intrinsic differences and realistic perspectives of lithium-sulfur and magnesium-sulfur batteries. *Communications Materials*, 2(1):1–12, 2021.

[93] Sheng-Heng Chung and Arumugam Manthiram. Current status and future prospects of metal–sulfur batteries. *Advanced Materials*, 31(27):1901125, 2019.

[94] Yasin Emre Durmus, Huang Zhang, Florian Baakes, Gauthier Desmaizieres, Hagay Hayun, Liangtao Yang, Martin Kolek, Verena

Küpers, Jürgen Janek, Daniel Mandler, et al. Side by side battery technologies with lithium-ion based batteries. *Advanced energy materials*, 10(24):2000089, 2020.

[95] Xiaodong Hong, Jun Mei, Lei Wen, Yueyu Tong, Anthony J Vasileff, Liqun Wang, Ji Liang, Ziqi Sun, and Shi Xue Dou. Non-lithium metal–sulfur batteries: steps toward a leap. *Advanced materials*, 31(5):1802822, 2019.

[96] Chen-Xi Zu and Hong Li. Thermodynamic analysis on energy densities of batteries. *Energy & Environmental Science*, 4(8):2614–2624, 2011.

[97] Richard Schmuch, Ralf Wagner, Gerhard Hörpel, Tobias Placke, and Martin Winter. Performance and cost of materials for lithium-based rechargeable automotive batteries. *Nature Energy*, 3(4):267–278, 2018.

[98] K Hans Wedepohl. The composition of the continental crust. geochem. cosmochim. acta 59, 1217–1232, 1995.

[99] Ivgeni Shterenberg, Michael Salama, Hyun Deog Yoo, Yosef Gofer, Jin-Bum Park, Yang-Kook Sun, and Doron Aurbach. Evaluation of (cf3so2) 2n-(tfsi) based electrolyte solutions for mg batteries. *Journal of The Electrochemical Society*, 162(13):A7118, 2015.

[100] Zhirong Zhao-Karger and Maximilian Fichtner. Magnesium–sulfur battery: its beginning and recent progress. *MRS Communications*, 7(4):770–784, 2017.

[101] Zhirong Zhao-Karger, Xiangyu Zhao, Di Wang, Thomas Diemant, R Jürgen Behm, and Maximilian Fichtner. Performance improvement of magnesium sulfur batteries with modified non-nucleophilic electrolytes. *Advanced Energy Materials*, 5(3):1401155, 2015.

[102] Tao Gao, Xiao Ji, Singyuk Hou, Xiulin Fan, Xiaogang Li, Chongying Yang, Fudong Han, Fei Wang, Jianjun Jiang, Kang Xu, et al. Thermodynamics and kinetics of sulfur cathode during discharge in mgtfsi2–dme electrolyte. *Advanced Materials*, 30(3):1704313, 2018.

[103] Joachim Häcker, Christian Danner, Brigitta Sievert, Indro Biswas, Zhirong Zhao-Karger, Norbert Wagner, and K Andreas Friedrich. Investigation of magnesium–sulfur batteries using electrochemical impedance spectroscopy. *Electrochimica Acta*, 338:135787, 2020.

[104] Hiroaki Nakamura, Youichi Ogawa, Akira Kasahara, et al. Ionic and positive hole conductivities of solid magnesium and strontium sulfides. *Transactions of the Japan institute of metals*, 25(10):692–697, 1984.

[105] Hiroaki Nakamura, Youichi Ogawa, Akira Kasahara, and Satoshi Iwasaki. Sulfur pressure dependence of electrical conductivity of group iia and iiia metal sulfides. *Materials Transactions, JIM*, 36 (10):1263–1270, 1995.

[106] Upendra Puntambekar, Sunder Veliah, and Ravindra Pandey. Point-defects in magnesium sulfide. *Journal of materials research*, 9(1):132–134, 1994.

[107] Tina Chen, Gopalakrishnan Sai Gautam, and Pieremanuele Canepa. Ionic transport in potential coating materials for mg batteries. *Chemistry of Materials*, 31(19):8087–8099, 2019.

[108] Sten Haastrup, Mikkel Strange, Mohnish Pandey, Thorsten Deilmann, Per S Schmidt, Nicki F Hinsche, Morten N Gjerding, Daniele Torelli, Peter M Larsen, Anders C Riis-Jensen, et al. The computational 2d materials database: high-throughput modeling and discovery of atomically thin crystals. *2D Materials*, 5(4):042002, 2018.

[109] Aliaksandr V Krukau, Oleg A Vydrov, Artur F Izmaylov, and Gustavo E Scuseria. Influence of the exchange screening parameter on the performance of screened hybrid functionals. *The Journal of chemical physics*, 125(22):224106, 2006.

[110] Maxim Shishkin and Georg Kresse. Self-consistent g w calculations for semiconductors and insulators. *Physical Review B*, 75 (23):235102, 2007.

[111] Christoph Freysoldt, Jörg Neugebauer, and Chris G Van de Walle. Fully ab initio finite-size corrections for charged-defect supercell calculations. *Physical review letters*, 102(1):016402, 2009.

[112] Danny Broberg, Bharat Medasani, Nils ER Zimmermann, Guodong Yu, Andrew Canning, Maciej Haranczyk, Mark Asta, and Geoffroy Hautier. Pycdt: A python toolkit for modeling point defects in semiconductors and insulators. *Computer Physics Communications*, 226:165–179, 2018.

[113] Richard JD Tilley. *Defects in solids*. John Wiley & Sons, 2008.

[114] Graeme Henkelman and Hannes Jónsson. Improved tangent estimate in the nudged elastic band method for finding minimum energy paths and saddle points. *The Journal of chemical physics*, 113(22):9978–9985, 2000.

[115] Ask Hjorth Larsen, Jens Jørgen Mortensen, Jakob Blomqvist, Ivano E Castelli, Rune Christensen, Marcin Dułak, Jesper Friis, Michael N Groves, Bjørk Hammer, Cory Hargus, et al. The atomic simulation environment—a python library for working with atoms. *Journal of Physics: Condensed Matter*, 29(27):273002, 2017.

[116] Gregor Mali. Ab initio crystal structure prediction of magnesium (poly) sulfides and calculation of their nmr parameters. *Acta Crystallographica Section C: Structural Chemistry*, 73(3):229–233, 2017.

[117] William Primak, Herman Kaufman, and Roland Ward. X-ray diffraction studies of systems involved in the preparation of alkaline earth sulfide and selenide phosphors1. *Journal of the American Chemical Society*, 70(6):2043–2046, 1948.

[118] Stephan Lany. Polymorphism, band-structure, band-lineup, and alloy energetics of the group ii oxides and sulfides mgo, zno, cdo, mgs, zns, cds. In *Oxide-based Materials and Devices V*, volume 8987, pages 109–116. SPIE, 2014.

[119] Changming Zhao, Yifeng Duan, Jie Gao, and Huafeng Dong. Crystal and band structures of zns, mgs, and zns-mgs alloys. *Journal of Applied Physics*, 121(23):235705, 2017.

[120] Jeffrey G Smith, Junichi Naruse, Hidehiko Hiramatsu, and Donald J Siegel. Intrinsic conductivity in magnesium–oxygen battery discharge products: Mgo and mgo2. *Chemistry of Materials*, 29(7): 3152–3163, 2017.

[121] James E Saal, Scott Kirklin, Muratahan Aykol, Bryce Meredig, and Christopher Wolverton. Materials design and discovery with high-throughput density functional theory: the open quantum materials database (oqmd). *Jom*, 65(11):1501–1509, 2013.

[122] John R Taylor, Chris D Zafiratos, and Michael Andrew Dubson. *Modern physics for scientists and engineers.* 2004.

[123] Mark James Abraham, Teemu Murtola, Roland Schulz, Szilárd Páll, Jeremy C Smith, Berk Hess, and Erik Lindahl. Gromacs: High performance molecular simulations through multi-level parallelism from laptops to supercomputers. *SoftwareX*, 1:19–25, 2015.

[124] US Coast Guard. Chemical hazard response information system (chris)-hazardous chemical data. *Commandant Instruction*, 16465, 1999.

[125] John B Goodenough and Youngsik Kim. Challenges for rechargeable li batteries. *Chemistry of materials*, 22(3):587–603, 2010.

[126] AK Padhi, V Manivannan, and JB Goodenough. Tuning the position of the redox couples in materials with nasicon structure by anionic substitution. *Journal of the Electrochemical Society*, 145 (5):1518, 1998.

[127] Shou-Hang Bo, Clare P Grey, and Peter G Khalifah. Defect-tolerant diffusion channels for mg2+ ions in ribbon-type borates: Structural insights into potential battery cathodes mgvbo4 and mg x fe2–x b2o5. *Chemistry of Materials*, 27(13):4630–4639, 2015.

[128] Hugh Glass. *Borate polyanion-based systems as Li-and Mg-ion cathode materials.* PhD thesis, University of Cambridge, 2017.

[129] G-C Guo, W-D Cheng, J-T Chen, H-H Zhuang, J-S Huang, and Q-E Zhang. Monoclinic mg2b2o5. *Acta Crystallographica Section C: Crystal Structure Communications*, 51(12):2469–2471, 1995.

[130] Gábor I Csonka, John P Perdew, Adrienn Ruzsinszky, Pier HT Philipsen, Sébastien Lebègue, Joachim Paier, Oleg A Vydrov, and János G Ángyán. Assessing the performance of recent density functionals for bulk solids. *Physical Review B*, 79(15):155107, 2009.

Included publications

Paper I
Computational Design of Ductile Magnesium Alloy Anodes for Magnesium Batteries
Smobin Vincent, Jin Hyun Chang, and Juan Maria García Lastra
Batteries & Supercaps, 4, 522 (2021)

Computational Design of Ductile Magnesium Alloy Anodes for Magnesium Batteries

Smobin Vincent,[a] Jin Hyun Chang,[a] and Juan Maria Garcia Lastra*[a]

The main advantage of Mg batteries over other metal counterparts is its ability to work with a pure metallic anode, achieving a very high specific capacity. Unfortunately, pure Mg is hard to machine due to its brittleness, making it extremely difficult to produce foils that are thin enough for practical battery applications. Alloying Mg with small amounts of doping elements can enhance its ductility. However, care should be given to ensure that the dopants do not interfere with the electrochemical process of plating and stripping of Mg from the anode during battery operation. Dopants should prefer to be in bulk or at a stacking fault rather than migrating to the surface to meet this requirement. In this work, we carried out a computational screening of 34 dopants that are reported to reduce Mg brittleness to check which of them energetically prefers to stay in bulk. We found that only 12 out of the 34 meet such a criterion. Y and Nd, two of the main dopants in the WE43 commercial alloys, are among the 12 beneficial doping elements, which presents a practical avenue for the exploration for superior Mg battery anode material.

1. Introduction

Rechargeable magnesium batteries (RMBs) are a promising alternative to secondary rechargeable lithium batteries due to the relative abundance of magnesium compared to that of lithium. From the technical point of view, the main advantage of RMB is its ability to operate with a pure metallic anode since the plating and stripping of magnesium do not promote the formation of dendrites, unlike the metallic lithium counterpart. Thanks to this property, RMBs display high volumetric capacity. However, one of the major obstacles in developing RMBs is the formation of a passivation layer at the magnesium metal anode surface in contact with conventional electrolytes such as $Mg(BF_4)_2$ or $Mg(ClO_4)_2$. The passivation layer hinders the diffusion of Mg ions and lowers the coulombic efficiency.[1] There are two proposed solutions to overcome the problems stemming from the passivation layer formation.

The first method is to use metals that form an alloy with magnesium as anode material. The magnesium still acts as a charge carrier that gets deposited on the anode upon charge, forming an alloy with the host anode metal. Several studies reported the use of Bi, Sn, Sb, In and Bi–Sb as an anode for RMB.[2–5] Even though reversible magnesiation is possible in these systems, they face some challenges such as capacity loss at high C-rates, sluggish Mg-ion kinetics and pulverisation of electrode due to volume expansion.[1,6]
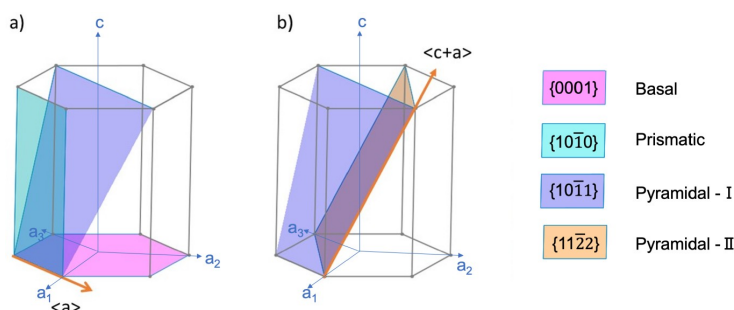
The second route to suppress the passivation layer is to develop electrolytes alternative to the conventional $Mg(BF_4)_2$ and $Mg(ClO_4)_2$. Aurbach et al. reported a breakthrough by proposing organohaloaluminate-based electrolytes in ethereal solutions.[7] Several groups have followed up with the seminal work by Aurbach et al. to further develop new-generation electrolytes suitable for rechargeable RMBs. Some examples include the all-phenyl complex (APC) electrolyte $((PhMgCl)_2–AlCl_3$ in tetrahydrofuran (THF)),[8] the magnesium aluminium chloride complex (MACC) electrolyte $(MgCl_2–AlCl_3$ in dimethyl ether (DME)),[9] the $Mg(CB_{11}H_{12})_2$ salt in THF or DME[10] and the $Mg[B(HFIP)_4]_2$ salt in diglyme.[11]

Although developing a new electrolyte presents a promising avenue for future RMB research, magnesium also suffers from being too brittle. The brittle nature of magnesium is a serious obstacle to overcome in fabricating sufficiently thin foils to be used as RMB anodes. Consequently, magnesium anode's ductility has to be increased to develop practical RMBs in conjunction with next-generation electrolytes that suppress the formation of the passivation layer. Magnesium exhibits low ductility due to its hexagonal crystal structure. Existing experimental and theoretical studies indicate that doping magnesium with suitable elements will promote the formation of stacking faults, which in turn improves the ductility of magnesium.[12,13] Stacking faults are crystal imperfections formed due to the addition or removal of an atomic layer. The excess energy per unit area due to the faults is known as stacking fault energy (SFE). There are three main types of basal stacking faults for Mg: one extrinsic stacking fault with ABABCABAB stacking sequence and two intrinsic stacking faults with ABABCBCB (called I_1) and ABABCACA (called I_2) stacking sequences. Sandlöbes et al. reported that reduction in the SFE of I_1 stacking fault (I_1SF) on doping improves the ductility of magnesium.[13]

Experimental reports on the use of doped Mg as RMB anode are relatively scarce. In aqueous electrolytes, Zhao et al.[14] and Wang et al.[15] have tested the AZ31 commercial alloys (Mg-3 wt% Al-1 wt% Zn). Wang et al. also tested AP65 (Mg-6 wt% Al-5 wt% Pb).[15] According to their reports, both AZ31 and AP65 exhibit larger overpotentials than pure Mg.

[a] S. Vincent, Prof. Dr. J. H. Chang, Prof. Dr. J. M. Garcia Lastra
Department of Energy Conversion and Storage
Technical University of Denmark
DK-2800 Kgs. Lyngby, Denmark
E-mail: jmgla@dtu.dk

Batteries & Supercaps

Articles
doi.org/10.1002/batt.202000240

Chemistry Europe
European Chemical
Societies Publishing

Figure 1. Possible slip systems in the hexagonal system. a) Basal, prismatic and pyramidal-I slip systems in $\langle a \rangle$ direction and b) pyramidal-I and pyramidal-II slip systems in $\langle c + a \rangle$ direction.

Regarding non-aqueous electrolytes, Schloffer et al. studied Mg-1.55 wt% Gd, Mg-1.63 wt% Zn and Mg-1.02 wt% Gd-1.01 wt% Zn alloys with APC as an electrolyte.[16] They observed that after 5 cycles, only the samples doped exclusively with Zn were showing a clear overpotential. Very recently, Mandai and Somekawa made a systematic analysis of Mg doped at 0.3 wt% with nine different elements, namely Ag, Al, Bi, Ca, Li, Mn, Sn, Y and Zn, with Mg[B(HFIP)$_4$]$_2$/diglyme salt-electrolyte combination.[11] They reported that Zn and Bi increase the overpotential with respect to pure Mg, while Ag and Ca decrease it. The other five elements (Al, Li, Mn, Sn and Y) did not seem to have any noticeable effect on the overpotential. The reason for the different influence of the dopants on the overpotentials remains unclear.

In this work, we hypothesize that the dopants that modify the electrochemical properties of Mg, either benignly or detrimentally, are those that either segregate or migrate towards the surface of the system. By contrast, those dopants that stay at the bulk will be electrochemically inert (i.e., they will not affect the overpotentials, the electron conductivity at the surface, corrosion or passivation at the anode). Ideally, one should try to find dopants that enhance Mg ductility while concomitantly improve its electrochemical properties. The latter may be difficult to rationalize since several complex processes such as Mg diffusion at the surface and Mg solvation/disolvation need to be accounted for, and they depend on the electrolyte being used. A more conservative approach is to focus solely on seeking dopants that reduce Mg brittleness without interfering with the electrochemical processes. Our strategy ensures to increase the ductility of RMB anode without sacrificing any other property.

Several authors have used density functional theory (DFT) to perform an exhaustive search to find suitable doping elements that improve the ductility of magnesium.[12,13,17,18] The work of Zhang et al. has identified a set of 34 elements that improve the ductility of magnesium.[17] As an initial step of the investigation, we took these 34 elements and confirmed that they lower the SFE of I_1SF on alloying with magnesium based on our DFT calculations. As the dopants' impact on the electrochemical properties of the magnesium anode has not been explored, we investigated their propensity to migrate to the surface. Based on the propensity criterion, we have identified 12 dopants that could be added to magnesium to form a suitable ductile alloy anode without compromising its electrochemical properties. Some of the identified systems can be readily purchased for further testing as they are commercially available.

This paper is structured into four sections. A short discussion on the brittleness of magnesium and how stacking faults helps to improve its ductility is presented in section 1.1. The following section covers the methodology and computational details. The main results of this work are presented and discussed in Section 2. Some final comments are provided in the last section.

1.1. Ductility in Magnesium

The brittleness of Mg originates from its insufficient number of independent slip systems needed to accommodate deformations. According to the Von Mises criterion, a material requires five independent slip systems to allow deformations.[19] The possible slip systems in an hcp crystal, the crystal structure of magnesium at room temperature, are illustrated in Figure 1. The corresponding number of independent slip systems are listed in Table 1.

Basal and prismatic slips along $\langle a \rangle$ direction offer two independent slip systems each. The four slip systems of pyramidal-I along $\langle a \rangle$ direction are crystallographically equivalent to the combination of basal $\langle a \rangle$ and prismatic $\langle a \rangle$ slips.[20] Therefore, only four independent slip systems are attainable in

Table 1. Independent slip systems in the magnesium crystal system.[20]

Direction	Plane	Number of independent slip systems
$\langle a \rangle$	Basal	2
	Prismatic	2
	Pyramidal-I	4
$\langle c + a \rangle$	Pyramidal-I	5
	Pyramidal-II	5

Batteries & Supercaps

Articles
doi.org/10.1002/batt.202000240

Chemistry Europe
European Chemical
Societies Publishing

⟨a⟩ direction. On the other hand, pyramidal-I and pyramidal-II slips along ⟨c+a⟩ direction offer five independent slip systems, and activating any of the slips along ⟨c+a⟩ direction can satisfy the Von Mises criterion. Wu and Curtin showed that ⟨c+a⟩ dislocations are metastable even in pure Mg once formed, although their formation is energetically unfavorable.[21] Therefore, finding dopants that activate and further stabilize the ⟨c+a⟩ dislocations is a suitable strategy to enhance the ductility of Mg.

The dopants activate ⟨c+a⟩ dislocations through the promotion of stacking faults.[12] Sandlöbes et al. investigated the relationship between ductility and SFEs in Mg and Mg−Y alloys.[13] They observed a reduction in SFE of Mg upon alloying with Y and reported that the improved ductility of Mg−Y alloys was due to the high activity of pyramidal-I and pyramidal-II ⟨c+a⟩ dislocations. The plausible explanation for this is that I_1 stacking fault (I_1SF) can act as a nucleation source for ⟨c+a⟩ dislocations.[13] Thus, dopants that reduce the SFE (relative to that of pure Mg) for the I_1SF will promote ⟨c+a⟩ dislocations, and consequently will enhance Mg ductility. Therefore, we limit the scope of the stacking faults to I_1SF in this study.

Computational Methods

Three conditions need to be fulfilled in order to assess whether the addition of dopants is beneficial for RMB applications:

- The dopant should improve magnesium's ductility (the SFE for the I_1SF should be lowered after dopant addition).
- The dopant hast to form a thermodynamically stable alloy with magnesium.
- The dopant should be more stable either in bulk or at stacking faults than on the surface to form a dopant-free surface.

Regarding the first condition, the first-principle study of Zhang et al. on I_1SF identified 34 dopants that decrease the SFE of magnesium.[17] These elements are Al, Ba, Bi, Ca, Ce, Cs, Dy, Er, Eu, Ga, Gd, Hf, Ho, In, K, La, Lu, Na, Nd, Pb, Pr, Rb, Sc, Sm, Sn, Sr, Tb, Ti, Tl, Tm, Y, Yb, Zn and Zr. In our study, we restricted ourselves to this set of 34 dopants with a doping concentration of ∼2.08% for all alloy structures (i.e., one dopant atom per 48 atoms), which lies in the typical doping level of commercial alloys (∼1% to 3%). We carried out our own first-principle I_1SF study since the SFE depends on the doping level, while no SFEs have been reported for a 2.08% doping concentration to the best of our knowledge.

The SFE for the I_1SF was calculated using

$$\text{SFE} = \frac{E^{I_1\text{SF}} - E^{\text{bulk}}}{2A},\qquad(1)$$

where $E^{I_1\text{SF}}$ and E^{bulk} are the energies of the structures with and without stacking faults, respectively. A is the area of the stacking fault plane, which corresponds to the area of the XY plane in this work. The term "bulk" refers to the bulk of the material in a pristine form without stacking faults. The I_1SF and bulk structures used in the calculations are shown in Figure 2. We tested the size of the SF supercell to make sure that the interactions between the SF defects are negligible. The change in SFE for the supercells with SFs separated by more than 8 atomic layers is less than 1 mJ/m². To perform calculations with low doping concentration (∼2.08%), we employed $2 \times 2 \times 12$ supercell of hcp containing 96 atoms for both structures, and two magnesium atoms were substituted with
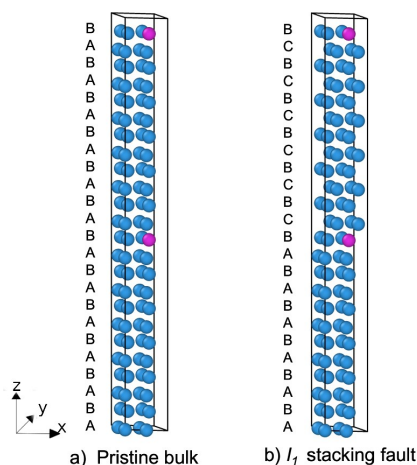
Figure 2. Structures of a) pristine bulk and b) I_1SF. Mg atoms are shown in blue and the dopants are shown in pink.

the dopants for the alloy structures. Due to periodic boundary conditions, the I_1SF structure has two stacking-fault planes separated by 12 atomic layers to minimize the interaction between them, and a dopant was placed on each of the stacking faults.

We used Vienna Ab initio Simulation Package (VASP) to perform first-principle calculations based on DFT.[22,23] The Perdew-Burke-Ernzerhof (PBE) parameterized generalized-gradient approximation (GGA) functional was employed to describe the exchange and correlation effects,[24] and the projector augmented wave (PAW) method was used to account for the core-valence interaction.[25] A plane-wave basis set with cut-off energy of 520 eV was used for all calculations. The Brillouin zone is integrated with the k-point mesh generated using the Monkhorst-Pack scheme with a k-point density of 4.5 per Å⁻¹ for all the structures. The convergence of the k-point density was tested for magnesium and all other elements in this study, and the difference in total energy was found to be less than 2 meV/atom. The convergence criterion for the electronic self-consistent loop was set to 10^{-6} eV, and the atomic positions were relaxed until the force on each atom reached below 10^{-2} eV/Å⁻¹. The structure and atomic positions were relaxed for both bulk and I_1SF structures, and only the atomic positions were relaxed for the slabs.

The second and third conditions (the alloy stability and the dopant's propensity to migrate to the surface, respectively) were evaluated based on conventional expressions for formation energies. The formation energies of an alloy when a dopant is in bulk, at stacking fault or on the surfaces were calculated using

$$E_f^{struct} = \frac{E^{struct}(\text{Mg}_{m-n}\text{X}_n) - E^{struct}(\text{Mg}_m) - nE(\text{X}) + nE(\text{Mg})}{n},\qquad(2)$$

where *struct* can be either bulk, I_1SF, or surface terminations (e.g., (0001), (10̄10), and (10̄11)). $E^{struct}(\text{Mg}_{m-n}\text{X}_n)$ is the energy of the structure where n out of m Mg atoms are substituted with dopant atoms. $E^{struct}(\text{Mg}_m)$ is the energy of the same structure with no dopants (i.e., all m atoms are Mg). $E(\text{X})$ is the energy per atom of X in its most stable crystalline structure. $E(\text{Mg})$ is the energy per atom of Mg in hcp. All the simulations for calculating formation energies have the same calculation parameters used for the stacking fault simulations for consistency. In addition, the number

of atoms in the supercells was kept to 96 for all the cases (i.e., $m = 96$ in Eq. (2)), with two dopant atoms placed as far apart from each other as possible.

The stability of the alloy (second condition) was evaluated based on the formation energy with the dopant in the bulk/stacking fault. The E_f^{bulk} or $E_f^{I_1 SF}$ should be negative to form a stable alloy. The dopants will segregate and form a separate phase if they are positive. The energy of the bulk and I_1SF structures were also computed using the structure shown in Figure 2. The propensity of the dopant to migrate to the surface (third condition) was analyzed by comparing the formation energies of the alloys when the dopant is in bulk and at stacking fault versus on surfaces. The relative energy of the dopant in bulk and at stacking fault versus on the surface are written as

$$\Delta E^{bulk} = E_f^{bulk} - E_f^{surface} \qquad (3)$$

and

$$\Delta E^{I_1 SF} = E_f^{I_1 SF} - E_f^{surface}, \qquad (4)$$

respectively. The superscript 'surface' refers to one of (0001), (10$\bar{1}$0) and (10$\bar{1}$1) surface terminations considered, and the $E_f^{surface}$ is for the most thermodynamically favorable Mg surface for the dopant. At least one of ΔE^{bulk} or $\Delta E^{I_1 SF}$ should be negative to ensure that the dopant does not migrate to the surface.

The preliminary step for assessing the migration of the dopants towards the surface is to determine which Mg surface terminations are thermodynamically most favorable. The surfaces formed in magnesium at equilibrium condition were identified using the Wulff plot analysis. The 12 symmetrically distinct surfaces in magnesium crystal with the lowest Miller indices were considered for the Wulff construction. We followed the methodology in the work of Tran et al.[26] to obtain the Wulff plot using our lattice constants and simulation parameters. Tran et al. reported that the minimum thickness of 10 Å for both slab and vacuum is sufficient to converge surface energies to within 0.02 J/m^2. We used slab structures with two surfaces separated by a minimum of 8 atomic layers (> 10 Å) and vacuum thickness of 10 Å for the surface energy calculations. The surface energy, γ^{surf}, of different surfaces required for obtaining the Wulff shape is calculated using

$$\gamma^{surf} = \frac{E^{slab} - n^{slab}E_{Mg}}{2A^{slab}}, \qquad (5)$$

where E^{slab} is the energy of the slab model with the surface, n^{slab} is the number of atoms in slab structure and A^{slab} is the area of the slab along the surface plane. The Wulff shape was obtained using the Wulff analysis module implemented in Pymatgen.[26,27] After identifying the surfaces formed in magnesium at equilibrium conditions, the formation energies of the surfaces were calculated using Eq. (2).

2. Results and Discussion

2.1. Ductility analysis

The alloying elements that reduce the SFE of magnesium upon alloying are identified as suitable dopants that enhance the ductility of Mg. The SFEs calculated for the 34 binary magnesium alloys with the dopant concentration of ~2.08%

are given in Table 2. The SFE obtained for the pure magnesium is 21.547 mJ/m^2, which is in agreement with the previous studies.[13,17,28] All the doping elements other than Zn exhibit a reduction in the SFE on alloying with magnesium. The anomalous behavior of Zn is in contrast to the results of Zhang et al. where all the 34 dopants showed a decrease in the SFE.[17] For a 2.08% doping concentration, our results show that SFE for Zn-doped Mg is 1.6 mJ/m^2 larger than that of pure Mg. On the other hand, SFEs of Zn alloys with 1.1% and 2.5% Zn concentrations are more stable than pure Mg by 0.2 mJ/m^2 and 2.3 mJ/m^2, respectively, according to Zhang et al.[17]. One cannot draw a conclusion on the ability of Zn to promote stacking faults based on such small changes in SFE, especially when we account for the inherent DFT inaccuracies and the spurious dopant-dopant interactions of our model. Therefore, Zn was not disregarded for subsequent analyses, especially because Zn is present in numerous commercial Mg alloys.

2.2. Wulff plot analysis

The surface energies calculated for 12 Mg surfaces with the lowest Miller indices are given in Table 3. The equilibrium shape of Mg crystal is obtained using the Wulff plot

Table 2. Calculated SFE and formation energies of the binary Mg alloys with the dopant in bulk, at stacking fault and on surfaces.

System	SFE [mJ/m^2]	E_f^{bulk} [eV]	$E_f^{I_1 SF}$ [eV]	$E_f^{(0001)}$ [eV]	$E_f^{(10\bar{1}1)}$ [eV]	$E_f^{(10\bar{1}0)}$ [eV]
Al	14.083	0.048	0.031	0.096	0.094	0.112
Ba	4.316	1.311	1.273	−0.343	−0.612	−0.580
Bi	−5.679	−0.245	−0.305	−0.779	−0.879	−0.909
Ca	14.084	0.126	0.109	−0.221	−0.330	−0.273
Ce	13.402	0.167	0.150	0.036	0.114	0.125
Cs	−2.044	2.833	2.781	−0.410	−0.573	−0.639
Dy	18.854	−0.010	−0.016	0.280	0.336	0.473
Er	19.081	0.001	−0.004	0.334	0.400	0.533
Eu	6.815	0.411	0.379	−0.209	−0.387	−0.310
Ga	15.219	−0.169	−0.183	−0.158	−0.227	−0.219
Gd	18.400	−0.016	−0.023	0.200	0.254	0.393
Hf	11.358	0.605	0.582	1.435	1.813	1.795
Ho	19.081	−0.007	−0.013	0.307	0.369	0.504
In	11.358	−0.367	−0.399	−0.464	−0.510	−0.501
K	5.452	1.593	1.558	−0.229	−0.380	−0.430
La	14.311	0.310	0.294	0.056	−0.028	0.112
Lu	18.627	0.024	0.018	0.390	0.485	0.612
Na	12.948	0.437	0.419	−0.072	−0.177	−0.218
Nd	15.447	0.080	0.067	0.109	0.096	0.238
Pb	3.407	−0.209	−0.249	−0.545	−0.624	−0.638
Pr	14.538	0.092	0.077	0.050	0.019	0.161
Rb	1.590	1.492	1.448	−1.047	−1.205	−1.256
Sc	18.172	−0.111	−0.118	0.329	0.503	0.523
Sm	17.037	0.031	0.021	0.170	0.186	0.327
Sn	3.862	−0.260	−0.299	−0.467	−0.531	−0.538
Sr	7.042	0.718	0.686	−0.217	−0.431	−0.373
Tb	18.627	−0.006	−0.013	0.256	0.305	0.443
Ti	13.175	0.649	0.630	1.213	1.479	1.429
Tl	11.131	−0.049	−0.072	−0.305	−0.367	−0.382
Tm	19.081	0.012	0.006	0.360	0.428	0.559
Y	18.854	−0.092	−0.098	0.173	0.253	0.377
Yb	11.358	0.282	0.260	−0.079	−0.220	−0.150
Zn	23.170	−0.033	−0.030	−0.015	−0.067	−0.080
Zr	11.131	0.192	0.169	0.999	1.376	1.354
Mg	21.547	–	–	–	–	–

Batteries & Supercaps

Articles
doi.org/10.1002/batt.202000240

Chemistry Europe
European Chemical
Societies Publishing

Table 3. Surface energies and area fraction of 12 surfaces with the lowest Miller indices.

Surface	Surface energy (J/m^2)	Area fraction
(0001)	0.59	0.22
(10$\bar{1}$0)	0.63	0.34
(10$\bar{1}$1)	0.68	0.44
(10$\bar{1}$2)	0.75	0.00
(11$\bar{2}$0)	0.76	0.00
(11$\bar{2}$1)	0.80	0.00
(20$\bar{2}$1)	0.82	0.00
(21$\bar{3}$0)	0.75	0.00
(21$\bar{3}$1)	0.77	0.00
(2$\bar{1}\bar{1}$2)	0.80	0.00
(21$\bar{3}$2)	0.80	0.00
(22$\bar{4}$1)	0.80	0.00

construction using these surface energies as inputs. The computed Wulff shape is shown in Figure 3a. It can be seen from the Wulff shape that (0001), (10$\bar{1}$0) and (10$\bar{1}$1) surfaces are the only surfaces present in Mg at equilibrium conditions. The area fraction of each surface derived from the Wulff shape is given in Table 3. Even though the (0001) surface is the most energetically favorable, most of the area of the equilibrium magnesium surface consists of the (10$\bar{1}$1) surface.

Thus, we only considered the (0001), (10$\bar{1}$0) and (10$\bar{1}$1) surfaces for our study of the propensity of a dopant to migrate to the surface. Again, for the sake of consistency, the formation energies with the dopants at the surfaces were calculated using 96-atoms slab structures with one dopant on each of the two surfaces. The (0001), (10$\bar{1}$0) and (10$\bar{1}$1) surface slabs are visualized in Figure 3.

2.3. Stability analysis

The formation energy of the alloy with the dopant atom in bulk, E_f^{bulk}, or at stacking fault, $E_f^{l,SF}$, should be negative to form a stable alloy. As shown in Table 2, only 14 out of the 34

considered dopants fulfill that condition: Bi, Dy, Er, Ga, Gd, Ho, In, Pb, Sc, Sn, Tb, Tl, Y and Zn. It is worth noting that $E_f^{l,SF}$ is smaller than E_f^{bulk} for all dopants other than Zn, which indicates that these dopants are more favorable to be at stacking fault than in bulk. Er is a special case, being stable only at the stacking fault – all the other stable dopants are stable both in bulk and at the stacking fault. In addition to the 14 dopants that fulfill our stability condition, some dopants such as Al, Lu, Nd, Pr, Sm and Tm display slightly positive values (i.e., less than 0.1 eV for E_f^{bulk} and $E_f^{l,SF}$). Due to the intrinsic errors in DFT, we took a cautious approach and decided not to exclude these 6 dopants at this stage from the pool of potential dopants that are beneficial for Mg-alloy anodes.

A screening based on the stability criterion allows us to disregard 14 out of the 34 dopant candidates. The disregarded dopants were alkali and alkaline earth metals, whose large atomic size compared to that of Mg makes them rather unstable, three rare-earth elements (Eu, La and Yb), and the elements in group 4 of the periodic table (Ti, Zr and Hf). Regarding elements from group 4, there are experimental reports in the literature confirming their low solubility in Mg.[29–31] One could argue the 14 excluded dopants could be metastable at the low doping level considered in this work due to kinetic considerations (e.g., high migration barriers), and they may not segregate to form a separate phase. However, under the operating conditions of the battery where Mg atoms are continuously plated/stripped from the anode, atomic migration is strongly favored, and thus the segregation of metastable dopants would eventually occur.

It is worth to mention explicitly the case of Ca, which was included in the study by Mandai and Somekawa. The Mg-0.3 wt % Ca showed a reduction of the overpotential relative to pure Mg.[11] Our calculation show that Ca and Mg should segregate, which agrees well with experiments.[32] Mandai and Somekawa speculated that the low amounts of Ca dopant in their samples dissolve during the first cycles, producing defects that may function as active sites.

a) Wulff plot   b) (0001) Surface   c) (10$\bar{1}$0) Surface   d) (10$\bar{1}$1) Surface
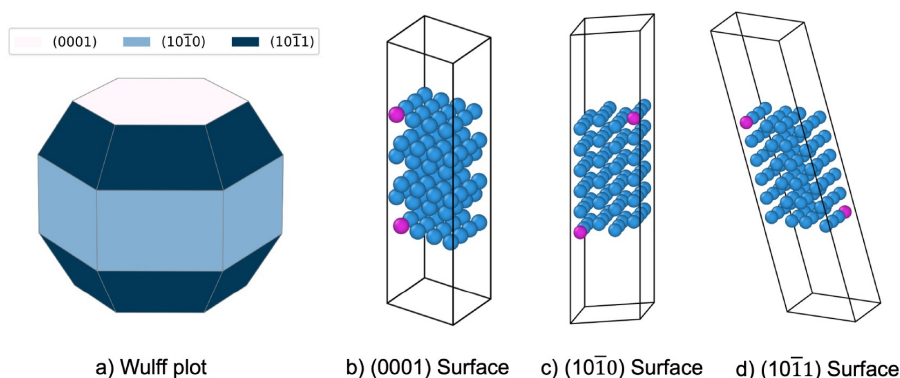
Figure 3. a) Wulff plot of the equilibrium surfaces of Mg. Slab structures used in the surface calculations. b) (0001) surface, c) (10$\bar{1}$0) surface and d) (10$\bar{1}$1) surface. Mg atoms are shown in blue and the dopants are shown in pink.

Batteries & Supercaps

Articles
doi.org/10.1002/batt.202000240

**Chemistry
Europe**

European Chemical
Societies Publishing

2.4. Relative energy analysis

As a final step of the analysis and screening, we evaluated the propensity of the 20 stable dopants to reside in bulk or at stacking fault than migrate to the (0001), (10$\bar{1}$0) or (10$\bar{1}$1) Mg surfaces. While using the surface at which the dopant is most stable as a reference, we evaluate the relative energies of the dopants in bulk and at the stacking fault versus on the surface, which are respectively represented as ΔE^{bulk} and $\Delta E^{I_1\text{SF}}$. The results are shown in Figure 4.

Among the stable magnesium alloys, Al and most of the rare-earth elements (Dy, Er, Gd, Ho, Lu, Nd, Sc, Sm, Tb, Tm and Y) have negative ΔE^{bulk} and $\Delta E^{I_1\text{SF}}$. The negative relative energies imply that these dopants are not prone to migrating to the surface, and thus they are electrochemically inert. In contrast, Bi, Pb, Sn, In and Tl strongly prefer to migrate to the Mg surface, which will interfere in the stripping (deposition) of Mg during the discharge (charge) of the battery and potentially react with the electrolyte. Experiments have shown increased overpotentials for Bi and Pb dopants with respect to pure Mg.[11,15]

It should be pointed out that the propensity of the dopants to migrate to the surface depends on the considered surface termination. For example, Zn and Ga have slightly positive ΔE^{bulk} and $\Delta E^{I_1\text{SF}}$ values because they energetically prefer to be on the (10$\bar{1}$0) or (10$\bar{1}$1) surfaces. However, they are more stable to be in bulk or at the I_1SF compared to the (0001) surface. Our results show a good agreement with the experimental results even for the borderline cases where the magnitudes of ΔE^{bulk} and $\Delta E^{I_1\text{SF}}$ are small. The study of Schloffer et al. on the electrochemical behavior of Mg-1.63 wt% Zn in APC electrolyte reported that the alloy exhibits a high propensity to be passivated,[16] indicating that Zn participates in surface processes. Along the same lines Mandai and Somekawa,[11] Zhao et al.[14] and Wang et al. [15] reported an increased overpotential in

the AZ31 alloy, containing Zn, with respect to pure Mg. Schloffer et al. also showed that the addition of 1.55 wt% Gd does not have any adverse effect on the anode performance.[16] These experimental observations are in good agreement with our findings where Gd does not migrate to Mg surfaces while Zn does.

Based on the identified dopants, the commercial alloy WE43 with a composition of Mg-4 wt% Y-2.25 wt% Nd-0.15 wt% Zr will be a suitable candidate as a magnesium alloy anode. The two main dopants in WE43, Y and Nd, are both stable in bulk, promote stacking faults and do not migrate to the surface. Zr is added to magnesium alloys as a grain refiner although it has limited solubility in magnesium; the undissolved Zr acts as a nucleation site during solidification and forms fine-equiaxed grains.[33] In contrast, the alloys in the AZ family (the most widely used type of commercial Mg alloys) containing Al and Zn are expected to be unsuitable for Mg battery anodes as Zn tends to migrate to the surface.

3. Conclusions

We performed a theoretical study of 34 dopants reported in the literature as beneficial to improve magnesium ductility to explore their potential use as anodes in magnesium batteries. We started by checking that the studied alloys at the doping level considered in this work (~2.08%) promote stacking fault defects, whose presence enhances magnesium ductility. Subsequently, we examined whether the dopants tend to segregate and form separate phases or prefer to remain in the alloy. We found that only 20 out of the 34 dopants, mostly rare-earth elements, are stable in the alloy. Finally, we investigated these 20 stable dopants and their propensity to migrate to the alloy's surface. We considered that those dopants that migrate to the surface could interfere with the electrochemical process
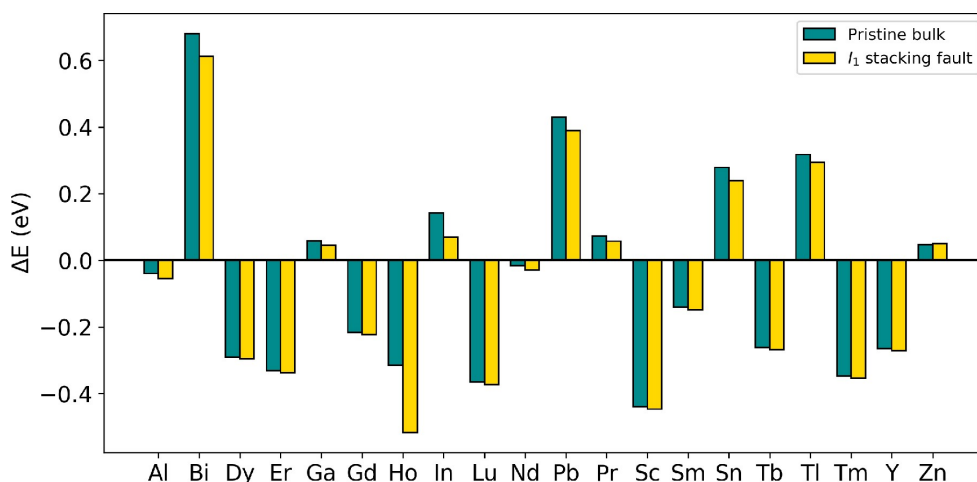

Figure 4. Relative energies of stable Mg alloys.

Batteries & Supercaps

Articles
doi.org/10.1002/batt.202000240

Chemistry Europe
European Chemical
Societies Publishing

(they could, for instance, produce passivation or degrade the electrolyte), and thus we disregarded them as useful dopants. Within this sequential analysis, we identified 12 potential favorable dopants: Al, Dy, Er, Gd, Ho, Lu, Nd, Sc, Sm, Tb, Tm and Y. Remarkably, the commercial alloy WE43 contains Y and Nd, both included in our shortlist of beneficial dopants, so we encourage experimental tests with this alloy.

Acknowledgement

Conflict of Interest

The authors declare no conflict of interest.

[1] R. Mohtadi, F. Mizuno, *Beilstein J. Nanotechnol.* **2014**, *5*, 1291–1311.
[2] T. S. Arthur, N. Singh, M. Matsui, *Electrochem. Commun.* **2012**, *16*, 103–106.
[3] N. Singh, T. S. Arthur, C. Ling, M. Matsui, F. Mizuno, *Chem. Commun.* **2013**, *49*, 149–151.
[4] F. Murgia, E. T. Weldekidan, L. Stievano, L. Monconduit, R. Berthelot, *Electrochem. Commun.* **2015**, *60*, 56–59.
[5] K. Periyapperuma, T. T. Tran, M. Purcell, M. Obrovac, *Electrochim. Acta* **2015**, *165*, 162–165.
[6] J. Niu, Z. Zhang, D. Aurbach, *Adv. Energy Mater.* **2020**, *10*, 2000697.
[7] D. Aurbach, Z. Lu, A. Schechter, Y. Gofer, H. Gizbar, R. Turgeman, Y. Cohen, M. Moshkovich, E. Levi, *Nature* **2000**, *407*, 724–727.
[8] O. Mizrahi, N. Amir, E. Pollak, O. Chusid, V. Marks, H. Gottlieb, L. Larush, E. Zinigrad, D. Aurbach, *J. Electrochem. Soc.* **2008**, *155*, A103.
[9] C. J. Barile, E. C. Barile, K. R. Zavadil, R. G. Nuzzo, A. A. Gewirth, *J. Phys. Chem. C* **2014**, *118*, 27623–27630.
[10] R. Mohtadi, M. Matsui, T. S. Arthur, S.-J. Hwang, *Angew. Chem.* **2012**, *124*, 9918–9921.
[11] T. Mandai, H. Somekawa, *Chem. Commun.* **2020**, *56*, 12122–12125.
[12] S. Sandlöbes, M. Friák, S. Korte-Kerzel, Z. Pei, J. Neugebauer, D. Raabe, *Sci. Rep.* **2017**, *7*, 1–8.
[13] S. Sandlöbes, M. Friák, S. Zaefferer, A. Dick, S. Yi, D. Letzig, Z. Pei, L.-F. Zhu, J. Neugebauer, D. Raabe, *Acta Mater.* **2012**, *60*, 3011–3021.
[14] H. Zhao, P. Bian, D. Ju, *J. Environ. Sci.* **2009**, *21*, S88–S91.
[15] N. Wang, R. Wang, C. Peng, Y. Feng, B. Chen, *Corros. Sci.* **2012**, *64*, 17–27.
[16] D. Schloffer, S. Bozorgi, P. Sherstnev, C. Lenardt, B. Gollas, *J. Power Sources* **2017**, *367*, 138–144.
[17] J. Zhang, Y. Dou, G. Liu, Z. Guo, *Comput. Mater. Sci.* **2013**, *79*, 564–569.
[18] Z. Pei, M. Friák, S. Sandlöbes, R. Nazarov, B. Svendsen, D. Raabe, J. Neugebauer, *New J. Phys.* **2015**, *17*, 093009.
[19] R. Mises, *Z. Angew. Math. Mech.* **1928**, *8*, 161–185.
[20] M. Yoo, *Metall. Trans. A* **1981**, *12*, 409–418.
[21] Z. Wu, W. Curtin, *Nature* **2015**, *526*, 62–67.
[22] G. Kresse, J. Furthmüller, *Phys. Rev. B* **1996**, *54*, 11169–11186.
[23] G. Kresse, J. Furthmüller, *Comput. Mater. Sci.* **1996**, *6*, 15–50.
[24] J. P. Perdew, K. Burke, M. Ernzerhof, *Phys. Rev. Lett.* **1996**, *77*, 3865–3868.
[25] P. Blöchl, *Phys. Rev. B* **1994**, *50*, 17953–17979.
[26] R. Tran, Z. Xu, B. Radhakrishnan, D. Winston, W. Sun, K. A. Persson, S. P. Ong, *Sci. Data* **2016**, *3*, 1–13.
[27] S. P. Ong, W. D. Richards, A. Jain, G. Hautier, M. Kocher, S. Cholia, D. Gunter, V. L. Chevrier, K. A. Persson, G. Ceder, *Comput. Mater. Sci.* **2013**, *68*, 314–319.
[28] Y. Wang, L.-Q. Chen, Z.-K. Liu, S. Mathaudhu, *Scr. Mater.* **2010**, *62*, 646–649.
[29] M. Qian, D. StJohn, M. Frost, *Scr. Mater.* **2002**, *46*, 649–654.
[30] J. Murray, *Bull. Alloy Phase Diagrams* **1986**, *7*, 245–248.
[31] J. Schaum, H. Burnett, *J. Res. Natl. Bur. Stand.* **1952**, *49*, 155.
[32] R. Agarwal, J. J. Lee, H. L. Lukas, F. Sommer, *Zeitschrift für Metallkunde* **1995**, *86*, 103–108.
[33] Y. Ding, C. Wen, P. Hodgson, Y. Li, *J. Mater. Chem. B* **2014**, *2*, 1912–1933.

Paper II
Thermodynamic Investigation of Phase Transformation in Sn Anode for Magnesium Batteries
Smobin Vincent, David Kleiven, Juan Maria García Lastra and Jin Hyun Chang,
APL Materials, 10, 071104 (2022)

Thermodynamic investigation of phase transformation in Sn anode for magnesium batteries

Smobin Vincent, David Kleiven, Juan Maria Garcia Lastra, et al.

View Online   Export Citation   CrossMark

ARTICLES YOU MAY BE INTERESTED IN

Thermodynamic investigation of phase transformation in Sn anode for magnesium batteries

View Online　　Export Citation　　CrossMark

Smobin Vincent,[1] (ID) David Kleiven,[2] Juan Maria Garcia Lastra,[1] (ID) and Jin Hyun Chang[1,a] (ID)

AFFILIATIONS

[1] Department of Energy Conversion and Storage, Technical University of Denmark, DK-2800 Kgs. Lyngby, Denmark
[2] Department of Physics, Norwegian University of Science and Technology (NTNU), Trondheim NO-7491, Norway

Note: This paper is part of the Special Topic on Abundant and Non-toxic Materials for Batteries.
[a] Author to whom correspondence should be addressed: jchang@dtu.dk

ABSTRACT

Metallic Mg anodes are incompatible with conventional electrolytes, such as $Mg(BF_4)_2$ or $Mg(ClO_4)_2$, due to the formation of a passivation layer that blocks the transport of Mg ions, thus limiting the selection of electrolytes and cathodes. Alloying anode materials for Mg batteries, such as Sn and its intermetallics, have recently been proposed as a new class of anode materials for Mg-ion batteries to address the issues of incompatibility with the conventional electrolytes. However, the large changes in the volume of the Mg–Sn alloy during cycling lead to poor Coulombic efficiency and rapid capacity degradation. The underlying reasons for how the structural changes hamper electrochemical performance remain unclear. In this work, we perform a theoretical study of the Mg–Sn alloys to have a deeper insight into the alloying process and the phase transformation in the Sn anode. This work is the first in-depth computational study that combines density functional theory and cluster expansion to investigate the phase transition process in the Mg–Sn system that includes Mg_2Sn, α-Sn, and β-Sn structures. We considered three possible routes for the transformation pathway from Mg_2Sn to β-Sn: $Mg_2Sn \rightarrow \alpha$-Sn $\rightarrow \beta$-Sn, $Mg_2Sn \rightarrow \beta$-Sn, and $Mg_2Sn \rightarrow$ amorphous phase $\rightarrow \beta$-Sn. Our study shows that the transformation of Sn between its α- and β-phases hinders the alloying process. This hindrance, together with the amorphization of the alloy, is revealed to be the key factor to understand the poor electrochemical performance of the Mg–Sn alloy.

I. INTRODUCTION

Li-ion batteries (LIBs) are currently the dominant energy storage technology used in electric vehicles and portable electronic devices. LIBs still face challenges in meeting future energy storage requirements due to limited mineral resources (e.g., Li and Co) that could lead to an increase in prices and geopolitical tensions.[1–4] As a result, next-generation batteries based on naturally abundant materials are in demand, driving current research toward alternative battery chemistries. Rechargeable magnesium batteries (RMBs) are one of the promising post-Li-ion batteries. Mg is abundant in nature and safe for the environment. The divalent Mg^{2+} cations give an attractive theoretical volumetric energy density of 3833 mA h/ml,[5] which is around two times that of Li. Metallic Mg can be used as an anode for RMBs since it does not suffer from the dendrite

formation[6–8] problem that affects the usage of metallic Li anodes in lithium batteries.

The metallic Mg anode suffers from two major limitations. The first issue is the incompatibility of the metallic Mg anode with conventional electrolytes, such as $Mg(BF_4)_2$ or $Mg(ClO_4)_2$; a passivation layer that forms at the electrode–electrolyte interface blocks the transport of Mg ions, preventing reversible plating and stripping from taking place.[9,10] The passivating layer consists of insoluble magnesium salts/halides formed as a reaction product of metal Mg and anions, such as ClO_4 and BF_4,[11] which got deposited on the Mg anode surface. The formation of the Mg-ion-blocking passivating layers can be prevented by using electrolytes with tetrahydrofuran (THF) and Grignard Mg salts, although they can only be operated within a narrow electrochemical window,[10,12,13] limiting the use of many high-voltage cathode materials. The second limitation of the

Mg anode is the brittleness of the Mg metal, which makes it difficult to be drawn into thin foils to be used as an anode in battery applications. Lightly doped Mg alloys can increase the ductility, but care should be given to ensure that the added dopants do not adversely affect the electrochemical properties.[14]

The alloying anode materials for Mg batteries, such as Sn,[15] In,[16] Pb,[17] Bi,[18] and their intermetallics, have recently been proposed as a new class of anode materials for Mg-ion batteries to address the issues of incompatibility with the conventional electrolytes. These alloying anodes are shown to be compatible with a wide range of conventional electrolytes and are less susceptible to the passivation layer formation.[15,19,20] Among the alloying anodes, Sn appears to be a promising anode because of its high gravimetric capacity, ductility, and low intercalation voltage.[15] A theoretical study by Wang *et al.*[21] indicated that Sn has a relatively low migration barrier for Mg^{2+} ions, making it a competitive anode for RMBs.

Sn exists in two allotropic forms: α- and β-Sn. The ground-state structure of Sn is a face-centered cubic (fcc) with a diamond crystal structure known as a α-Sn phase, which is a zero-gap semiconductor.[22] At a transition temperature of 13 °C, α-Sn transforms into the β-Sn phase, a body-centered tetragonal (bct) metal.[23] Most experimental studies of Sn are based on the β-Sn phase as it is the stable phase at room temperature. The β-Sn structure becomes Mg_2Sn with the fcc structure upon magnesiation.[15]

Significant volume change during charge and discharge is a known issue of Sn.[11,24] The structural distortion due to the volume change leads to poor Coulombic efficiency and rapid capacity degradation.[25] The underlying reasons for how the structural changes hamper electrochemical performance remain unclear. Singh *et al.*[15] indicated that amorphization, accompanied by the structural transformation, hinders a complete extraction of Mg^{2+} from Mg_2Sn, which leads to poor Coulombic efficiency and fast capacity fade. The first step of improving the performance of the Sn anode is to gain an in-depth understanding of the phase transformation process during charge and discharge, which can be used for designing future anode materials.

The aim of this study is to investigate the phase transformation from pure Sn (bct) to Mg_2Sn (fcc) on magnesiation. While the β-Sn and Mg_2Sn are the only two known crystalline phases during the cycling of the Sn anode, no detailed information is available for the transformation from bct to fcc structures. This study investigates the relative thermodynamic stability of the bct to fcc phase at intermediate magnesiation levels. The cluster expansion (CE) method coupled with first-principle density functional theory (DFT) calculations have been proven to predict the structures formed during the battery charging and discharging.[26–28] Previous CE study on Mg–Sn alloys only considers hcp and fcc structures[29] while overlooking the bct structure, which is known to be the most stable phase for pure Sn.[23] The present work is the first theoretical study that includes the missing bct structure in the phase analysis. The hcp phase has not been considered in this study as it is not present during the charge–discharge process of the RMBs. Two CE models are developed to determine the most thermodynamically stable phase at different Mg concentration levels by comparing the formation energies of bct and fcc structures. In addition, we simulated the voltage profile using Monte Carlo (MC) simulations to gain more insights into how the thermodynamic stability of the materials is related to their performance.

II. METHOD

First-principles calculations based on DFT were employed to calculate the total energies of all structures. DFT calculation results are used to train CE models, and all of the calculations were performed using the Vienna *Ab initio* Simulation Package (VASP).[30,31] The Perdew–Burke–Ernzerhof (PBE) parameterized generalized gradient approximation (GGA) functional was employed to describe the exchange and correlation effects, and the projector augmented wave (PAW) method was used to account for the core–valence interactions.[32,33] A plane-wave basis set with a cut-off energy of 520 eV is used for the calculations. The Brillouin zone is integrated with the k-point mesh generated using the Monkhorst–Pack scheme with a k-point density of 4 per Å^{-1}.[34] The convergence threshold for electronic degrees of freedom was 10^{-6} eV, and the interatomic forces were set to 10^{-2} eV Å^{-1} for the structural relaxation.

We developed two separate CE models for α-Sn and β-Sn systems, where both of them are trained using corresponding DFT calculations. For simplicity, we refer to α-Sn and β-Sn systems as fcc and bct structures, respectively, based on their parent lattice structures. The energies from the first-principles calculations were then used to build the CE model to explore the configurational space more effectively. The CLuster Expansion in Atomic Simulation Environment (CLEASE) package was used to generate training structures for DFT calculations and to construct the CE model by fitting the effective cluster interactions (ECIs).[27] The training structures were generated systematically using different generation schemes provided in the CLEASE package. The first set of structures was generated using a random generation method. The subsequent structures are generated to ensure that energetically stable structures are included in the training set while the configurational space is sufficiently explored. Two generation schemes are employed for this work: a probe structure[35,36] scheme was used to generate structures that differ the most from the existing training set in the database and the ground-state structure generation scheme based on simulated annealing was used to include low-energy structures.[37]

A template lattice structure describing the substitutional disorder is needed to construct a CE model. A structure with a space group 216 [shown in Fig. 1(a)] is used to represent fcc structures (α-Sn and Mg_2Sn) as it is the common subgroup with the highest symmetry for the space groups of Mg_2Sn (space group 225) and Sn (space group 227). The structure becomes α-Sn when 4b and 4c Wyckoff positions are occupied by Sn and vacancy, respectively. The Mg_2Sn structure can be realized using the template when 4b and 4c positions are occupied by Mg. The charging procedure can be mimicked by letting the 4b sites be occupied by either Mg or Sn, while the 4c sites are occupied by either Mg or vacancy. A total of 200 structures are generated for the fcc structures while applying the above site constraints. The 200 structures consist of structures with a conventional cell (1 × 1 × 1 cell consisting of 12 atoms), 2 × 1 × 1 cell (24 atoms), and 2 × 2 × 1 cell (48 atoms).

A template structure with space group 141 was used to construct the CE model for bct structures [shown in Fig. 1(b)] as the β-Sn phase has a bct crystal structure with the space group 141. There is no imposed constraint for the occupation of the lattice sites, which means any of the lattice sites can be occupied by either Mg or Sn. It is known from experiments that the solubility of magnesium in
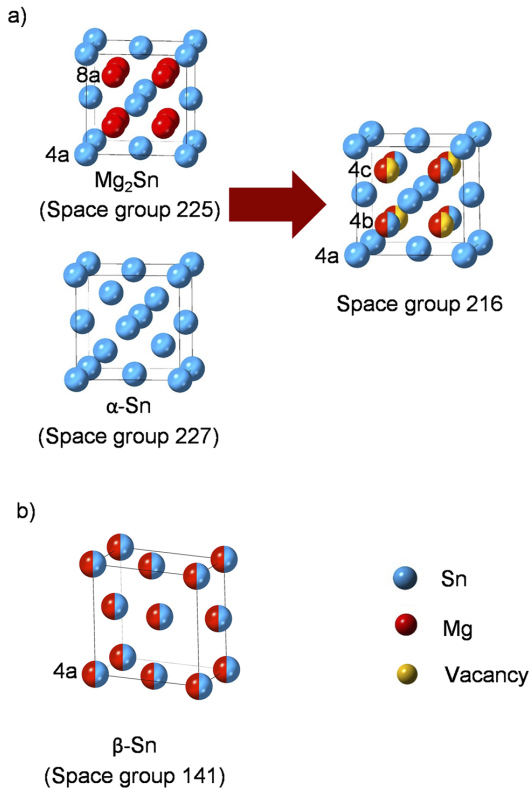
FIG. 1. (a) Structures of Sn and Mg_2Sn, which can be represented using a common template with space group 216. (b) Template with space group 141 for bct structures.

bct Sn is very low.[38,39] Therefore, we limited the magnesiation concentration in the bct structure to be up to 12.5% Mg to allow for a thorough sampling at low Mg concentration. We generated 170 bct structures with the Mg concentration below 12.5% to train the CE model. The CE models for bct and fcc structures were constructed using the maximum cut-off radii of 9, 9, and 7 Å for the two-body, three-body, and four-body clusters, respectively. Two regularization schemes, ℓ_1 and ℓ_2 types, are compared for its predictive power, which is evaluated using leave-one-out cross-validation (LOOCV) score.

One technical issue for constructing an accurate CE model is the large lattice distortion after the structure relaxation, which originates from the presence of vacancies or large mismatch in atomic radii of elements that occupy the lattice. The lattice distortions introduce "noise" in the CE model, which assumes an ideal lattice structure. One strategy to alleviate the issue of lowered accuracy is to eliminate the heavily distorted structures.[29,40,41] The lattice

distortion can be quantitatively measured using normalized mean square displacement (NMSD), which is described as[40]

$$\text{NMSD} = \frac{\text{MSD}}{V^{\frac{2}{3}}}, \tag{1}$$

where V is the volume of the structure and MSD is the mean square displacement calculated using

$$\text{MSD} = \frac{\sum_{\text{atom}}\sum_{X=x,y,z}(X[f] - X[i])^2}{N_{\text{atom}}}. \tag{2}$$

$X[f]$ and $X[i]$ are Cartesian coordinates of the final relaxed structure and initial unrelaxed structure, respectively, and N_{atom} is the total number of atoms in the structure. The structures with a high value of NMSD (i.e., heavily distorted structures) are removed from the training set to construct a CE model without much distortion noise.

Monte Carlo (MC) simulations were performed using the constructed CE model to investigate the relative stability of fcc and bct structures and to obtain the voltage profile.[28,42] We used canonical MC at various fixed concentrations for the phase stability analysis. The lowest energy structure for each concentration was obtained using a simulated annealing technique. The starting temperature of the MC simulations was set to 10^{10} K, which was gradually lowered to 2 K. A $5 \times 5 \times 15$ supercell consisting of 1200 atoms was used for the fcc structures, while a $6 \times 6 \times 9$ supercell consisting of 1296 atoms was used for bct structures.

The relative stability of the phases was investigated using convex-hull analysis. The formation energy for the construction of convex hull is calculated using the following equation:

$$E_f = E_{Mg_xSn} - X_{Mg}E_{Mg} - X_{Sn}E_{\alpha-Sn}, \tag{3}$$

where E_{Mg_xSn} (0 < x < 2) is the total energy of the structure and X_{Mg} and X_{Sn} are the concentration of Mg and Sn in the structure, respectively. E_{Mg} and $E_{\alpha-Sn}$ are the energy per atom of pure Mg (hcp) and α-Sn, respectively.

The open-circuit voltage (OCV) profile was obtained using semi-grand canonical Monte Carlo (sgcMC) simulations. The sgcMC has the advantage of controlling the concentration of the system by imposing fixed chemical potential. Each trial move in sgcMC simulation consists of selecting a random site and substituting the site with a different element, which makes the concentrations of species in the cell to fluctuate from one point to another. The chosen value of chemical potential controls the average concentration of species. The sgcMC simulations presented in this work require two chemical potential values since there are two binary sub-lattices in the simulation cell that consists of Mg–Sn and Mg–vacancy. Throughout this work, the two sub-lattices were kept in internal equilibrium by constraining the chemical potential of Mg to be the same on both of the two sub-lattices. This constraint allows us to control the Mg concentration by varying one chemical potential. This chemical potential can be directly used to calculate the OCV of the half-cell consisting of Mg and Sn electrodes (the Sn electrode is the material under study, which is magnesiated up to Mg_2Sn). The OCV is calculated using the following formula:

$$\text{OCV} = -\frac{\mu_{Mg}^{Mg_xSn} - \mu_{Mg}}{e}. \tag{4}$$

Here, $\mu_{\mathrm{Mg}}^{\mathrm{Mg_x Sn}}$ ($0 < x < 2$) is the chemical potential in eV per Mg atom in $\mathrm{Mg_x Sn}$ (this is the chemical potential obtained from sgcMC), μ_{Mg} is the energy per atom of the pure Mg in the hcp crystal structure calculated as -1.5095 eV, and e is the electric charge, which is 2 for $\mathrm{Mg^{2+}}$ ion. The same settings were used for the simulated annealing for the sgcMC simulations, except for the use of a $10 \times 10 \times 10$ supercell consisting of 12 000 atoms for simulating fcc structures. The large supercell was used to allow the system to explore very low magnesium concentrations as a dip in voltage is observed in the experimental voltage profile at low magnesium concentrations.[15]

III. RESULTS AND DISCUSSION

A. Cluster expansion

As the first step of constructing the CE model, the relaxed structures from the DFT simulations are examined to determine their NMSDs to quantitatively investigate their degree of distortion. The lattice distortion of relaxed structures in the considered magnesium range and their distributions are shown in Fig. 2. The Mg concentrations ranging from 0% to ~67% and from 0% to 12.5% are considered for fcc and bct structures, respectively. It is noted that lattice distortion is low in the vicinity of known stable concentrations (α-Sn and $\mathrm{Mg_2 Sn}$ for fcc structures and β-Sn for bct structures). The heavily distorted structures tend to be present in the concentration ranges that deviate significantly from the known stable structures (i.e., α-Sn, β-Sn and $\mathrm{Mg_2 Sn}$). The inclusion of these heavily distorted structures in the training set has been shown to have an adverse effect on the predictive power of the CE model.[29,40] In particular, Nguyen et al.[40] demonstrated that the accuracy of the CE model improved when it is trained with structures with the NMSD value of less than 0.1%.[40] Of the 200 fcc and 170 bct structures, 106 fcc and 71 bct structures had the NMSD values below 0.1%.

The effect of filtering out the distorted structures is verified by comparing the performances of the CE models constructed with and without the distorted structures. The performance is measured using the LOOCV score, and the NMSD value of 0.1% is used as a threshold to filter out the distorted structures. The LOOCV score of CE models with and without distorted structures is given in Table I. Two commonly used regularization schemes, ℓ_1- and ℓ_2-regularized fits, are used for obtaining the LOOCV scores. The LOOCV score of the fcc system improved substantially upon the removal of the highly distorted structures; the LOOCV score improved from 24.95 to 6.59 meV/atom for the ℓ_1-regularized fit and from 25.89 to 5.89 meV/atom for the ℓ_2-regularized fit. The improved LOOCV scores agree well with the findings of Nguyen et al.[40] The difference in the LOOCV for ℓ_1- and ℓ_2-regularized fits is negligible, and they deliver similar MC simulation results and convex hull diagram. The key difference is in the number of ECIs used in the CE model. The ℓ_1-regularized fit yields a lower number of ECIs, leading to a reduced computational time for the subsequent MC simulations. Consequently, the CE model constructed using the ℓ_1-regularized fit was used for the subsequent MC simulations for the fcc system.

No significant improvement in the LOOCV is found for the bct system upon the removal of the distorted structures. Despite the lack of significant change in the LOOCV score, it is observed that the structures with high NMSD values relax into different space
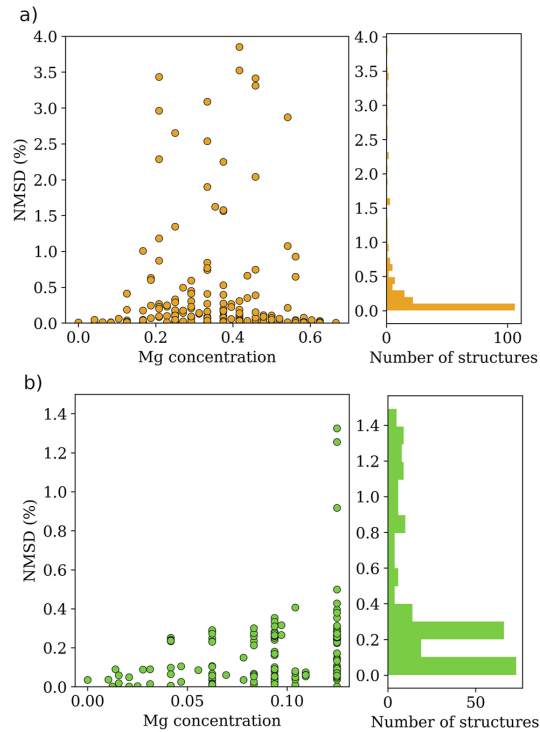

FIG. 2. Distortion of the structures based on the normalized mean square displacement (NMSD) values for the (a) fcc system and (b) bct system.

groups. The structures with high NMSD values are discarded from the training set since the relaxed structures no longer correspond to the original lattice model. In other words, we only used the structures in the training set that remain to have the same space group as we specified. It is evident from Table I that the LOOCV score with ℓ_1 regularization is significantly higher than those with ℓ_2 regularization. Hence, the ECIs based on ℓ_2-regularized fit is used for the MC simulation of the bct system.

TABLE I. LOOCV score for the CE models of the fcc and the bct structures before and after removing distorted structures. LOOCV scores with ℓ_1- and ℓ_2-regularized fits are given for all models.

|	All structures			Undistorted structures		
	No. structures	LOOCV (meV/atom)		No. structures	LOOCV (meV/atom)	
		ℓ_1	ℓ_2		ℓ_1	ℓ_2
fcc	200	24.95	25.89	106	6.59	5.89
bct	170	13.66	4.39	71	13.31	3.7

B. Convex-hull analysis

The stable structures at different levels of magnesiation are identified through convex-hull analysis. The convex-hull plot obtained from DFT calculations without distorted structures for bct and fcc structures are shown in Fig. 3(a), and the one from the canonical MC based on CE models trained with this DFT dataset is shown in Fig. 3(b). It can be seen from both convex-hull plots that α-Sn (fcc) is more stable than the β-Sn (bct), which agrees with experimental and theoretical studies that α-Sn is the stable phase at low temperatures (temperature below 13 °C).[23,43] Furthermore, the fcc structures are energetically more favorable for the entire magnesiation levels considered. The canonical MC simulation for bct structures predicts a new phase when the Mg concentration is around 11% [Fig. 3(b)]. However, the relative energy of this phase with respect to the fcc is high, which indicates that this phase will not form at low temperatures. Jain *et al.*[44] reported an Mg_9Sn_5 phase to be thermodynamically stable. This phase is not observed in our convex hull since we only considered the structures in space groups 225 and 141. We calculated the formation energy of this structure and observed that this structure falls on the hull line. However, this structure is reported as a high temperature and

pressure phase and will not form under normal operating conditions of batteries.[45]

The vibrational contributions should be added to the formation energies to compare the bct and fcc systems at temperatures higher than 0 K. As the phonon calculations using DFT are computationally expensive, we include the vibrational contribution from the study of Legrain and Manzhos[43] on α-Sn and β-Sn based on DFT and the harmonic approximation. They calculated the difference in vibrational contribution to energy between β-Sn and α-Sn at transition temperature to be 0.024 eV/atom. The difference in energy is subtracted from the energies of all the bct structures to include the vibrational contributions effectively. This approximation is valid since our training set consists only of low Mg concentration structures and stays in the original parent lattice after discarding the highly distorted structures.

The convex-hull plots after including the vibrational contributions to DFT and canonical MC results are shown in Figs. 3(c) and 3(d), respectively. The energies of α-Sn and β-Sn become almost the same upon the inclusion of the vibrational contribution corresponding to the transition temperature. The updated convex-hull plots show that Sn and Mg_2Sn are the two stable phases upon
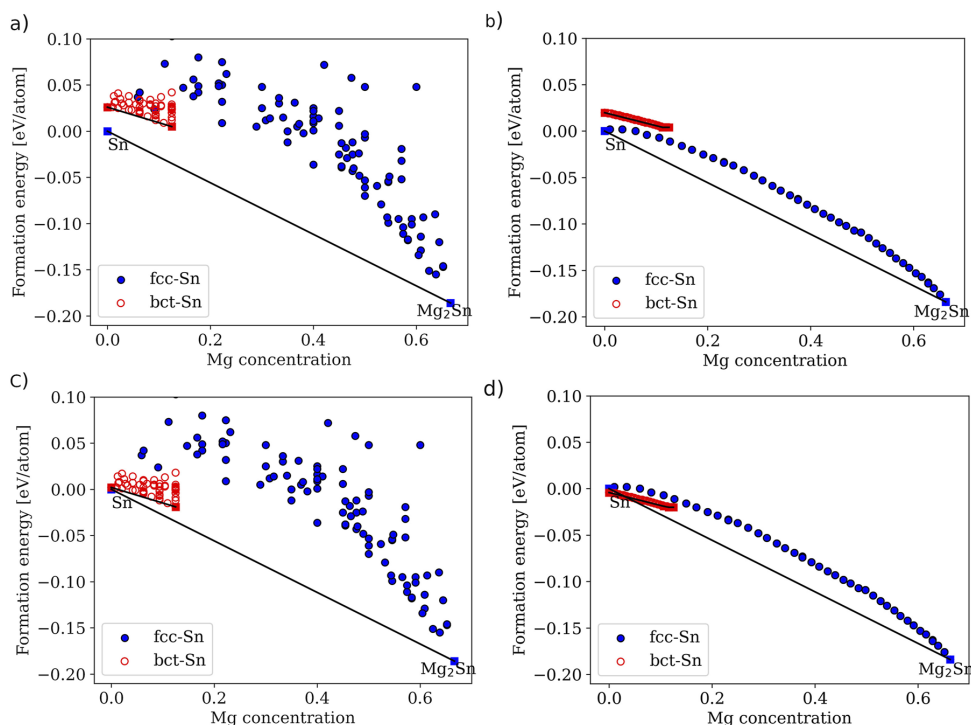

FIG. 3. Convex hull from (a) DFT calculations, (b) canonical MC simulations, and (c) DFT calculations with 0.024 eV/atom subtracted from the energy per atom of bct structures to include the vibrational contribution and (d) canonical MC based on the CE model trained with vibrational contribution added DFT dataset.

alloying Sn with Mg. Furthermore, it can be seen from the convex-hull plots that no other stable intermediate states are present during the charging of the Sn electrode to Mg_2Sn. The energies of fcc and bct structures overlap slightly only when the Mg concentration is very low, and the fcc structures become more stable as the Mg concentration is increased, indicating that bct structures are only stable when the Mg concentration is negligible. The results indicate that the nucleation of Mg_2Sn (fcc) will take place upon adding Mg to β-Sn. Legrain et al.[46] showed that low-concentration doping of Mg is unfavorable in both α-Sn and β-Sn, i.e., Mg prefers to segregate when doped in low concentration in these phases. Although doping of Mg is unfavorable in both phases, β-Sn exhibits lower defect formation energy relative to that of α-Sn, indicating that doping in the β-Sn phase is more stable. A similar trend can be observed in the present study as the system at low Mg concentrations is above the hull line [Figs. 3(b) and 3(d)], and the formation energies of low-concentration Mg in β-Sn are lower than those of α-Sn. We only considered the vibration contribution corresponding to the transition temperature 13 °C, but a similar approach can be used to study the phase transformation at higher temperatures. It is worth noting that the energy difference between the α-Sn and β-Sn without any vibrational contribution ($\Delta E_{\alpha-\beta}$) is 0.026 eV/atom in our study. This matches with the $\Delta E_{\alpha-\beta}$ value of 0.02–0.06 eV/atom reported in the previous DFT studies.[43,44] Legrain and Manzhos[43] pointed out that slight changes in the $\Delta E_{\alpha-\beta}$ can lead to a large difference in the transition temperature, and they obtained a $\Delta E_{\alpha-\beta}$ value of 0.04 eV/atom using the GGA functional. The $\Delta E_{\alpha-\beta}$ value of 0.026 eV/atom calculated in the present study is slightly lower than the value reported in their study. A larger $\Delta E_{\alpha-\beta}$ value will result in pushing the formation energies of β-Sn in Fig. 3 upward, making it less stable compared to the α-Sn.

C. Open-circuit voltage profile

The thermodynamic stability of the phases studied using the convex-hull plots is directly related to the voltage profile of batteries. The voltage profile obtained from the sgcMC simulation is shown in Fig. 4. The voltage plateau at 0.15 V obtained from the sgcMC matches the experimental value reported by Singh et al.[15] In their results, a slight dip in the voltage was observed at the beginning of magnesiation, which could originate from the kinetics of the bct to fcc transition. Since we only considered the thermodynamics of the phase transformation, the dip is not observed in the simulated voltage profile. The flat voltage profile predicted by the MC simulations indicates that the anode material is phase-separated during charging and discharging.

The magnesium solubility in Sn is low,[38,39] which could be a possible cause of the formation of two phases rather than a solid solution. The flat voltage profile is consistent with the convex-hull analysis, where no phases other than Sn and Mg_2Sn are observed. The single-phase β-Sn becomes phase-separated between β-Sn and Mg_2Sn during charge. At the end of charging, the system becomes a single-phase Mg_2Sn. Some studies suggest that an amorphous phase can form during the transformation from Mg_2Sn to β-Sn upon discharge.[15,47] Some of the highly distorted structures discarded for CE training had low formation energies that lie close to the convex hull, indicating that the system could transform into an intermediate phase (possibly an amorphous phase as indicated in previous
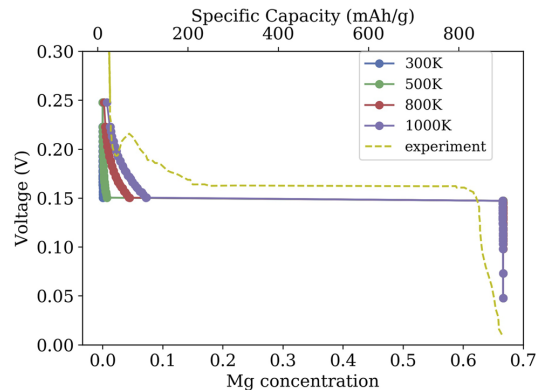
FIG. 4. Voltage profile obtained from the semi-grand canonical MC simulation for fcc structures. The dotted line is the experimental voltage profile from Ref. 15.

experimental studies) during the charging/discharging of the battery. A sufficiently slow discharge process can transform Mg_2Sn to β-Sn without losing its crystallinity. This transformation can happen via two possible routes. The first route is that Mg_2Sn transforms to α-Sn upon demagnesiation as they share a common parent lattice with space group 216 [Fig. 1(a)], followed by a transformation from α-Sn to β-Sn (i.e., $Mg_2Sn \rightarrow \alpha$-Sn $\rightarrow \beta$-Sn). However, it is not clear whether α-Sn to β-Sn transformation is massive or martensitic. Mitchell and Donnelly[48] reported that the α to β transformation is highly likely to be massive in nature due to the absence of a specific orientation relationship. Ojima et al.,[49] on the other hand, suggested that the transformation is mainly massive but also martensitic. The discrepancy indicates that a detailed study on the transformation from α-Sn to β-Sn is required. The second route is a direct transformation from the Mg_2Sn structure to β-Sn upon demagnesiation without an intermediate α-Sn (i.e., $Mg_2Sn \rightarrow \beta$-Sn). As shown in Figs. 3(c) and 3(d), the low-concentration Mg structures in the β-Sn phase has lower formation energies than those in the α-Sn phase, indicating the feasibility of taking the second route of bypassing the α-Sn phase entirely. We performed a DFT calculation to test the thermodynamic feasibility of the direct transformation from Mg_2Sn to β-Sn. A full structure relaxation calculation was carried out on a structure where all the Mg atoms in Mg_2Sn are removed from the cell, followed by a slight rattling of all the atoms. The structure relaxed to a tetragonal crystal structure, which is very similar to pristine β-Sn. The current work focuses on the thermodynamic stability of the phases present during the cycling of the Sn anode in RMBs. Further work on the kinetics of these phases to understand the transformation pathway is under way.

IV. CONCLUSION

We investigated the phase transformation of the Sn anode for RMBs using two DFT-based CE models to analyze the energetics of bct and fcc structures. This is the first time the energetics of fcc and bct phases are evaluated in the same framework to study

the phase transformation in Mg–Sn alloys. We performed canonical MC to obtain the convex-hull plots and sgcMC to obtain the open-circuit voltage profile. The phase stability analysis using the convex-hull plots demonstrates that bct structures are only stable at very low magnesium concentrations. The bct-Sn starts to transform into Mg_2Sn upon magnesiation. The voltage profile obtained from sgcMC simulations shows the voltage plateau that is consistent with the value reported in previous experiments. The flat voltage profile obtained from sgcMC is consistent with the phase stability analysis where the material remains phase-separated between β-Sn and Mg_2Sn during the charging and discharging of the battery. The highly distorted structures discarded in the CE model had low formation energies, suggesting that the material could transform into an amorphous phase during cycling. Our novel approach considers the three possible routes for the transformation from Mg_2Sn to β-Sn in this study. The first route is the transformation via an intermediate α-Sn phase ($Mg_2Sn \rightarrow \alpha$-Sn $\rightarrow \beta$-Sn). The second route is the direct transformation from Mg_2Sn to β-Sn ($Mg_2Sn \rightarrow \beta$-Sn). The third route is via an intermediate amorphous phase ($Mg_2Sn \rightarrow$ amorphous phase $\rightarrow \beta$-Sn). Further study is needed to understand the kinetic barrier and the phase transformation pathways.

ACKNOWLEDGMENTS

AUTHOR DECLARATIONS

Conflict of Interest

The authors have no conflicts to disclose.

Author Contributions

Smobin Vincent: Conceptualization (equal); Data curation (equal); Formal analysis (equal); Methodology (equal); Writing – original draft (equal); Writing – review & editing (equal). **David Kleiven:** Formal analysis (equal); Methodology (equal); Writing – original draft (equal). **Juan Maria Garcia Lastra:** Conceptualization (equal); Formal analysis (equal); Methodology (equal); Supervision (equal); Writing – original draft (equal); Writing – review & editing (equal). **Jin Hyun Chang:** Conceptualization (equal); Formal analysis (equal); Methodology (equal); Supervision (equal); Writing – original draft (equal); Writing – review & editing (equal).

DATA AVAILABILITY

The data that support the findings of this study are available from the corresponding author upon reasonable request.

REFERENCES

[1] D. Calisaya-Azpilcueta, S. Herrera-Leon, F. A. Lucay, and L. A. Cisternas, "Assessment of the supply chain under uncertainty: The case of lithium," Minerals **10**, 604 (2020).

[2] P. G. Schiavi, P. Altimari, R. Zanoni, and F. Pagnanelli, "Full recycling of spent lithium ion batteries with production of core-shell nanowires//exfoliated graphite asymmetric supercapacitor," J. Energy Chem. **58**, 336–344 (2021).

[3] B. Bustos-Gallardo, G. Bridge, and M. Prieto, "Harvesting lithium: Water, brine and the industrial dynamics of production in the Salar de Atacama," Geoforum **119**, 177–189 (2021).

[4] S. Kosai, U. Takata, and E. Yamasue, "Natural resource use of a traction lithium-ion battery production based on land disturbances through mining activities," J. Cleaner Prod. **280**, 124871 (2021).

[5] R. Shah, V. Mittal, E. Matsil, and A. Rosenkranz, "Magnesium-ion batteries for electric vehicles: Current trends and future perspectives," Adv. Mech. Eng. **13**, 16878140211003398 (2021).

[6] F. Bella, S. De Luca, L. Fagiolari, D. Versaci, J. Amici, C. Francia, and S. Bodoardo, "An overview on anodes for magnesium batteries: Challenges towards a promising storage solution for renewables," Nanomaterials **11**, 810 (2021).

[7] P. Saha, M. K. Datta, O. I. Velikokhatnyi, A. Manivannan, D. Alman, and P. N. Kumta, "Rechargeable magnesium battery: Current status and key challenges for the future," Prog. Mater. Sci. **66**, 1–86 (2014).

[8] T. Ichitsubo, T. Adachi, S. Yagi, and T. Doi, "Potential positive electrodes for high-voltage magnesium-ion batteries," J. Mater. Chem. **21**, 11764–11772 (2011).

[9] H. D. Yoo, S.-D. Han, I. L. Bolotin, G. M. Nolis, R. D. Bayliss, A. K. Burrell, J. T. Vaughey, and J. Cabana, "Degradation mechanisms of magnesium metal anodes in electrolytes based on $(CF_3SO_2)_2N^-$ at high current densities," Langmuir **33**, 9398–9406 (2017).

[10] D. Aurbach, Z. Lu, A. Schechter, Y. Gofer, H. Gizbar, R. Turgeman, Y. Cohen, M. Moshkovich, and E. Levi, "Prototype systems for rechargeable magnesium batteries," Nature **407**, 724–727 (2000).

[11] J. Niu, Z. Zhang, and D. Aurbach, "Alloy anode materials for rechargeable Mg ion batteries," Adv. Energy Mater. **10**, 2000697 (2020).

[12] Z. Ma, D. R. MacFarlane, and M. Kar, "Mg cathode materials and electrolytes for rechargeable Mg batteries: A review," Batteries Supercaps **2**, 115–127 (2019).

[13] T. D. Gregory, R. J. Hoffman, and R. C. Winterton, "Nonaqueous electrochemistry of magnesium: Applications to energy storage," J. Electrochem. Soc. **137**, 775 (1990).

[14] S. Vincent, J. H. Chang, and J. M. Garcia Lastra, "Computational design of ductile magnesium alloy anodes for magnesium batteries," Batteries Supercaps **4**, 522–528 (2021).

[15] N. Singh, T. S. Arthur, C. Ling, M. Matsui, and F. Mizuno, "A high energy-density tin anode for rechargeable magnesium-ion batteries," Chem. Commun. **49**, 149–151 (2013).

[16] F. Murgia, E. T. Weldekidan, L. Stievano, L. Monconduit, and R. Berthelot, "First investigation of indium-based electrode in Mg battery," Electrochem. Commun. **60**, 56–59 (2015).

[17] K. Periyapperuma, T. T. Tran, M. I. Purcell, and M. N. Obrovac, "The reversible magnesiation of Pb," Electrochim. Acta **165**, 162–165 (2015).

[18] A. Benmayza, M. Ramanathan, N. Singh, F. Mizuno, and J. Prakash, "Electrochemical and thermal studies of bismuth electrodes for magnesium-ion cells," J. Electrochem. Soc. **162**, A1630 (2015).

[19] T. S. Arthur, N. Singh, and M. Matsui, "Electrodeposited Bi, Sb and $Bi_{1-x}Sb_x$ alloys as anodes for Mg-ion batteries," Electrochem. Commun. **16**, 103–106 (2012).

[20] Y. NuLi, J. Yang, J. Wang, and Y. Li, "Electrochemical intercalation of Mg^{2+} in magnesium manganese silicate and its application as high-energy rechargeable magnesium battery cathode," J. Phys. Chem. C **113**, 12594–12597 (2009).

[21] Z. Wang, Q. Su, J. Shi, H. Deng, G. Q. Yin, J. Guan, M. P. Wu, Y. L. Zhou, H. L. Lou, and Y. Q. Fu, "Comparison of tetragonal and cubic tin as anode for Mg ion batteries," ACS Appl. Mater. Interfaces **6**, 6786–6789 (2014).

[22] S. Groves and W. Paul, "Band structure of gray tin," Phys. Rev. Lett. **11**, 194 (1963).

[23] G. A. Busch and R. Kebn, "Semiconducting properties of gray tin," Solid State Phys. **11**, 1–40 (1960).

[24]O. I. Malyi, T. L. Tan, and S. Manzhos, "In search of high performance anode materials for Mg batteries: Computational studies of Mg in Ge, Si, and Sn," J. Power Sources **233**, 341–345 (2013).

[25]D.-T. Nguyen, X. M. Tran, J. Kang, and S.-W. Song, "Magnesium storage performance and surface film formation behavior of tin anode material," ChemElectroChem **3**, 1813–1819 (2016).

[26]J. H. Chang, C. Baur, J.-M. Ateba Mba, D. Arčon, G. Mali, D. Alwast, R. J. Behm, M. Fichtner, T. Vegge, and J. M. Garcia Lastra, "Superoxide formation in Li_2VO_2F cathode material – A combined computational and experimental investigation of anionic redox activity," J. Mater. Chem. A **8**, 16551–16559 (2020).

[27]J. H. Chang, D. Kleiven, M. Melander, J. Akola, J. M. Garcia-Lastra, and T. Vegge, "CLEASE: A versatile and user-friendly implementation of cluster expansion method," J. Phys.: Condens. Matter **31**, 325901 (2019).

[28]Y. S. Meng and M. E. Arroyo-de Dompablo, "First principles computational materials design for energy storage materials in lithium ion batteries," Energy Environ. Sci. **2**, 589–609 (2009).

[29]K. Wang, D. Cheng, C.-L. Fu, and B.-C. Zhou, "First-principles investigation of the phase stability and early stages of precipitation in Mg–Sn alloys," Phys. Rev. Mater. **4**, 013606 (2020).

[30]G. Kresse and J. Furthmüller, "Efficiency of ab-initio total energy calculations for metals and semiconductors using a plane-wave basis set," Comput. Mater. Sci. **6**, 15–50 (1996).

[31]G. Kresse and J. Furthmüller, "Efficient iterative schemes for *ab initio* total-energy calculations using a plane-wave basis set," Phys. Rev. B **54**, 11169–11186 (1996).

[32]J. P. Perdew, K. Burke, and M. Ernzerhof, "Generalized gradient approximation made simple," Phys. Rev. Lett. **77**, 3865–3868 (1996).

[33]P. E. Blöchl, "Projector augmented-wave method," Phys. Rev. B **50**, 17953–17979 (1994).

[34]H. J. Monkhorst and J. D. Pack, "Special points for Brillouin-zone integrations," Phys. Rev. B **13**, 5188 (1976).

[35]A. Seko, Y. Koyama, and I. Tanaka, "Cluster expansion method for multicomponent systems based on optimal selection of structures for density-functional theory calculations," Phys. Rev. B **80**, 165122 (2009).

[36]A. Seko and I. Tanaka, "Cluster expansion of multicomponent ionic systems with controlled accuracy: Importance of long-range interactions in heterovalent ionic systems," J. Phys.: Condens. Matter **26**, 115403 (2014).

[37]A. van de Walle and G. Ceder, "Automating first-principles phase diagram calculations," J. Phase Equilib. **23**, 348–359 (2002).

[38]A. A. Nayeb-Hashemi and J. B. Clark, "The Mg–Sn (magnesium–tin) system," Bull. Alloy Phase Diagrams **5**, 466–476 (1984).

[39]A. Nayak and W. Oelsen, "Quantitative thermal analysis of magnesium–tin alloys by calorimetric measurement for the determination of solidus and liquidus curves," Trans. Indian Inst. Met. **22**, 53–58 (1969).

[40]A. H. Nguyen, C. W. Rosenbrock, C. S. Reese, and G. L. Hart, "Robustness of the cluster expansion: Assessing the roles of relaxation and numerical error," Phys. Rev. B **96**, 014107 (2017).

[41]A. van de Walle, "Multicomponent multisublattice alloys, nonconfigurational entropy and other additions to the Alloy Theoretic Automated Toolkit," CALPHAD: Comput. Coupling Phase Diagrams Thermochem. **33**, 266–278 (2009).

[42]A. Van der Ven and G. Ceder, "Ordering in $Li_x(Ni_{0.5}Mn_{0.5})O_2$ and its relation to charge capacity and electrochemical behavior in rechargeable lithium batteries," Electrochem. Commun. **6**, 1045–1050 (2004).

[43]F. Legrain and S. Manzhos, "Understanding the difference in cohesive energies between alpha and beta tin in DFT calculations," AIP Adv. **6**, 045116 (2016).

[44]A. Jain, S. P. Ong, G. Hautier, W. Chen, W. D. Richards, S. Dacek, S. Cholia, D. Gunter, D. Skinner, G. Ceder, and K. A. Persson, "Commentary: The Materials Project: A materials genome approach to accelerating materials innovation," APL Mater. **1**, 011002 (2013).

[45]K.-J. Range, G. H. Grosch, and M. Andratschke, "Studies on AB_2-type intermetallic compounds. Part V[1]. The crystal structure of Mg_9Sn_5, a supposed high-pressure modification of Mg_2Sn," J. Alloys Compd. **244**, 170–174 (1996).

[46]F. Legrain, O. I. Malyi, C. Persson, and S. Manzhos, "Comparison of alpha and beta tin for lithium, sodium, and magnesium storage: An *ab initio* study including phonon contributions," J. Chem. Phys. **143**, 204701 (2015).

[47]D.-T. Nguyen and S.-W. Song, "Magnesium stannide as a high-capacity anode for magnesium-ion batteries," J. Power Sources **368**, 11–17 (2017).

[48]D. R. G. Mitchell and S. E. Donnelly, "A transmission electron microscopy study of the $\beta \to \alpha$-phase transformation in tin," Philos. Mag. A **63**, 747–755 (1991).

[49]K. Ojima, Y. Taneda, and A. Takasaki, "Direct observation of $\alpha \to \beta$ transformation in tin by transmission electron microscopy," Phys. Status Solidi A **139**, 139–144 (1993).

Paper III
Ab-initio Study of Charge Transport in Mg-S batteries
Smobin Vincent, Jin Hyun Chang, Pieremanuele Canepa and Juan Maria García Lastra
To be submitted

Ab-initio Study of Charge Transport in Mg-S Battery Cathode

Smobin Vincent,[†] Jin Hyun Chang,[†] Pieremanuele Canepa,[‡] and Juan Maria García Lastra[*,†]

†*Department of Energy Conversion and Storage, DTU Energy*

‡*Department of Materials Science and Engineering, National University of Singapore, 117575, Singapore*

E-mail: jmgla@dtu.dk

Abstract

Rechargeable Mg-S batteries are attractive as next-generation energy storage devices due to their high theoretical energy density and low cost. Charge transport within the redox end products, i.e., MgS and MgS_2, limits the performance of Mg-S batteries. However, the mechanisms of charge transport in MgS and MgS_2, are not presently understood. The present study uses first-principles calculations to evaluate the equilibrium conductivity associated with point defects in MgS and MgS_2, and their transport mechanisms. Doubly positive Mg interstitial and doubly negative Mg vacancy are identified as the prevalent defects in MgS. Despite having a high concentration, due to their high mobility, the contribution of these defects to conductivity is negligible. One of the dominant defects in MgS_2, single electron polaron, exhibits good mobility despite having low concentrations. Thus, increasing the concentration of single electron polaron is the way to enhance conductivity in MgS_2. The charge transport study at non-equilibrium conditions using ab-initio molecular dynamics revealed that two single electrons in MgS_2, preferred to merge into form a double electron polaro

1

Introduction

Rechargeable metal-sulfur batteries such as Li-S, Al-S, Mg-S, and Ca-S are receiving significant interest as potential next generation batteries due to their low cost, environmental sustainability and abundance of sulfur.[1–4] In addition, metal-sulfur batteries offer high theoretical energy densities owing to their use of metal as an anode and high-capacity sulfur as the cathode. Li-S ($2654\,\mathrm{W\,h\,kg^{-1}}$ and $2856\,\mathrm{W\,h\,L^{-1}}$) and Mg-S ($1684\,\mathrm{W\,h\,kg^{-1}}$ and $3286\,\mathrm{W\,h\,L^{-1}}$) have the highest energy densities among the most studied metal-sulfur batteries.[1,5]. Mg-S battery has the advantage over the Li counterpart; in addition to the abundance and lower cost,[1,6,7] the dendrite-free nature of Mg makes it a safer alternative,[8,9] attracting much attention as a next-generation battery. Mg-S batteries have the potential to become a cost-effective, sustainable and safe alternative to Li-ion and Li-S batteries.

Despite the promises of Mg-S batteries, it is not free of technical challenges that must be overcome before being used in practical applications. One of the major challenges is the poor cyclability of the sulfur cathode, where the magnesiation process upon discharge is not highly reversible. More specifically, Mg^{2+} ions migrate from the Mg anode to sulfur cathode during discharge, forming various high-order polysulfides (e.g., MgS_8, MgS_6, and MgS_4), which get further reduced to form the final discharge products, MgS and MgS_2.[10] The formation of these high-order polysulfide intermediates occur at a fast rate due to their high solubility in the electrolytes.[11] However, the further reactions to lower-order (poly)sulfides become slower as they start to precipitate on the sulfur cathode.[12] Furthermore, these low-order (poly)sulfides have exhibit low Mg^{2+}-ion diffusivity, leading to a large overpotential at the trailing end of the charging process, as well as limited reversibility to high-order polysulfides and sulfur during charge.[13] Thus, understanding the charge transport properties in MgS and MgS_2 is very important in designing an efficient Mg-S battery with long cycle life.

Presently, the charge transport mechanism in MgS and MgS_2 is not fully understood. Although few experimental and computational studies exist for MgS, the study of charge transport in MgS_2 is left unexplored. Most experimental studies on the charge transport in MgS have been performed at

temperatures above 900 K.[14,15] The conductivity at room temperature is more important for battery applications. Presumably, the lack of conductivity measurement of MgS around room temperature stems from the difficulties in determining its low conductivity due to its insulating nature. Several computational works also investigated the charge transport in MgS. Puntambekar et al. computed the activation energies for the diffusion of Mg^{2+} (2.6 eV) and S^{2-} (3.4 eV) ions in MgS using an empirical interionic potential model.[16] Using density functional theory (DFT), Chen et al. calculated the diffusion barrier of 1.2 eV for Mg^{2+} ions in MgS.[17] These studies mainly focused on the ionic transport, and only little effort was devoted to studying electronic transport. The present study aims to elucidate the charge transport mechanism in MgS and MgS_2 using first-principles DFT calculations at the hybrid functional level of theory. More precisely, we study the ionic and electronic conductivity arising from the migration of charged point defects and polaronic defects (electron and hole polarons), respectively. The formation energies and equilibrium concentration of several point defects and polarons are calculated to identify the dominant defects. Further, the diffusion barrier for the prevalent defects are evaluated using nudged elastic band (NEB) method. The calculated energy barrier is then used to estimate the maximum thickness of MgS and MgS_2 layers to achieve practical discharge rates. The transport mechanism under the non-equilibrium conditions during the battery operations, i.e., the injection or extraction of polarons and Mg^{2+} from the cathode, is also investigated using ab-initio molecular dynamics (AIMD).

Methodology

Computational details

All of the first-principle DFT calculations were performed using Vienna Ab initio Simulation Package (VASP).[18,19] The commonly used PBE functional[20] is known to severely underestimate the bandgaps of semiconductors and insulators, as well as not predicting the charge localization reliably (i.e., the charges are often delocalized).[21] Therefore, we used the screened hybrid functional of Heyd–Scuseria–Ernzerhof (HSE06)[22,23] for the calculation of formation energies and diffusion

3

barrier for the defects. The α value was set to 0.40 (i.e., incorporating 40 % exact exchange) to reproduce the bandgap values of GW-level calculations, which is known to be more accurate.[24] All of the calculations used a plane wave basis for the electronic wave functions with a cut-off energy of 520 eV, and the projector augmented wave (PAW) method was used to account for the core-valence interactions.[25] All calculations are spin polarized, and the atomic positions are relaxed until the forces acting on each atoms are less than 1×10^{-1} eV Å^{-1}. The convergence threshold for electronic self-consistent loop was is set to 1×10^{-6} eV Å^{-1}.

The calculations for the bandgap, dielectric constant and chemical potential are performed with primitive unit cells. For these systems, the Brillouin zone was sampled with a dense Γ-centered k-point mesh with a minimum k-point density of 4 per Å^{-1}. The defect and mobility calculations were carried out using a $2 \times 2 \times 2$ supercell of the conventional cell with single Γ-centered k-point.

Defect formation energy

The likelihood of the defect formation was evaluated using the formation energy, E_f, of a defect, X. The E_f of X in charge state, q, was calculated according to

$$E_f(X^q) = E(X^q) - E_0 - \sum n_i \mu_i + q \varepsilon_f + E_{\text{FNV}}. \tag{1}$$

E_0 and $E(X^q)$ and represent the total energy of the pristine cell and the computational cell containing a point defect in charge state q, respectively. n_i is the number of atoms of species, i, removed while creating the defect, X. The value of n_i becomes negative when a species is removed from the cell during the defect creation. μ_i denotes the chemical potential of species i, which is determined by the phases that are in thermodynamic equilibrium with the material under study at 0 K. ε_f is the equilibrium Fermi energy of electrons, and E_{FNV} is the Freysoldt-Neugebauer-Vanderwall (FNV) correction for charged systems.[26] The FNV correction requires a dielectric constant of the material under investigation, which is calculated using self-consistent response of the material to a finite electric field. The computed dielectric constant of MgS and MgS$_2$ are 10.4 and 11.2, respectively.

The Python Charge Defects Toolkit (PYCDT) package[27] was used to generate the input struc-

tures and VASP settings files for the point defect calculations. The input structures for the polaronic

defect calculations, on the other hand, were prepared manually by distorting the local surrounding

of the region where polaron localization is as it is often . To localize polarons in DFT calculations,

typically, it is necessary to prepare the structures by manually distorting the local surroundings of

the region where polaron localization is anticipated.

The concentration of defects, $c(X^q)$, was calculated using

$$c(X^q) = N \exp\left(\frac{-E_f}{k_B T}\right), \tag{2}$$

where N is the number of equivalent sites of the defects, k_B is the Boltzmann constant and T is the

temperature in kelvin. The mobility of defect, μ, was calculated using

$$\mu = \frac{\nu q a^2}{k_B T} \exp\left(\frac{-E_b}{k_B T}\right), \tag{3}$$

where ν is the attempt frequency of the hopping, a is the hopping distance and E_b is the diffu-

sion barrier. The attempt frequency, ν, was taken as $1 \times 10^{13}\,\mathrm{s}^{-1}$ for both S and Mg.[28] a is the

distance between the initial and final points of the defects taken from DFT. The diffusion barrier

is calculated using nudged elastic band (NEB)[29] method implemented in the atomic simulation

environment (ASE) package.[30]

Molecular dynamics

The dynamics of the low energy barrier defects were analyzed using AIMD simulations. The

dynamics of the defects in non-equilibrium conditions is evaluated using AIMD simulation. The

molecular dynamcis (MD) calculations were performed in a canonical ensemble (NVT) at 350 K,

which is maintained by Langevin thermostat as implemented in ASE. The MD simulations used

the same VASP settings as static DFT calculations for defect formation, except for the use of the

PBE functional to keep the computational cost of the MD calculations reasonable. The simulation

is run with a time step of 1 fs and equilibriated for a time period of 0.5 ps for all cases, unless it is explicitly mentioned otherwise.
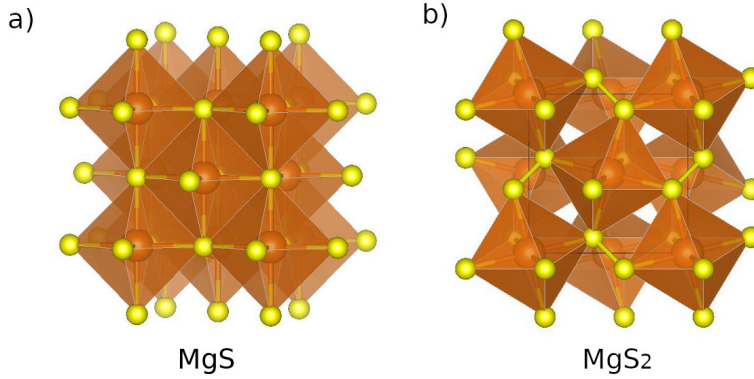
Results and discussion

Figure 1: The crystal structure of a) MgS and b) MgS_2. Brown and yellow correspond to Mg and S ions, respectively.

Crystal structure and bandgaps

The crystal structures of MgS and MgS_2 are illustrated in Fig. 1. The MgS exist as rocksalt crystal structure (spacegroup Fm-3m) in which the Mg^{2+} cations are octahedrally coordinated by S^{2-} anions. The most stable structure for MgS_2 is reported to be cubic pyrite structure (spacegroup Pa-3).[31] This is a modified rocksalt structure in which the S^{2-} anions of the rocksalt structure (MgS) is replaced by a S_2^{2-} dianions (S dimer). The calculated lattice constant value for MgS using HSE06 is 3.66 Å, which matches well with the experimental value of 3.67 Å.[32]

MgS and MgS_2 bandgaps were computed using DFT at three distinct levels of theory, namely G_0W_0, GW_0 and HSE06. The computed bandgaps are given in Table 1. It has been demonstrated that the GW_0 approach best describes the band gap of semiconductors and insulators.[24] Thus the α value of HSE06 (α=0.4) functional was calibrated to reproduce the GW_0 bandgaps, and results

in a bandgap of 4.49 eV and 4.34 eV for MgS and MgS_2, respectively. Both MgS and MgS_2 exhibits indirect bandgaps. Previous theoretical studies employing hybrid functional also reported an indirect band gap in the range of 4.0 eV to 4.8 eV for MgS. [33,34]

Table 1: Calculated bandgaps for MgS and MgS_2 with different levels of theory

	Bandgap (eV)	
	MgS	MgS_2
HSE06	4.49	4.34
GW_0	4.52	4.33
G_0W_0	4.29	3.88

Localization of polaron

Polarons are the localized charge of an electron or hole along with the induced polarization of the surrounding lattice in the crystal (i.e., lattice distortion in the vicinity of localized charge). In this work, we attempted to localize four types of polarons: single hole polaron (p^1), double hole polaron (p^2), single electron polaron (p^{1-}), and double electron polaron (p^{2-}).

In MgS, we were only able to obtain p^2. The sulfur atom in MgS has an oxidation state of -2. Removal of 2 electrons from the system results in a p^2 which changes the oxidation states of two sulfur atoms from -2 to -1. Thus the ions experience weaker electrostatic repulsion, resulting in the formation of a S-dimer. This can be seen in Fig. 2a that a S dimer is formed. The original $S-S$ interataomic distance of 3.65 Å is shortened to 2.3 Å in the presence of double-hole polaron. The double-hole polaron is localized only when the system is relaxed from a initial configuration in which one of the S-S bond is shortened. Without this initial distortion, it results in the delocalization of the polaron in the crystal. The delocalization energy (i.e., the difference in total energy between the structures with polaron delocalized and localized) for p^2 in MgS is calculated to be 0.21 eV. Previous study on MgO (which has a rocksalt structure similar to MgS) demonstrated that a single hole polaron could be localized on the Mg atom. [35] However, we could not localize the single hole polaron as well as the electron polarons in MgS.

For MgS_2, we could localize double-electron polaron and single-electron polaron. The addition

of an electron leads to localization of the p^{1-} on the sulfur dimer without any initial structural distortion. The presence of p^{1-} increases the $S-S$ bond distance to 2.57 Å from 2.05 Å. Fig. 2b shows the localization of p^{1-} on the S dimer. The p^{2-} formed by the addition of two electrons increases the $S-S$ distance significantly to 3.15 Å. This is illustrated in Fig. 2c. The formation of p^{1-} required a manual distortion of the initial structure. We observed that without this initial distortion, the two electrons were localize as two separate p^{1-} in the crystal structure.
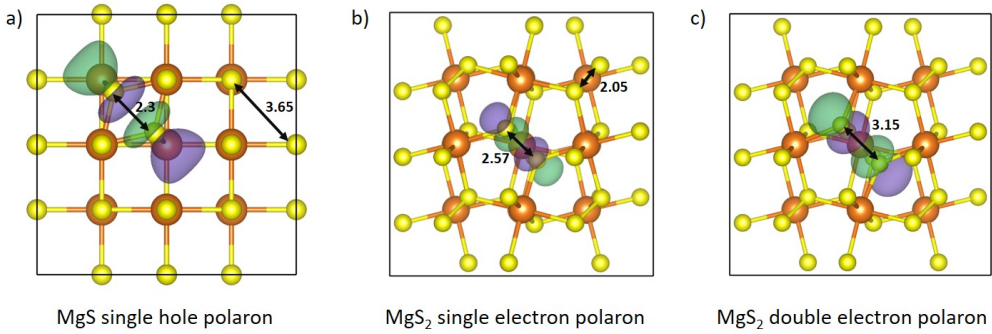

Figure 2: Frontier orbital wave function of a) single hole polaron localized in MgS b) single electron polaron localized in MgS_2, and c) double electron polaron localized in MgS_2. The numbers in the figure shows the S-S distance in Å

Defect formation energy

The formation energy of defects in MgS and MgS_2 for different chemical potential is shown in Fig. 3. The chemical potential varies with chemical environment of the system. i,e., the reservoir from which the chemical potential taken can be defined as Mg rich region (S poor region) or Mg poor region (S rich region). Based on OQMD database,[36] the phases that are in thermodynamic equilibrium with MgS at 0 K are $Mg_{149}S$, and MgS_2. While, the phases that are in thermodynamic equilibrium with MgS_2 are MgS and S. Thus, the limiting chemical potential value for calculating defects in MgS are defined by the $Mg_{149}S-MgS$ region (Mg rich) and $MgS-MgS_2$ region (Mg poor). Similarly for MgS_2, the limiting chemical potential is defined by the $MgS-MgS_2$ (Mg rich) and MgS_2-S (Mg poor) regions.

A total of 69 charged defects including magnesium vacancies (Vac_{Mg}), magnesium interstitial (Int_{Mg}), sulfur vacancies (Vac_S), sulfur interstitial (Int_S), hole polarons and electron polarons were considered. The charge of the defects are given as superscript in their notation. The slope of each line corresponds to charge state of that defect. We investigated 3 distinct interstitial positions for the Mg and S interstials in MgS. However, the interstitial defect with low formation energies are only shown in Fig. 3. The position of the equilibrium fermi level (E_f), which is indicated as vertical dashed line in Fig. 3 is determined using the charge neutrality condition, $\sum c_i q_i = 0$. The defects with low formation energy at equilibrium fermi level is considered as the dominant defect. The concentrations of the prevalent defects is given in Table 2.

Fig. 3a and Fig. 3b illustrate the formation energies of the defects in MgS for $Mg_{149}S-MgS$ region and $MgS-MgS_2$ region, respectively. In both regions, Vac_{Mg}^{2-} and Int_{Mg}^{2+} are the most favorable charged defects and they exhibit low defect formation energies, result in a high defect concentration of $9.78\,cm^{-3}$ The equilibrium fermi level is located at the intersection of these two defects, since the opposite charges of these two defects cancel each other out, resulting in the charge neutrality condition. In $MgS-MgS_2$ region, the defect with lowest formation energy is $VacS_0$. However, since the defect is neutral, it does not contribute to charge transport. Puntambekar et al. reported that Vac_{Mg}^{2-} is the predominant defect in MgS, which agrees with our observation.[16]

The defect formation energies of the defects in MgS_2 for MgS-MgS$_2$ and MgS-MgS regions are shown in Fig. 3c and Fig. 3d. Both regions showcase analogous defect formation energy diagram with $VacS_0$ as the lowest formation energy defect. However, as stated previously, they have no effect on charge transport due to the neutral charge. The p^{1-} is the next dominant defect in MgS_2 with a defect concentration of $3.48 \times 10^{-9}\,cm^{-3}$. Vac_{Mg}^{2-} have a slightly greater defect formation energy, which results in a rather lower defect concentration of $6.65 \times 10^{-15}\,cm^{-3}$. The interstitial defects in MgS_2 exhibits very high formation energy.
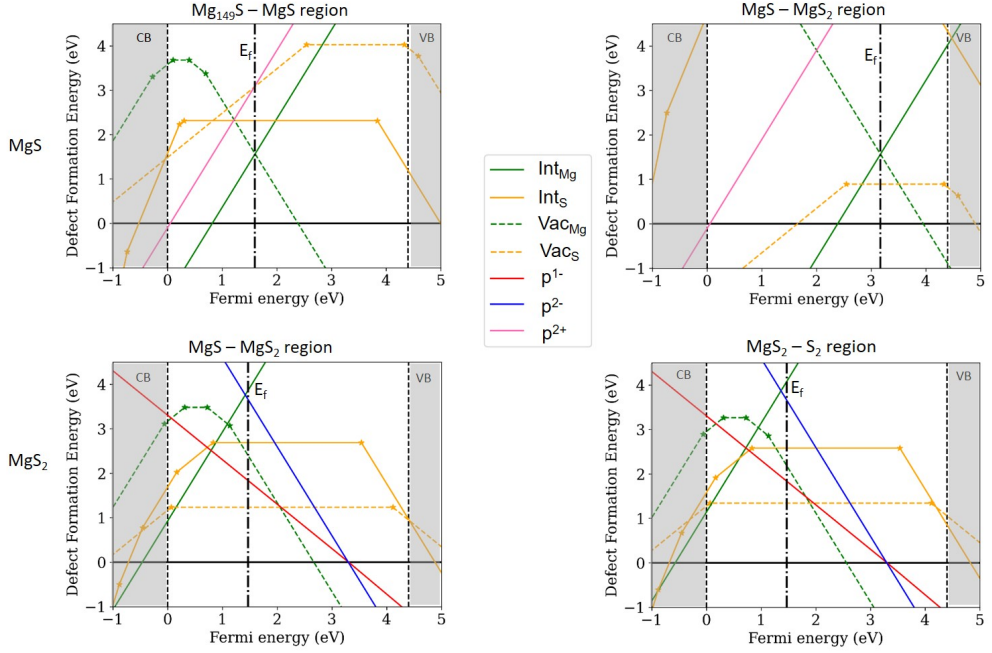
Figure 3: The defect formation energy for MgS and MgS_2. The equilibrium Fermi energy is shown with the dashed dotted line.

Mobility and conductivity

The energy barrier for the diffusion of most prevalent defects in MgS and MgS_2 were calculated using nudged elastic band method (NEB). Fig. 4a depicts the minimum energy path (MEP) for the predominant defects in MgS. The calculated mobilility and conductivity values are summarized in Table 2. Vac_{Mg}^{2-} exhibits very high migration barrier, which is consistent with experiment.[14]. Previous computational study using PBE functional estimated a migration barrier of 0.9 eV for the diffusion of Vac_{Mg}^{2-}.[17] The use of different functional could be the cause of variance in migration barrier compared to our study. The diffusion of Int_{Mg}^{2+} is also characterized by a high diffusion barrier of 1 eV. Despite having high defect concentrations, the low mobility of the Int_{Mg}^{2+} and Vac_{Mg}^{2-} results in poor conductivity.

The MEP for the dominant defects in MgS_2 is shown in Fig. 4b. Analogous to MgS, the Vac_{Mg}^{2-} migration barrier in MgS_2 is also very high. The single electron polaron (p^{1-}) exhibit low diffusion
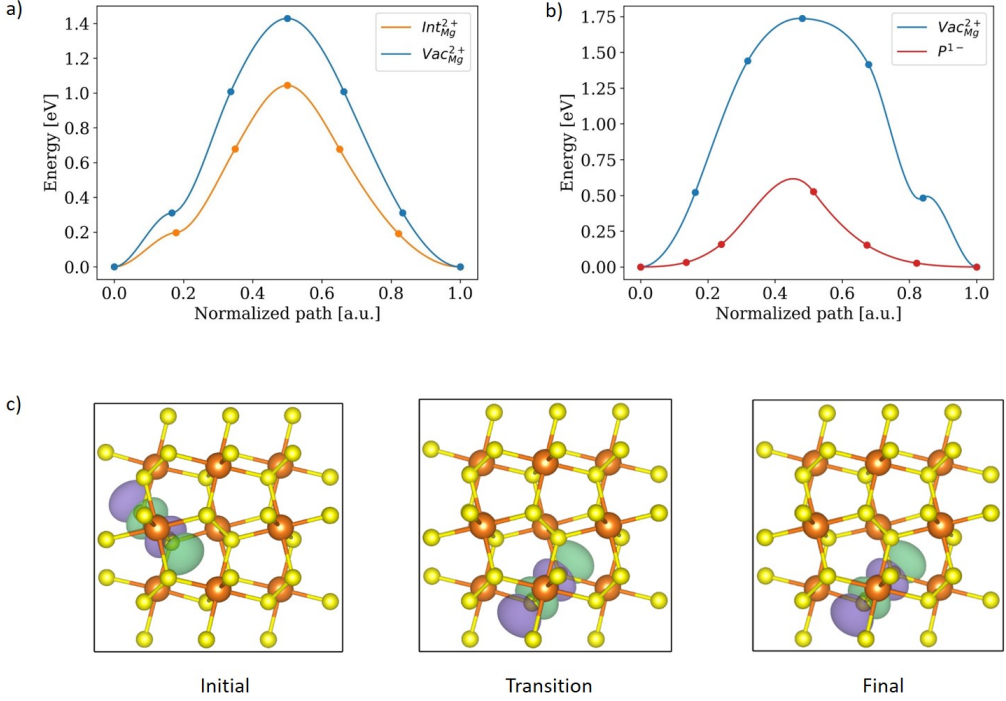
Figure 4: The energy barrier for the prevalent defects in a) MgS, and b) MgS$_2$. Frontier orbital wave function of initial, transition, and final images of c) single hole polaron in MgS d) double electron polaron in MgS$_2$

barrier. The activation energy for the diffusion of p^{1-} is 0.53 eV. In contrast to the hole polaron in MgS, the electron polarons in MgS$_2$ remained localized during migration. This is illustrated in Fig. 4c. The relatively low energy barrier of p^{1-} leads to a decent mobility. However, the less concentration of these defect results in negligible conductivity.

Molecular Dynamics

So far, we have analysed the transport mechanism based on the intrinsic defects formed at equilibrium. However, during the practical battery operation the scenario is different, being the cathode material out of equilibrium. During the charging of battery, electrons move from the external circuit to the cathode. Simultaneously, Mg ions from the electrolyte join the cathode. We employed

Table 2: Defect concentration, energy barrier, mobility and conductivity for the most prevalent defects in MgS and MgS$_2$.

System	Defects	Defect concentration [cm^{-3}]	Energy barrier [eV]	Mobility cm^2/(Vs)	Conductivity [S cm^{-1}]
MgS	Vac$_{Mg}^{2-}$	9.78	1.42	1.38×10^{-24}	2.71×10^{-23}
	Int$_{Mg}^{2+}$	9.78	1.01	8.35×10^{-18}	1.63×10^{-16}
MgS$_2$	Vac$_{Mg}^{2-}$	6.651×10^{-15}	1.73	1.18×10^{-29}	1.58×10^{-43}
	p^{1-}	3.48×10^{-9}	0.53	1.06×10^{-9}	3.69×10^{-18}

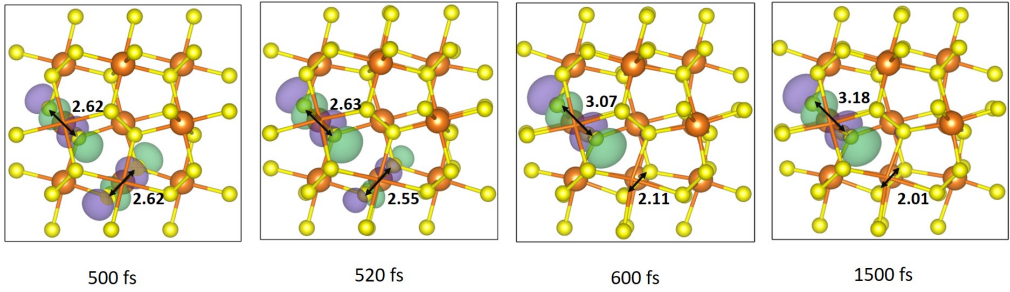different AIMD setups to comprehend the system's dynamics in such a scenario.

Figure 5: Snapshot from MD of electron polarons in bulk MgS$_2$

The Mg^{2+} ion from the electrolyte need two electrons from external circuit to compensate the charge. Our initial AIMD setup aimed to determine whether electrons entering from the external circuit prefer to exist as two single electron polarons or as a double electron polaron. The system was initialized with two single-electron polarons localized in the bulk crystal structure. The size of the bulk supercell is $2 \times 2 \times 2$ of the conventional unit cell with 96 atoms. The snapshot from the AIMD simulation after equilibration is shown in Fig. 5. During the equilibration, the S-dimers in which the polarons were localized kept fixed. From the Fig. 5, it is clear that initially the electrons exist as separated p^{1-}. Then in the subsequent steps they merge to form p^{2-}. Consequently, the $S-S$ distance of one S-S dimer shorten while the $S-S$ distance of the other dimer increases. This is consistent with our observation in the MEP for the p^{2-}. So, we anticipate that the electrons approaching the cathode from the external circuit will readily combine and form p^{2-}. For subsequent simulations, we therefore assumed the electrons entering from the external circuit to be p^{2-}.
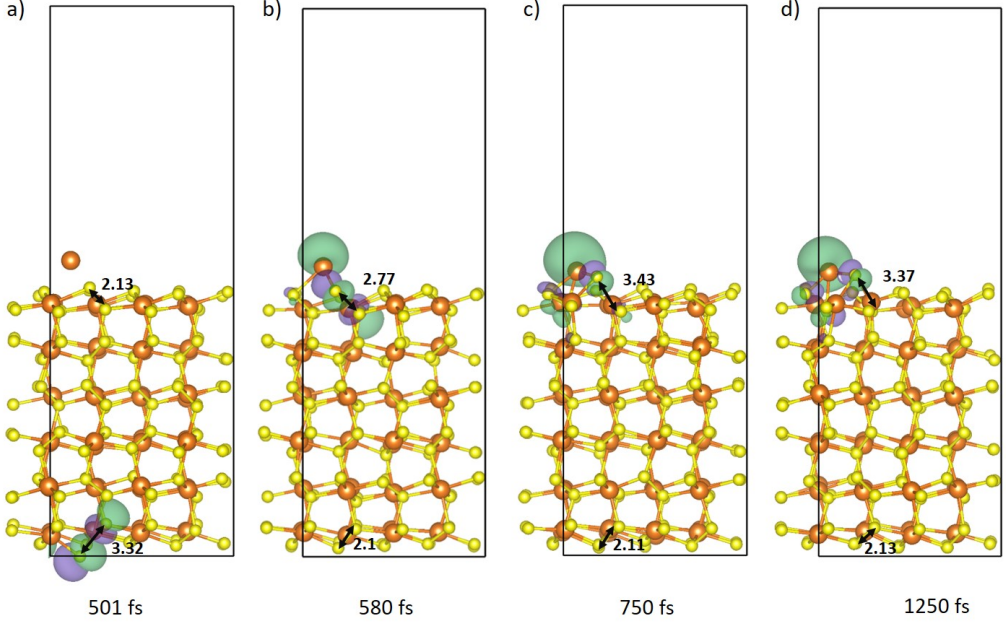
12

Figure 6: Snapshot from MD at 001 surface of MgS$_2$

The second setup is to study the magnesiation in MgS$_2$ surface. We used a slab structure of 001 surface of MgS$_2$ with a vacuum of 15 Å and slab thickness of 18 Å. To localize the polaron, the system is initiated in such a way that one of the S−S bonds at the bottom of the slab is broken. A Mg atom is placed on top of the slab to investigate the effect of magnesiation at the electrode surface. To compensate for the dipole moment from the Mg atom, dipole correction was applied in the direction of the surface.

Fig. 6 depicts snapshots from the MD run. It can be seen that, the p^{2-} is localized at the bottom of the slab in the beginning. The charge is transferred to the surface on subsequent MD steps when the Mg^{2+} begins to interact with the cathode. This is also reflected on the S−S distance of the S dimers in which the charge is localized. The S−S distance of the S dimer at which the polaron localized at the beginning of the simulation has been reduced from 3.6 Å to 2.1 Å. In contrast, the interaction with Mg^{2+} increases the S-S distance of the S-dimer at the surface to 3.6 Å from 3.6 Å. This implies the formation of MgS at the surface. During the MD run, no charge transport path

13

was observed. When Mg^{2+} interacts at the surface, the localized charge from the bottom of the slab abruptly of shifts to the surface. Probably, electron tunneling would have occured from the bottom of the slab to the surface. Typically, tunneling occurs in materials with a thickness of less than 5 nm. unneling happens in materials with a thickness less than 5 nm. But it is not feasible to study such a big system with current setup. In a system large enough to prevent tunneling, we could observe the transport path for the electron.
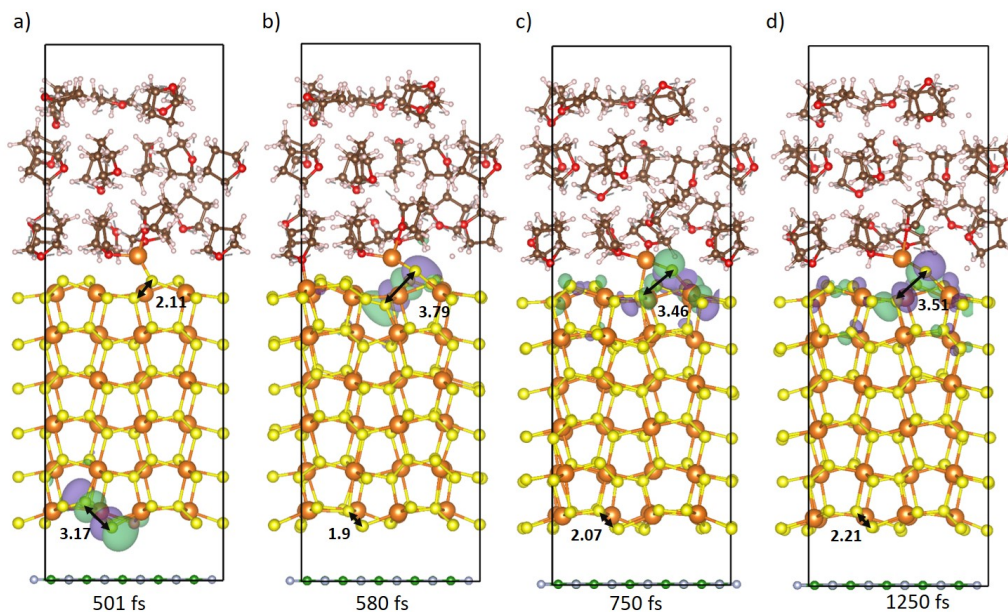

Figure 7: Snapshot from MD at 001 surface of MgS_2

The third AIMD setup was designed to investigate the role of electrolytes in the magnesiation of MgS_2. The vacuum of the slab structure was filled with THF molecules, which are the commonly used electrolyte solvent in magnesium batteries. Using the GROMACS package,[37] 18 THF molecules were added to match the empirical density of $0.88\,\mathrm{g\,cm^{-3}}$.[38] A bottom layer of wide gap semiconductor boron nitride (BN) was employed to prevent charge leakage from the slab's bottom to the electrolyte. Following the initial conjugate gradient relaxation, the electrolyte was relaxed at 350 K for 0.5 ps keeping the crystalline part frozen. Except for the BN, the crystalline

component was unfrozen and relaxed for another 1 ps to allow for cathode - electrolyte interaction. Fig. 7 shows the snapshot from MD run. The observation is similar to what we saw in the previous MD simulation without the electrolyte. The electrolyte seemed to have no direct effect on the magnesiation process, according to our MD simulation.

Conclusion

Elucidating the charge transport mechanism in MgS and MgS_2 is very essential in developing efficient RMBs. We performed a theoretical investigation of charge transport in these materials, evaluating the contribution of several defects to the conductivity in the material. In MgS, we identified Vac_{Mg}^{2-} and Int_{Mg}^{2+} as the prevalent defects. These defects show a relatively high concentration in the material. However, due to their poor mobility, the contribution of these defects to the conductivity of material is negligible. We identified that p^{1-} and Vac_{Mg}^{2-} are the prevalent defects in MgS_2 . The concentration of these defects appears to be quite high. Although the concentration of p^{1-} is low, their mobility is sufficient to allow them to traverse the MgS_2 deposit under practical battery conditions. Consequently, the strategy to enhance the conductivity in MgS_2 is to increase the concentration of p^{1-}. We also performed ab-initio molecular dynamics to understand the charge transport in non-equilibrium conditions. Our results indicate that two p^{1-} in MgS_2 prefer to combine and form a p^{2-}.

References

(1) Bieker, G.; Küpers, V.; Kolek, M.; Winter, M. Intrinsic differences and realistic perspectives of lithium-sulfur and magnesium-sulfur batteries. *Communications Materials* **2021**, *2*, 1–12.

(2) Chung, S.-H.; Manthiram, A. Current status and future prospects of metal–sulfur batteries. *Advanced Materials* **2019**, *31*, 1901125.

(3) Durmus, Y. E.; Zhang, H.; Baakes, F.; Desmaizieres, G.; Hayun, H.; Yang, L.; Kolek, M.;

Küpers, V.; Janek, J.; Mandler, D., et al. Side by side battery technologies with lithium-ion based batteries. *Advanced energy materials* **2020**, *10*, 2000089.

(4) Hong, X.; Mei, J.; Wen, L.; Tong, Y.; Vasileff, A. J.; Wang, L.; Liang, J.; Sun, Z.; Dou, S. X. Nonlithium metal–sulfur batteries: steps toward a leap. *Advanced materials* **2019**, *31*, 1802822.

(5) Zu, C.-X.; Li, H. Thermodynamic analysis on energy densities of batteries. *Energy & Environmental Science* **2011**, *4*, 2614–2624.

(6) Schmuch, R.; Wagner, R.; Hörpel, G.; Placke, T.; Winter, M. Performance and cost of materials for lithium-based rechargeable automotive batteries. *Nature Energy* **2018**, *3*, 267–278.

(7) Hans Wedepohl, K. The composition of the continental crust. Geochem. Cosmochim. Acta 59, 1217–1232. 1995.

(8) Aurbach, D.; Lu, Z.; Schechter, A.; Gofer, Y.; Gizbar, H.; Turgeman, R.; Cohen, Y.; Moshkovich, M.; Levi, E. Prototype systems for rechargeable magnesium batteries. *Nature* **2000**, *407*, 724–727.

(9) Shterenberg, I.; Salama, M.; Yoo, H. D.; Gofer, Y.; Park, J.-B.; Sun, Y.-K.; Aurbach, D. Evaluation of (CF3SO2) 2N-(TFSI) based electrolyte solutions for Mg batteries. *Journal of The Electrochemical Society* **2015**, *162*, A7118.

(10) Zhao-Karger, Z.; Fichtner, M. Magnesium–sulfur battery: its beginning and recent progress. *MRS Communications* **2017**, *7*, 770–784.

(11) Zhao-Karger, Z.; Zhao, X.; Wang, D.; Diemant, T.; Behm, R. J.; Fichtner, M. Performance improvement of magnesium sulfur batteries with modified non-nucleophilic electrolytes. *Advanced Energy Materials* **2015**, *5*, 1401155.

(12) Gao, T.; Ji, X.; Hou, S.; Fan, X.; Li, X.; Yang, C.; Han, F.; Wang, F.; Jiang, J.; Xu, K.,

et al. Thermodynamics and kinetics of sulfur cathode during discharge in MgTFSI2–DME electrolyte. *Advanced Materials* **2018**, *30*, 1704313.

(13) Häcker, J.; Danner, C.; Sievert, B.; Biswas, I.; Zhao-Karger, Z.; Wagner, N.; Friedrich, K. A. Investigation of magnesium–sulfur batteries using electrochemical impedance spectroscopy. *Electrochimica Acta* **2020**, *338*, 135787.

(14) Nakamura, H.; Ogawa, Y.; Kasahara, A., et al. Ionic and positive hole conductivities of solid magnesium and strontium sulfides. *Transactions of the Japan institute of metals* **1984**, *25*, 692–697.

(15) Nakamura, H.; Ogawa, Y.; Kasahara, A.; Iwasaki, S. Sulfur pressure dependence of electrical conductivity of group IIa and IIIa metal sulfides. *Materials Transactions, JIM* **1995**, *36*, 1263–1270.

(16) Puntambekar, U.; Veliah, S.; Pandey, R. Point-defects in magnesium sulfide. *Journal of materials research* **1994**, *9*, 132–134.

(17) Chen, T.; Sai Gautam, G.; Canepa, P. Ionic transport in potential coating materials for Mg batteries. *Chemistry of Materials* **2019**, *31*, 8087–8099.

(18) Kresse, G.; Furthmüller, J. Efficiency of ab-initio total energy calculations for metals and semiconductors using a plane-wave basis set. *Comput. Mater. Sci.* **1996**, *6*, 15–50.

(19) Kresse, G.; Furthmüller, J. Efficient iterative schemes forab initiototal-energy calculations using a plane-wave basis set. *Phys. Rev. B* **1996**, *54*, 11169–11186.

(20) Perdew, J. P.; Burke, K.; Ernzerhof, M. Generalized Gradient Approximation Made Simple. *Phys. Rev. Lett.* **1996**, *77*, 3865–3868.

(21) Haastrup, S.; Strange, M.; Pandey, M.; Deilmann, T.; Schmidt, P. S.; Hinsche, N. F.; Gjerding, M. N.; Torelli, D.; Larsen, P. M.; Riis-Jensen, A. C., et al. The Computational 2D Ma-

terials Database: high-throughput modeling and discovery of atomically thin crystals. *2D Materials* **2018**, *5*, 042002.

(22) Heyd, J.; Scuseria, G. E.; Ernzerhof, M. Hybrid functionals based on a screened Coulomb potential. *The Journal of chemical physics* **2003**, *118*, 8207–8215.

(23) Krukau, A. V.; Vydrov, O. A.; Izmaylov, A. F.; Scuseria, G. E. Influence of the exchange screening parameter on the performance of screened hybrid functionals. *The Journal of chemical physics* **2006**, *125*, 224106.

(24) Shishkin, M.; Kresse, G. Self-consistent G W calculations for semiconductors and insulators. *Physical Review B* **2007**, *75*, 235102.

(25) Blöchl, P. Projector augmented-wave method. *Phys. Rev. B* **1994**, *50*, 17953–17979.

(26) Freysoldt, C.; Neugebauer, J.; Van de Walle, C. G. Fully ab initio finite-size corrections for charged-defect supercell calculations. *Physical review letters* **2009**, *102*, 016402.

(27) Broberg, D.; Medasani, B.; Zimmermann, N. E.; Yu, G.; Canning, A.; Haranczyk, M.; Asta, M.; Hautier, G. PyCDT: A Python toolkit for modeling point defects in semiconductors and insulators. *Computer Physics Communications* **2018**, *226*, 165–179.

(28) Tilley, R. J. *Defects in solids*; John Wiley & Sons, 2008.

(29) Henkelman, G.; Jónsson, H. Improved tangent estimate in the nudged elastic band method for finding minimum energy paths and saddle points. *The Journal of chemical physics* **2000**, *113*, 9978–9985.

(30) Larsen, A. H.; Mortensen, J. J.; Blomqvist, J.; Castelli, I. E.; Christensen, R.; Dułak, M.; Friis, J.; Groves, M. N.; Hammer, B.; Hargus, C., et al. The atomic simulation environment—a Python library for working with atoms. *Journal of Physics: Condensed Matter* **2017**, *29*, 273002.

(31) Mali, G. Ab initio crystal structure prediction of magnesium (poly) sulfides and calculation of their NMR parameters. *Acta Crystallographica Section C: Structural Chemistry* **2017**, *73*, 229–233.

(32) Primak, W.; Kaufman, H.; Ward, R. X-ray diffraction studies of systems involved in the preparation of alkaline earth sulfide and selenide phosphors1. *Journal of the American Chemical Society* **1948**, *70*, 2043–2046.

(33) Lany, S. Polymorphism, band-structure, band-lineup, and alloy energetics of the group II oxides and sulfides MgO, ZnO, CdO, MgS, ZnS, CdS. Oxide-based Materials and Devices V. 2014; pp 109–116.

(34) Zhao, C.; Duan, Y.; Gao, J.; Dong, H. Crystal and band structures of ZnS, MgS, and ZnS-MgS alloys. *Journal of Applied Physics* **2017**, *121*, 235705.

(35) Smith, J. G.; Naruse, J.; Hiramatsu, H.; Siegel, D. J. Intrinsic conductivity in magnesium–oxygen battery discharge products: MgO and MgO2. *Chemistry of Materials* **2017**, *29*, 3152–3163.

(36) Saal, J. E.; Kirklin, S.; Aykol, M.; Meredig, B.; Wolverton, C. Materials design and discovery with high-throughput density functional theory: the open quantum materials database (OQMD). *Jom* **2013**, *65*, 1501–1509.

(37) Abraham, M. J.; Murtola, T.; Schulz, R.; Páll, S.; Smith, J. C.; Hess, B.; Lindahl, E. GROMACS: High performance molecular simulations through multi-level parallelism from laptops to supercomputers. *SoftwareX* **2015**, *1*, 19–25.

(38) Guard, U. C. Chemical Hazard Response Information System (CHRIS)-Hazardous Chemical Data. *Commandant Instruction* **1999**, *16465*.